UNIVERSITY OF SOUTHAMPTON

FACULTY OF ENGINEERING, SCIENCE AND MATHEMATICS

Optoelectronics Research Centre

Femtosecond laser micro-machining and consequent self-assembled nano-structures in transparent materials

by

Erica Bricchi

Thesis submitted for the degree of Doctor of Philosophy

September 2005

UNIVERSITY OF SOUTHAMPTON

ABSTRACT

FACULTY OF ENGINEERING, SCIENCE AND MATHEMATICS
OPTOELECTRONICS RESEARCH CENTRE

Doctor of Philosophy

Femtosecond laser micro-machining and consequent self-assembled nano-structures in transparent materials

by Erica Bricchi

In this thesis we have reported novel developments in the field of femtosecond laser micro-machining within the bulk of transparent materials. Thanks to its unique properties, the femtosecond laser writing technique offers the potential for realizing three-dimensional multi-component photonic devices, fabricated in a single step and in a variety of transparent materials. When we began to research in this field, there had been no studies conducted on the ability of femtosecond lasers to fabricate diffractive optical components in the bulk of a dielectric material. These are necessary components for the realization of monolithic optical devices. Our work led to the first demonstration of femtosecond directly written diffractive optic devices (Fresnel zone plates) embedded in a silica substrate. Both the focusing properties and efficiencies of the devices compared well with the theoretical values.

In addition, the few reports on the measurement of the laser-induced index change were contradictory. In our view, it became clear that a systematic study was urgently required to be able to fully realize, in the future, precise designs for the fabrication of photonic devices. With a phase step interferometric technique, we measured the laser-induced index change (in modulus and sign) in various materials in a practical and simple way, which was nondestructive, and did not require further processing of the samples.

Finally, as the interaction between ultrashort laser pulses and transparent dielectric materials was a new research topic, its fundamental mechanisms were largely unknown. A better understanding of the fundamentals is essential for an efficient use of this writing technique. We observed and characterized a new a class of structure created by femtosecond irradiation of silica glass (type II), characterized by a spectrally selective reflection occurring only in the direction of the electric field of the writing laser, negative index change, birefringence, and extraordinary stability at high temperatures. This led to the discovery of the formation of self-assembled periodic sub-wavelength structures created during the direct writing in silica glass. Their existence was theoretically predicted to justify our experimental evidence and ultimately observed experimentally, thus revealing the *smallest signature of light.*

Contents

Declaration of Authorship

I, Erica Bricchi

declare that the thesis entitled

Femtosecond laser micro-machining and consequent self-assembled nano-structures in transparent materials

and the work presented in it are my own. I confirm that:

- this work was done wholly or mainly while in candidature for a research degree at this University;
- where any part of this thesis has previously been submitted for a degree or any other qualification at this University or any other institution, this has been clearly stated;
- where I have consulted the published work of others, this is always clearly attributed;
- where I have quoted from the work of others, the source is always given. With the exception of such quotations, this thesis is entirely my own work;
- I have acknowledged all main sources of help;
- where the thesis is based on work done by myself jointly with others, I have made clear exactly what was done by others and what I have contributed myself;
- parts of this work have been published (See *List of Publications*).

Erica Bricchi

September 2005

Nomenclature

Abbreviations

AFM	Atomic Force Microscope
CCD	Charged Coupled Device
CW	Continuous wave
IR	Infra Red
FL	Fresnel Lens
FZD	Fresnel Zone Device
FZP	Fresnel Zone Plate
MFZP	Multilevel Fresnel Zone Plate
MPI	Multiphoton Ionization
NA	Numerical Aperture
OSA	Optical Spectrum Analyzer
ORC	Optoelectronic Research Centre
PI	Photoionization
SEM	Scanning Electron Microscope
UV	Ultra Violet

Symbols

$\mathbf{B}$	Magnetic displacement vector
$\mathbf{D}$	Electric displacement vector
$\mathbf{E}$	Electric field
$\mathbf{H}$	Magnetic field
$\mathbf{P}$	Induced electric polarization
E_g	Band-gap of the material
E_p	Pulse energy
I	Intensity
T_e	Electron temperature
f_f	Filling factor of the nano-grating

n_1, n_2	Refractive indices of the nano-grating
n_{2bg}	Non-linear refractive index
n_{bg}	Refractive index in the linear approximation
n_e	Extraordinary refractive index
n_o	Ordinary refractive index
r	Repetition rate of the laser
$\hat{\mathbf{s}}$	Direction of propagation
s_s	Speed of the translation stage
t	Time coordinate
t_1, t_2	Thickness of the plates of the nano-gratings
t_p	Thickness of the written structures
v_e	Average thermal speed of electrons
v_p	Phase velocity

γ	Keldysh parameter
ε_0	Electric permittivity in free space
$\varepsilon_1, \varepsilon_2$	Dielectric permettivities of the plates of the nano-gratings
k	Magnitude of the wave vector
k_w	Magnitude of the wave vector of the writing laser
Λ	Period of the nano-grating
λ	Generic wavelength of a monochromatic wave
λ_w	Wavelength of the writing laser
μ_0	Magnetic permittivity in free space
ρ	Electron density
τ	Full width at half maximum of the temporal shape of the pulse
ω	Optical frequency
ω_0	Spatial radius of the Gaussian intensity beam profile at $1/e^2$
ω_p	Plasma frequency

Constants

$c = 2.998 \times 10^8\, m/s$	Speed of light
$e = 1.602 \times 10^{-19}\, C$	Charge of the electron
$h = 6.626 \times 10^{-34}\, Js$	Planck's constant
$m_e = 9.1095 \times 10^{-31}\, kg$	Mass of the electron
$k_B = 1.384 \times 10^{-23}\, J/K$	Boltzman constant

Acknowledgements

Now that my student days are coming to an end, I wish to express my gratitude to the numerous individuals who helped my professional growth in these last years, and who contributed (directly or indirectly) to the work presented in this thesis. I consider myself extremely fortunate to have had the opportunity to conduct my postgraduate studies in the ORC, which has been a stimulating working environment. I am therefore grateful to the company Pirelli Cavi e Sistemi and in particular Marco Romagnoli, who originally sent me here and supported my first six months, and to the Engineering and Physical Sciences Research Council (EPSRC) who sponsored my PhD.

I am thankful to my supervisor, Peter Kazansky, for being an extraordinary example of a passionate and dedicated scientist, someone who truly has an intuition for physics. Sincere thanks to John Mills who encouraged me choosing this fascinating PhD project and for getting me through my first year. I pay a special tribute to Bruce Klappauf, who dedicated an enormous amount of time and efforts to the project and assisted me during the most difficult moments of this adventure. I owe a particular acknowledgement to Jeremy Baumberg, who guided me in the early days, contributing his brilliance and drive to the project. I wish to express my gratitude to Caterina Netti, who made available her vast experience on the laser source during my training period, and to Lola Martin and Pavlos Lagudakis, who helped me in the lab during the following years.

I wish to acknowledge Arshad Mairaj, Angelique Favre and Emanuela Franchina for their collaboration on the direct-writing of different materials. Thank you for the valuable discussions and the fun time in the lab. A big thank you to Bill Brocklesby, Peter Jander, James Gates and Chris Hillman for their patience and enormous help during my first six months abroad as a summer student.

I am sincerely grateful to Dave Oliver, Arthur Longhurst, Kevin Summer and Vittoria Finazzi for their prompt help with my (many) computer problems. I wish to thank Chris Nash, Simon Butler, Tim McIntyre in the ORC, and Colin Miles and Tom Perkins in Physics for their efficiency and for helping make the long hours in the lab more cheerful. I am thankful to all the administration staff and in particular to Eve Smith, Joyce Aburrow, Heather Spencer, Jenny Morley, and Janet Mansour. Besides being extremely efficient and helpful, they also add that feminine touch, which a woman, working in a male-dominated environment, longs for.

I wish to thank Jacob and Eleanor, my proofreaders, for their corrections and their useful critics. Without them, writing this thesis would have taken even longer.

Finally, a big thank you to the other students in the group, Costa (not a student anymore!), Steve and Weijia and to my numerous office-mates (Francesca, Anoma, Paulo and Adriaan, just to mention a few) whom I shared the daily ups and downs of postgraduate student life. As such, the technical acknowledgements are blurring towards the personal ones. I am eternally grateful to all my dear ones: Jacob, my parents, the rest of my family (now embracing two continents), and all my friends (some of which already appeared in their “official” role), who have supported and encouraged me through the years. You filled my life with love, friendship, joy and laughter, which were fundamental ingredients enabling me to face my work challenges with serenity.

To each and all of you I thankfully dedicate this thesis.

Ai 90 anni del mio caro nonno Angelo,
ed in memoria dei tanto amati
Virginia, Gianfranco ed Enrica.

Chapter 1

Introduction

1.1 Historical background

Material processing with lasers is an expanding field, which is capturing the attention of scientists, engineers, and industry alike. The aspect of most interest to scientists is the fundamental interaction mechanisms between the intense light of a laser and matter. Engineers and manufacturers see in the laser a tool, which not only makes manufacturing cheaper, faster, cleaner, and more accurate, but also opens up entirely new technologies and fabrication methods that are simply not available using other techniques. The most established applications are surface ablative laser machining (cutting, and drilling), surface treatments, and laser welding. These applications are of interest for a range of disciplines such as metallurgy, electronics, chemical engineering, and laser surgery, just to mention a few.

Increasingly, however, lasers are also being used for machining optical materials for photonic applications, which is our area of interest. Indeed, the interaction of lasers with transparent materials, the basic components of optoelectronic devices, has been studied for many years. Initially, for practical reasons, it was important to determine the laser-induced damage thresholds of materials used in high power laser optics, but there have also been many fundamental studies on laser ablation. Laser ablation is generally performed using pulsed lasers, however, for applications requiring precise micro-structuring, the utility of lasers with pulse durations in the nanosecond to microsecond range is limited by thermal damage [1].

Another important part of the study of the interaction between light and transparent materials, concerns the ability of lasers to modify the refractive index of the irradiated materials. Indeed, laser sources have been used to induce photodarkening effects and gratings in photorefractive and semiconductor-doped materials [2, 3]. The discovery of the photosensitivity of silica fibers at ultra violet (UV) wavelengths [4, 5], and the extension of this method to a direct-writing technique [6, 7] has been a breakthrough having a major impact on guided wave device development. UV direct-write methods have been used to write Bragg gratings in planar waveguides [8] and optical fibers [9, 10], and even to fabricate waveguides in bulk glasses [11, 12]. This technique, however, has inherent limitations; in particular, many glasses are not sufficiently sensitive to the wavelength of the available UV lasers to yield significant changes in their refractive index upon exposure. Also, the UV photosensitivity band is very close to the absorption edge of most glasses, and thus the UV penetration depth is small. This fact has precluded the use of the UV direct-write technique from producing three-dimensional structures embedded inside the bulk of the optical materials.

In recent years, lasers with pulsewidths in the femtosecond range (generally termed “ultrashort” lasers being their pulse duration, τ, $\ll 10\,ps$) become commercially available, allowing materials to be subjected to higher intensities than ever before. The high intensity of a focused ultrashort-pulse laser enables localized non-linear absorption of the incident photons within the irradiated material. If enough laser energy is deposited, permanent structural changes are produced in the material at the location of the laser focus. When the focal plane is at the surface, ablation takes place. However, due to the much faster energy deposition, surface ablation with femtosecond pulsed lasers is different from long-pulse (nanosecond) laser ablation [1]. The short temporal duration of the femtosecond pulses is such that all the energy is absorbed before it can be dissipated into the material by phonon scattering. This characteristic leads to clean and high-aspect ratio damage sites, allowing microstructures to be produced with very high precision and reproducibility [13, 14, 15, 16, 17]. Because the energy absorption occurs via non-linear effects, which require high intensities, if the beam is focused inside a transparent material by an external lens, the interaction volume can be confined entirely inside the bulk of the medium. In this case, after the energy is deposited by the laser pulse, ablation is not possible because the excited volume is restrained by the surrounding material. The ultrafast energy deposition creates high temperatures and pressures inside the region leading to a micro-explosion [16, 18]; material is ejected from the center and forced outward into the surrounding volume, leading to the formation of a structure consisting of a void surrounded by densified material [19, 20]. This irradiation regime has been utilized to demonstrate three-dimensional data storage [19] and photonic crystals [21]. As such, the “femtosecond direct-write technique” was born, consisting of a focused high intensity laser beam, produced by a lens or objective external to a bulk material, which can be translated in the three dimensions.

The year of 1996 was a turning point for femtosecond-laser micro-machining as Davis et al. [22] demonstrated that, at exposures levels below damage threshold, it is possible to achieve a modification of the refractive index (up to 10^{-2}) in the bulk of various transparent materials. This enabled the potential for an even wider variety of devices for optical applications, which benefit from the capability of direct-writing without a photolithographic process, including the possibility of fabricating three-dimensional structures. Indeed, the possibility of creating guiding devices in three-dimensions and in a single fabrication step attracted the attention of most of the research groups working in the area. Miura et al. [23] demonstrated the first femtosecond written channels embedded in the bulk of various glasses (Ge-doped silica, fluoride, borosilicate, phosphate and chalcogenide glasses), and soon after active waveguides and three-dimensional couplers were reported [24, 25, 26]. The femtosecond writing technique offers two configurations for fabricating waveguides, longitudinally or transversely, depending on how the sample is translated, respectively, along or perpendicular to the beam-propagation direction. The longitudinal writing configuration intrinsically produces symmetric waveguides, but their length is limited by the working distance of the focusing objective. The transverse geometry provides more flexibility and allows writing waveguides of arbitrary length but gives rise to an asymmetry in the waveguide cross section which displays a large aspect ratio. To overcome this disadvantage in 2003 Cerullo et al. [27] and Mihailov et al. [28] proposed a technique, based on astigmatic shaping of the femtosecond writing beam, that allows both the elimination of the waveguide asymmetry in the transverse geometry and control of the written structures size.

The first demonstrations of ultrafast processing in transparent dielectrics were all carried out using amplified femtosecond lasers, which deliver high energy pulses (up to the mJ level). For this kind of system, almost any kind of focusing optic is sufficient to produce intensity levels required to modify the irradiated material. Once the material, the pulse duration and the wavelength of the laser have been chosen, the required modification intensity threshold is a constant, hence the tighter the focus in the sample, the less laser energy is required to reach the intensity threshold. This simple idea was successfully applied by Schaffer et al. [29], and Efimov et al. [30] who demonstrated the possibility of micro-machining bulk glass using femtosecond laser pulses with nanojoule energy. Such a low pulse energy can be achieved with a simple and cheaper femtosecond oscillator without subsequent amplification. However, unamplified systems require high numerical aperture objectives which are affected by aberrations and are characterized by a very short focal length (few millimeters) [31]. This latter property limits the maximum depth at which it is possible to write into a medium. Since the first demonstrations of unamplified femtosecond writing, the ultrafast micro-machining has been performed with both amplified and unamplified systems [26, 32, 33]. Nevertheless, the utilization of one or the other source leads to dissimilar results, as the cumulative effect due to the high repetition rate of the unamplified systems makes the written structure similar to those achieved with a longer pulse laser [34].

Whilst most of the studies has focused on the demonstration and optimization of guiding optical devices, some authors shifted their attention towards other applications such as fiber Bragg gratings [35, 36], and three-dimensional microfluidic channels, either realized with a multi-step technique combining refractive index modification and etching [37, 38, 39], or directly drilled in the bulk [40]. On the other hand, the studies focused on the characterization, modelling and understanding of the mechanisms involved in the modification of the refractive index have been less numerous and still not conclusive. In order to explain the experimentally observed material modification, it has been suggested that if the melting temperature is exceeded in a small volume, the material can resolidify nonuniformly, leading to density and refractive index variations [23, 24, 35]. In addition, ultrashort laser pulses have been observed to induce the formation of defects, which could be used to explain the refractive index change in the irradiated material, however, it has also been demonstrated that the defects anneal quicker than the refractive index, hence suggesting that they cannot be ascribed as the only responsible for the modification of the refractive index [22, 32, 41, 42, 43]. Furthermore, unexpected phenomena have been observed, suggesting that other new mechanisms may contribute to the modification of the irradiated materials. Indeed, Kazansky et al. [44], and Qui et al. [45] reported anisotropic light scattering peaking in the plane of polarization during direct-writing with ultrashort light pulses in glass. This effect was interpreted in terms of photoelectrons moving along the direction of light polarization inducing subwavelength inhomogeneities. Uniaxial birefringence of structures in fused silica written by femtosecond light pulses was also observed: the index change for light polarized along the direction of the polarization of the writing beam was higher than for the orthogonal polarization [46].

It is with this background that our investigations in the field of micro-machining of transparent materials began, with the the femtosecond writing technique still in its infancy and new physical phenomena to be unveiled. Our research was aimed to give a contribution to each of the major research areas involved in the developing of the femtosecond writing technique, namely the exploration of novel applications, the characterization of the laser-induced modification, and the investigation of the fundamental light-material interactions. In particular, we devoted our efforts:

- To demonstrate the capability of the technique for realizing embedded optic components.
- To progress the understanding of the anisotropic effects observed during femtosecond writing technique.
- To characterize the behaviour of laser-induced refractive index change versus the laser energy density, in various transparent materials.

1.2 Main achievements

At the beginning of this thesis, we present the first investigation of a diffractive optical device realized by the femtosecond writing technique. Utilizing the laser-induced modification of the refractive index, we fabricated efficient Fresnel zone plates embedded in the bulk of silica glass. This pioneering result triggered a new branch of research focused on the fabrication of diffractive optic devices such as diffraction gratings [47] and beam shapers [48, 49]. One limitation in the design of our devices was that the laser induced refractive index change and its dependence on the laser energy density were still largely unknown. There are contradictory reports of the magnitude of the induced refractive change Δn that ranges from ~ 0.03, when measured with a microscopic ellipsometer [22], down to $\Delta n = (1-6) \times 10^{-3}$ when measured with other techniques [26, 33, 46, 50]. In our view, it became clear that a systematic study was urgently required to be able to realize, in the future, precise designs for the fabrication of photonic devices. With a phase step interferometric technique, we measured the laser-induced index change (in modulus and sign) in a practical and simple way, which was nondestructive, and did not require further processing of the samples.

The ability to measure the sign of the refractive index change enabled us to discover that, in silica glass, the femtosecond laser-induced index modulation suddenly changes sign, becoming negative, with increasing pulse energy. Meanwhile, we had also observed a new anisotropic property of certain written structures, namely a reflection occurring only along the direction coincident with the polarization of the writing laser. Our observations demonstrate that anisotropic reflection, negative index change and birefringence onset at the same threshold. We explained our experimental evidence, assuming that a self-assembled periodic nanostructure was created within the irradiated volume. We showed that this theory was consistent with a theoretical model based on form birefringence and furthermore strengthened by the consideration that the orientation of the alleged nanostructure is identical to that implicated in a previous publication from our group describing the empirical observation of anisotropic light scattering [44]. Finally, we proved this theory with the experimental evidence of the presence of periodic nanostructures created in the irradiated bulk by a single focused beam. As such, we had discovered a new type of femtosecond structure characterized by the presence of a self-assembled periodic structure within the irradiated volume. In addition to the anisotropic reflection, negative index change and birefringence, we observed an extraordinary stability of these structures. In agreement with the first papers reporting the appearance of birefringence in certain direct-written structures, we defined this novel class of femtosecond structures as **type II-fs** (not to be confused with the UV written grating of type II).

Finally, utilizing the phase stepping technique, we have investigated the modification of the index change of various transparent materials. Indeed, one of the attractive features offered by the femtosecond writing technique is the potential flexibility in the variety of glasses that can be modified. Although silica glass has been the most commonly investigated glass for femtosecond micro-machining, device fabrication has been realized in a number of glass systems (fluoride, germanosilicate [22] chalcogenide [22, 30], borosilicate [29] and phosphate glasses [51]). Multicomponent glasses are indispensable for fabricating active integrated devices since their network structure can be easily altered to accommodate dopants that provide the desired active and non-linear properties. However, so far, no systematic measurements of the laser-induced refractive index change for relevant materials has been provided. The results of our analysis, presented in the last part of this manuscript, provide a useful set of data for the future design of photonic devices. In particular, we found that it was possible to create a modification of the refractive index in sapphire crystal without cracking the surrounding material. This result has been recently confirmed in [52], where active waveguides directly written by femtosecond irradiation have been demonstrated in a Ti^{3+}: sapphire crystal.

Chapter 2

Ultrashort pulse irradiation of transparent materials

Ultrashort pulses with moderate energy can have an extremely high peak power and peak intensity ($I > 10^{13}\, W/cm^2$). When materials (e.g. silica glass) are exposed to these high intensities, the light-matter interaction becomes non-linear. In Section 2.1, we review the equations describing the propagation of an electromagnetic wave in a dielectric material in a non-linear regime. Section 2.2 and Section 2.3 give a brief overview of the mechanisms involved during ionization and relaxation of a material subjected to an intense irradiation. Finally, the difficulties related to the theoretical modelling of the interaction between femtosecond beams focused into the bulk are briefly described (Sec. 2.5).

2.1 Non-linear propagation of short pulses in transparent material

The propagation of an electromagnetic wave in a medium is governed by the Maxwell equations

$$\nabla \times \mathbf{E} = -\frac{\partial \mathbf{B}}{\partial t}, \tag{2.1a}$$

$$\nabla \times \mathbf{H} = \frac{\partial \mathbf{D}}{\partial t} + \mathbf{j}, \tag{2.1b}$$

$$\nabla \cdot \mathbf{D} = q, \tag{2.1c}$$

$$\nabla \cdot \mathbf{B} = 0, \tag{2.1d}$$

where **E** and **H** are the electric and magnetic field vectors, respectively, **D** and **B** are corresponding electric displacement vectors and q and **j** are the free electric charge and current densities. The displacement vectors **D** and **B** arise in response to the electric and magnetic fields **E** and **H** propagating inside the medium and are related to them through the constitutive relations given by

$$\mathbf{D} = \varepsilon_0 \mathbf{E} + \mathbf{P} \tag{2.2a}$$

$$\mathbf{B} = \mu_0 \mathbf{H}, \tag{2.2b}$$

where ε_0 is the vacuum permittivity, μ_0 is the vacuum permeability, and **P** is the induced electric polarization. Combining (2.1) and (2.2) it is possible to obtain the wave equation that describes the light propagation in a dielectric material ($q = \mathbf{j} = 0$):

$$\nabla^2 \mathbf{E} = \frac{1}{c^2}\frac{\partial^2 \mathbf{E}}{\partial t^2} + \mu_0 \frac{\partial^2 \mathbf{P}}{\partial t^2}, \tag{2.3}$$

where $1/c^2 = \varepsilon_0 \mu_0$, and c is the speed of light in vacuum. To complete the description, a relationship between **P** and **E** is needed. If the material does not have memory then

$$\begin{aligned} \mathbf{P} &= \varepsilon_0 \left(\chi^{(1)}\mathbf{E} + \chi^{(2)}\mathbf{E}\cdot\mathbf{E} + \chi^{(3)}\mathbf{E}\cdot\mathbf{E}\cdot\mathbf{E} + \cdots\right), \\ &= \left[\mathbf{P^{(1)}} + \mathbf{P^{(2)}} + \mathbf{P^{(3)}} + \cdots\right] \end{aligned} \tag{2.4}$$

where $\chi^{(j)}$ $(j = 1, 2, \ldots)$ is the jth order susceptibility, and $\mathbf{P^{(j)}}$ id the jth order polarization. Each of the electric fields on the right hand side of equation (2.4) can have different frequency components, and there will be a non-linear polarization produced at the sum and/or difference of these frequency components.

Generally, the orders over the 3rd in (2.4) are negligible, moreover, in all the materials with inversion symmetry (for istance isotropic glasses) $\chi^{(2)}$ vanishes. As a result (2.4) simplifies to

$$\mathbf{P} = \varepsilon_0 \chi^{(1)}\mathbf{E} + \varepsilon_0 \chi^{(3)}\mathbf{E}\cdot\mathbf{E}\cdot\mathbf{E} = \mathbf{P_L} + \mathbf{P_{NL}}, \tag{2.5}$$

where $\mathbf{P_L}$ and $\mathbf{P_{NL}}$ are, respectively, the linear and non linear polarization. Including all the three permutation of the fields on the right side of equation (2.4) which contribute to the non-linear polarization, (2.5) becomes:

$$\mathbf{P} = \varepsilon_0 \left[\chi^{(1)} + \frac{3}{4}\chi^{(3)}|\mathbf{E}|^2\right]\mathbf{E}, \tag{2.6}$$

hence (2.3) can be simplified to:

$$\nabla \times \nabla \times \mathbf{E} + \frac{n^2}{c^2}\frac{\partial^2 \mathbf{E}}{\partial t^2} = 0, \tag{2.7}$$

where n, the refractive index, is given by:

$$n = \sqrt{1 + \chi^{(1)} + \frac{3}{4}\chi^{(3)}|\mathbf{E}|^2}. \tag{2.8}$$

Taking the non-linear term to be small compared to the linear susceptibility and expressing the electric field strength in terms of the laser intensity I, we have

$$n = n_{bg} + n_{2bg} I, \tag{2.9}$$

where the the laser intensity is

$$I = \frac{1}{2}\varepsilon_0 c n_{bg} |\mathbf{E}|^2, \tag{2.10}$$

and the linear and non-linear refractive index are, respectively,

$$n_{bg} = \sqrt{1 + \chi^{(1)}}, \tag{2.11}$$

$$n_{2bg} = \frac{3\chi^{(3)}}{4\varepsilon_0 c n_{bg}^2}. \tag{2.12}$$

This non-linear refractive index (2.12) explains many of the features of the propagation in transparent materials [53].

2.1.1 Self-focusing and plasma defocusing

The phenomenon of self-focusing is a result of the intensity-dependent non-linear refractive index of the materials, given by equation (2.9). The spatial intensity profile of the laser pulse leads to a spatial refractive index profile: because n_{2bg} is positive in most materials, the refractive index is higher at the centre of the beam compared to the wings. Hence, the variation in refractive index acts as a lens and focuses the beam. Although the refractive index variation depends on the laser intensity, the strength of the self-focusing lens depends only on the peak power of the laser pulse [54]. As the power in the pulse is increased, self-focusing becomes stronger until, at some critical power, it balances diffraction and a filament is formed. If the peak power of the laser pulse exceeds this critical power for self-focusing then catastrophic collapse of the beam to a singularity is predicted. The critical power P_c, is given by [31]

$$P_c \sim \frac{\pi \lambda_w^2}{8 n_{bg} n_{2bg}} \tag{2.13}$$

In reality, other mechanisms halt the collapse of the beam due to self-focusing. In particular, as the laser beam self-focuses, the intensity rises and eventually becomes sufficient to non-linearly ionize the material (Sec. 2.2). A plasma is hence formed and it contributes a negative refractive index change that cancels the positive refractive index change produced by the intensity-dependent index and prevents further self-focusing [55]. The complex refractive index variation in the created plasma is quantitatively described by means of the laser-induced plasma index modulation, Δn_{pl}, defined as [56]

$$\Delta n_{pl} = \frac{2e^2\tau_e}{n_{bg}m_e\omega}\frac{i-\omega\tau_e}{1+\omega^2\tau_e^2}\rho, \tag{2.14}$$

where e and m_e are the electron charge and mass, τ_e is the electron collision time, and ρ is the plasma density. As shown, the plasma formation causes a decrease in the real part of the medium's refractive index and acts as a concave lens.

2.2 Non-linear absorption

When an electromagnetic wave is propagating through a medium, it can be absorbed: for instance, part of the incoming laser energy promotes electrons from the valence to the conduction band of the material. If the photon energy E_p, ($E_p = hc/\lambda_w$, with h Planck's constant, c the speed of light, and λ_w emission wavelength of the laser), is greater than the energy gap of the material E_g, a single photon has sufficient energy to ionize the irradiated material and the laser energy is said to be *linearly* absorbed. On the other hand, if the band-gap E_g is greater than the photon energy, the material is transparent to the incident laser light. However, in a pure transparent material energy absorption may occur but only through non-linear mechanisms. There are two classes of non-linear absorption processes leading to the ionization of the irradiated material: non-linear photoionization and avalanche ionization.

2.2.1 Photoionization

Photoionization refers to excitation of the electron into the conduction band by the laser field. Depending on the laser frequency and intensity, the material can be either ionized through a tunneling effect, or multiphoton absorption [57]. In tunnelling ionization, the electric field of the laser suppresses the Coulomb well that binds a valence electron to its parent atom. If the electric field is very strong ($|\mathbf{E}| > 10^9\,V/cm$), the Coulomb well can be suppressed enough that there is a significant probability that the bound electron can

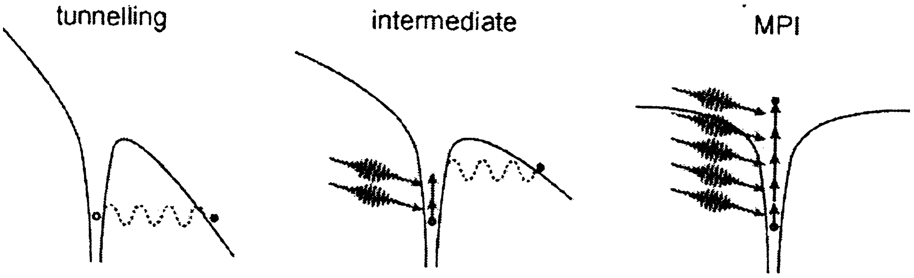

FIGURE 2.1: Schematic diagram of the photoionization of an electron through tunnelling (left), multiphoton ionization (right) or both non-linear processes (central) [57].

tunnel through the barrier and become free (Fig. 2.1). On the other hand, multiphoton ionization occurs when an atom simultaneously absorbs enough photons whose combined energy is sufficient to exceed the materials band-gap (Fig. 2.1). The photoionization rate depends strongly on the laser intensity I; i.e. the multiphoton ionization regime, the rate is

$$\left(\frac{\mathrm{d}\rho}{\mathrm{d}t}\right)_{\mathrm{MPI}} = \sigma_m I^m, \tag{2.15}$$

where σ_m is the multiphoton absorption coefficient for absorption for m photons. The number of photons required is determined by the smallest m which satisfies the relation $mhc/\lambda_w \geqslant E_g$. In contrast, the tunnelling rate scales more weakly with the laser intensity than the multiphoton rate [58]. While tunnelling ionization dominates for strong laser fields and low (far IR) optical frequency, $\omega = 2\pi/\lambda_w$, at high (visible) frequency (but still below that required for single photon absorption), multiphoton hotoionization becomes the dominant mechanism. The transition between the two types of ionization was expressed by Keldysh [59] in terms of the Keldysh parameter

$$\gamma = \frac{\omega}{e}\sqrt{\frac{m_e c n_{bg} \varepsilon_0 E_g}{I}}. \tag{2.16}$$

When the Keldysh parameter is larger (smaller) than ~ 1.5, photoionization is a multiphoton (tunnelling) process. In the intermediate regime, the photoionization is a mix between the two mechanisms (Fig. 2.1).

2.2.2 Avalanche ionization

Avalanche ionization involves free carrier absorption followed by impact ionization. An electron already in the conduction band of a material exhibits linear absorption of other incident laser photons, therefore gaining energy within the conduction band. After the absorption of m photons, where m is the smallest number satisfying $mhc/\lambda_w \geqslant E_g$, such that the electron's energy exceeds the conduction band minimum by more than the band-gap energy, this electron can then ionize, via a collision, another electron from

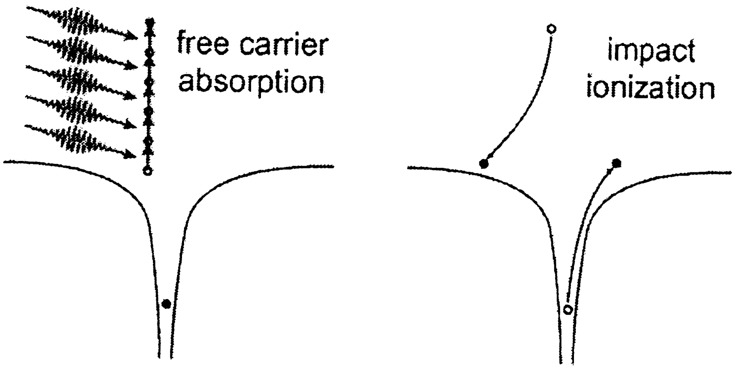

Figure 2.2: Schematic diagram of avalanche ionization [57].

the valence band resulting in two electrons near the conduction band minimum, each of which can absorb energy through free carrier absorption and subsequently impact ionize additional valence band electrons (Fig. 2.2). As long as the laser field is present, the electron density in the conduction band grows accordingly to

$$\left(\frac{\mathrm{d}\rho}{\mathrm{d}t}\right)_{\mathrm{AV}} = \eta(\mathbf{E})\rho, \tag{2.17}$$

where $\eta(\mathbf{E})$ is the avalanche ionization rate and $\mathbf{E}$ is the electric field of the laser. Avalanche ionization requires some seed electrons in the conduction band of the material. These initial electrons are provided either by thermally excited carriers, easily ionized impurity and defect states, or by carriers that are directly excited by the aforementioned photoionization.

The ionization process of a solid illuminated by an intense laser pulse can be described by the general equation

$$\frac{\mathrm{d}\rho}{\mathrm{d}t} = \left(\frac{\mathrm{d}\rho}{\mathrm{d}t}\right)_{\mathrm{AV}} + \left(\frac{\mathrm{d}\rho}{\mathrm{d}t}\right)_{\mathrm{PI}} - \left(\frac{\mathrm{d}\rho}{\mathrm{d}t}\right)_{\mathrm{LOSS}} \tag{2.18}$$

The first term on the right hand side is the avalanche ionization contribution, the second the photoionization contribution, and the last is the loss due to electron diffusion, recombination, etc. (Sec. 2.3). When the pulse width is shorter than a picosecond, the loss of electrons is negiglible during the duration of the pulse. Kaiser et al. [60] computed the relative contributions of PI and avalanche process for fused silica. Those authors conclusively showed that for pulsewidths below 150 *fs* the dominant mechanism is the photoionization (not the avalanche) mechanism and give a comprehensive analysis of electron excitation in silica by ultrashort pulses. When a large (10% or more) fraction of the valence electrons are excited to the conduction band, a high density of free electrons (plasma of electrons) is created in the irradiated volume. This ionization process, with the subsequent formation of plasma, is defined as *optical induced damage or breakdown.*

2.3 Energy transfer to the material

In the previous section we have seen how non-linear absorption processes lead to the ionization of a portion of the irradiated transparent material. Once excited, the electrons quickly relax through a number of processes such as thermalization, carrier removal, and thermal effects (Fig. 2.3).

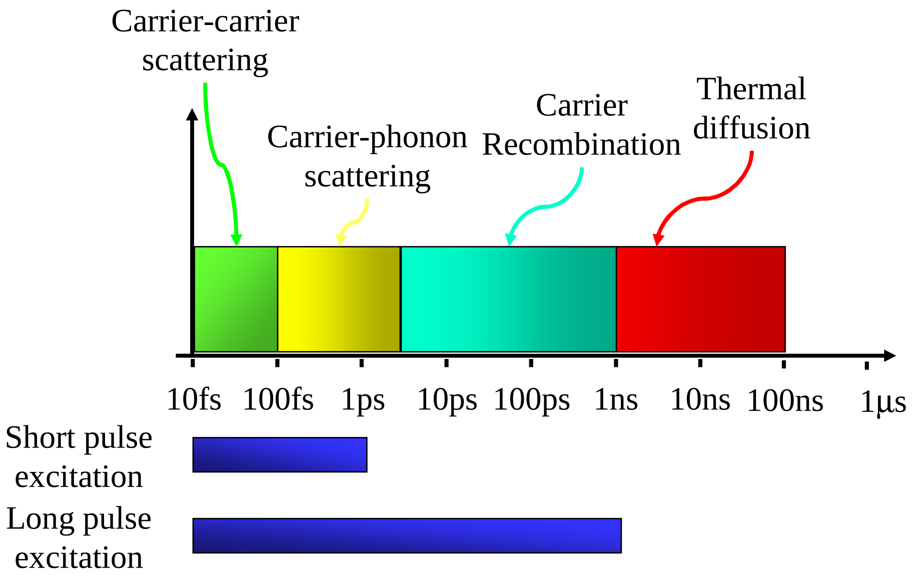

FIGURE 2.3: Schematic diagram of the timescale of electronic interactions.

2.3.1 Thermalization

After excitation, electrons and holes are redistributed throughout the conduction and valence bands via carrier-carrier scattering and carrier-phonon scattering. Carrier-carrier scattering changes neither the total energy in the carriers nor the carrier density but redistributes the energy of the carriers over the conduction band on a $10 - 100\,fs$ time scale. In a carrier-phonon scattering process, free carriers lose momentum by emission of a phonon. Although carrier-phonon scattering does not change the number of carriers, their energy decreases due to spontaneous emission, which transfers energy to the material. Because the emitted phonons carry little energy, it takes many scattering processes and therefore several picoseconds before the temperatures of the free electrons and the material are in equilibrium.

2.3.2 Carrier removal

Once the carriers and the material are in equilibrium, the material is at a well-defined temperature. Although the carrier distribution has the same temperature as the material, there is an excess of free carriers compared to thermodynamic equilibrium. The excess carrier are removed either by recombination of electrons and holes or by diffusion out of the excitation region. Free carrier recombination can either be radiative or non-radiative. In the first case, an electron and a hole recombine emitting a photon with their energy difference (luminescence). This process lowers both energy and density of free carriers, taking place in a timescale of nanoseconds. The non-radiative recombination is an inverse of the impact ionization process: an electron and a hole recombine transferring momentum and energy to a third carrier [61].

2.3.3 Thermal and structural effects

When the free carriers and the material come to an equilibrium temperature and the free carriers have been dissipated due to recombination, the material is essentially the same as that heated by conventional means. Ultrashort laser pulses can achieve this heating in just a few picoseconds. If no phase transition occurs, the temperature reverts back to the ambient value on the timescale of several nanoseconds [62, 63]. If melting or vaporization has occurred, then resolidification or condensation ensues as the temperature falls below the melting or boiling points, respectively; however, the material does not necessarily revert back to its original structure [64].

2.4 Comparison between ultrashort and longer-pulse laser irradiation of transparent materials

For a pulse duration longer than a few tens of picoseconds, energy is being transferred from the laser excited electron plasma to the material on a time scale of the pulse duration. The hot electrons rapidly equilibrate with the material through phonon emission and if the excitation is strong enough, the irradiated region will melt. In this long pulse regime, the absorbed energy is carried out from the focal volume by thermal diffusion. Hence, it is the relative rate of energy deposition and diffusion that determines the damage threshold and it is a well established fact that the fluence necessary to induce optical breakdown scales with the square root of the pulse width τ [1] (Fig. 2.4). The resulting damage is the consequence of melting and boiling of the material and therefore it is spread around the focal volume. Furthermore, the peak laser intensity required to produce the damage is not high enough to directly photoionize electrons, so either thermally excited electrons or impurity and defect states provide the initial seed electrons for the avalanche ionization. Since the breakdown relies on impurity or defect states, its threshold has a non-deterministic nature. For a constant laser fluence near to the threshold some laser shots produce damage while others do not, depending on how many seeds electrons are in the focal volume of each shot.

Conversely, as we have discussed in the previous section, in the ultrashort regime, the pulse duration is much shorter than the time required for the material to heat up to the equilibrium temperature, hence decoupling the absorption and material heating processes. Electrons in the conduction band are heated much faster than they can be cooled by phonon emission. A high density plasma is formed, while the material remains at its initial temperature. Only after the pulse is gone, is the energy transferred to the material, and if the laser energy is above a certain material-dependent energy threshold, permanent structural changes are produced in the material.

In this ultrashort laser regime, the starting point for optical breakdown does not rely on

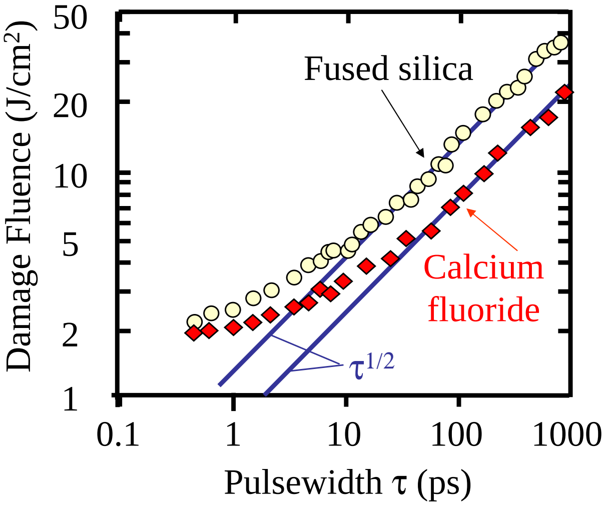

FIGURE 2.4: Dependence of threshold fluence for producing permanent surface damage on pulse width ([1]).

impurity or defect states for the seed electrons to initiate avalanche ionization, which, in this case are provided by photoionization. The threshold for damage therefore has a deterministic nature.

For lasers with a repetition rate of hundreds of kHz, (which is the typical value in commercially available amplified femtosecond system), all the energy absorbed from one pulse is dissipated before the arrival of the following one ($r = 250\,kHz, 1/r = 4\,\mu s$). Since the energy is not coupled into the material by a thermal process, the modified region is very well confined within the focal volume where the threshold is exceeded. On the contrary, for unamplified femtosecond systems, characterized by a repetition rate of tens of MHz, when a pulse hits the material, the energy absorbed from the previous pulse is still diffusing in the material, hence there is a coupling between the excitation due to a pulse and diffusion of the energy deposited by the previous one ($r = 80\,MHz, 1/r = 12.5\,ns$). For this reason, with unamplified femtosecond lasers, the modified volume is spread around the irradiated volume similarly the long-pulse regime, where irradiation and diffusion are coupled mechanisms [34].

2.5 Modelling limitations of femtosecond micro-machining

Since the discovery of the anomalous behaviour of ultrashort irradiation with respect to the longer-pulse regime [1, 65], many other authors dedicated their studies to the modelling of the interactions between ultrashort laser pulses and dielectric materials [13, 66, 67]. However, most of the experiments on dielectric breakdown of transparent materials were done on the surface. In this way, the difficulty of interpretation of the experimental results associated with non-linear propagation of the pulse in the material was avoided [68, 69, 70]. Schaffer et al. [29] proposed a technique to estimate the intensity threshold for bulk damage avoiding the complications due to self-focusing. By maintaining the peak power of the laser below the critical value for self-focusing (2.13), they could accurately calculate the intensity in the focal point and predicted a threshold for silica bulk ionization of $2.8 \times 10^{13}\, W/cm^2$.

However, to be able to have a more general model of the micro-machining of transparent materials, allowing the prediction of the size and shape of the modified regions, all the effects that accompany the propagation of the ultrashort pulses in the glass need to be considered. In the most complete theoretical models presented so far, Equation 2.7 was numerically solved assuming Gaussian propagation of the focused laser beam, and including the effects of self-focusing (2.9), non-linear absorption (2.18), group velocity dispersion and plasma defocusing (2.14) [71, 72]. Using this model, Sudrie et al. [73] related the electron density reached near the focus of the beam to the shape and size of the written structures examined by scanning electron microscopy. They showed that the shape and size of the modified material correspond to the zone where the electron density created by photoionization and avalanche is $\sim 10^{20}\, cm^{-3}$. This model also allowed to study the relationship between the formation of filaments and local refractive index change by fs lasers in silica glass [74, 75]. As discussed in Section 2.1.1, plasma defocusing prevents the collapse of the beam that is predicted by the self-focusing. Instead, a dynamic balance between the two effects leads to a filamentary propagation characterized by a near constant beam waist over many Rayleigh lengths [76]. Indeed, the experimental results showed that the location of the filament corresponds to the profile of the refractive index change.

Although much progress has been made in the last years, a comprehensive theory of non-linear pulse propagation in transparent materials, for pulses whose power exceeds the critical power, is still lacking. For example, Gaussian propagation becomes less accurate in predicting the beam profile under extremely tight focusing. The underlying assumption of the slowly varying approximation becomes questionable when the spatial profile changes considerably on the scale of a wavelength [31]. The lack of an exhaustive model describing the interaction of focused femtosecond pulses in bulk material makes the determination of the intensity threshold of the laser-induced modification of the material difficult to calculate. The laser pulse energy, pulse duration and beam profile are measured outside the sample. If the propagation through the sample did not affect any of these parameters, then the peak intensity in the focus would be simply related to the quantities that are measured externally. As we have seen, the high peak power of the laser pulses induce non-linear propagation effects that strongly distort the spatial and temporal profile of the laser pulse in a manner that is difficult to predict or model [55]. For this reason, although the intensity would be the quantity of interest in the interaction with the bulk material, nonetheless the experimental data of this thesis will be presented as function of the incident pulse energy, which is a measurable quantity.

Chapter 3

Experimental setups

The experimental work presented in this thesis involved the creation of patterns of modified refractive index in optically transparent materials irradiated with femtosecond laser pulses. Section 3.1 describes the setup utilized to "write" the desired structures into the materials. The rest of the chapter illustrates those characterization setups which have been used routinely: the interferometer, home-assembled to measure the modification of the refractive index after the laser exposure (Sec. 3.2), and the setup utilized to verify the presence of uniaxial birefringence in the laser processed regions (Sec. 3.3).

3.1 Direct-writing setup

During the first two years of my PhD, the direct-writing of the samples was performed in the ultra-fast laboratory of the Physics department of the University of Southampton, where I was granted 10% of the available time. The laboratory was equipped with a COHERENT system comprising a $18\,W$ "Sabre" argon ion laser, which pumped a mode-locked Ti:Sapphire oscillator ("Mira"), and a regenerative amplifier "RegA" seeded by the output of the Mira (Fig. 3.1).

The laser beam used for our experiments was extracted from the RegA output and was tuned to an operating wavelength λ_w between $800\,nm$ and $850\,nm$, with $\sim 200\,fs$ pulse duration, $250\,kHz$ repetition rate and pulse energy up to $6\,\mu J$. While the pulse spectrum was monitored with an Oceanoptics spectrum analyzer, no autocorrelator was regularly available and the temporal duration of the beam delivered by the femtosecond amplified source was measured with a COHERENT autocorrelator only during the maintenance days of the laser system (Fig. 3.2).

A mirror mounted on a magnetic base was used to divert the RegA output to the direct-writing setup where a computer controlled shutter regulated the irradiation time,

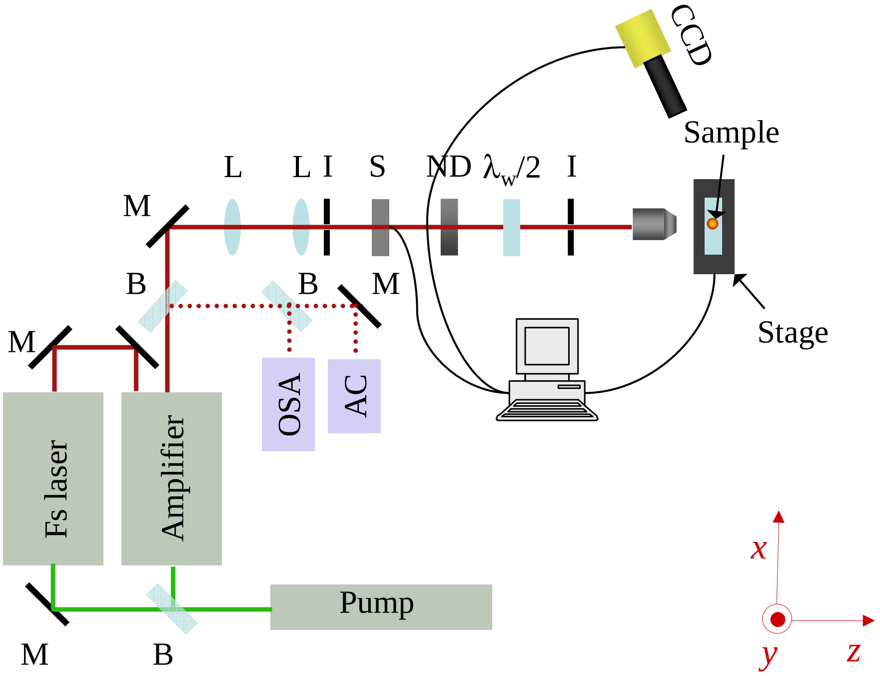

Figure 3.1: Schematic of direct writing setup. M: metallic mirror, L: lenses, I: irises defining the beam path, B: beam splitters, S: shutter, ND: variable neutral density filter, $\lambda_w/2$: half-wave plate, CCD: charge coupled device, OSA: optical spectrum analyzer and AC: autocorrelator.

the incident power was attenuated via a variable neutral density filter, and a half-wave plate allowed the rotation of the linear laser polarization. The laser light was finally focused via either a 50x (NA=0.55) or 10x (NA=0.21) objective into a sample that was mounted upon an Aerotech computer controlled linear motor translation stage with $20\,nm$ resolution in all three directions.

The desired patterns were created in the the bulk of a transparent material by moving the translation stage, while the laser was focused inside sample. This irradiation process is usually defined as laser direct-writing in conparison with a pen tracing on a piece of paper, where the focal point, the index change and the transparent material correspond to the pen-point, the ink and the writing pad. The only differences (apart from the physics involved!) being that, in this case, it is the sample (paper) moving with respect to the laser (pen) and furthermore the process happens into the depth of the material rather than on the surface. Although ideal for line tracing, this technique can also be used to realize uniform areas of index change: whenever required, the area of interest was processed by writing a series of adjacent lines with a spacing between them smaller than a line width. Dedicated computer programs were implemented in HP-VEE to control the stage translations and the shutter (S in Figure 3.1) opening time so that the desired patterns could be “drawn” in an efficient and automated way.

During the last few months of my PhD, the writing setup was moved to the newly opened ORC FAST laboratory. At that time the facility, now one of the biggest in the UK, was

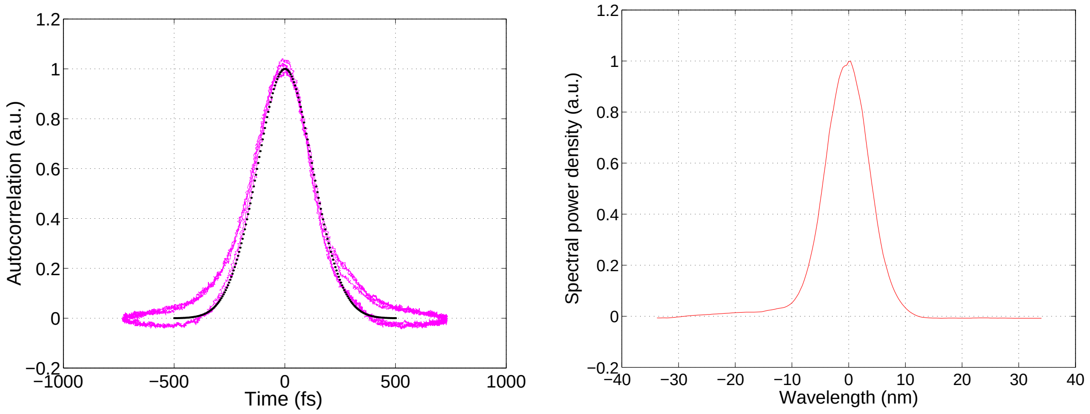

(a)

(b)

FIGURE 3.2: (a): Typical experimental autocorrelation trace of the pulse delivered by the femtosecond amplified source (line) overlapped with the autocorrelation of a sech-squared pulse profile with full width at half maximum $\tau = 200\,fs$ (dotted line). (b): Typical experimental trace of the spectrum of the laser (the full width at half maximum was $9.5\,nm$).

not yet fully equipped, and the available COHERENT system comprised only a doubled frequency diode ("Verdi"), pumping a Mira and a RegA. The reduced pump power ($10\,W$ as opposed to the $18\,W$ delivered by the argon ion laser in the previous setup) required that the oscillator was fixed at the wavelength of maximum gain ($800\,nm$), and in order to accumulate enough gain in the amplifier, the repetition rate was reduced to $100\,kHz$. Finally, also in this laboratory, an autocorrelator was not constantly available, and the pulse duration was measured occasionally. Particular attention was devoted in keeping the system alignment unmodified to avoid changing the pulse duration. Nevertheless, subsequent measurements highlighted a pulse variability from $\sim 200\,fs$ to $> 600\,fs$ over 2 months. The fluctuation of the pulse duration (which is nowadays constantly monitored via an autocorrelator permanently left with the setup) caused difficulties in reproducing the same numerical results in experiments carried out on different days.

3.1.1 Positioning of the sample

To ensure that the sample was squared with respect to the direction of propagation of the writing laser, it was mounted onto two goniometers which allowed tilting in the xz and yz planes respectively. Before a writing process, the focusing objective was temporarily removed and the reflections from the front and back surfaces of the sample were observed on the iris usually positioned before the focusing objective (which was not present during this alignment procedure) (Fig. 3.1). The goniometers were adjusted in turn until the two reflections were overlapped and positioned in the center of the iris (Fig. 3.3).

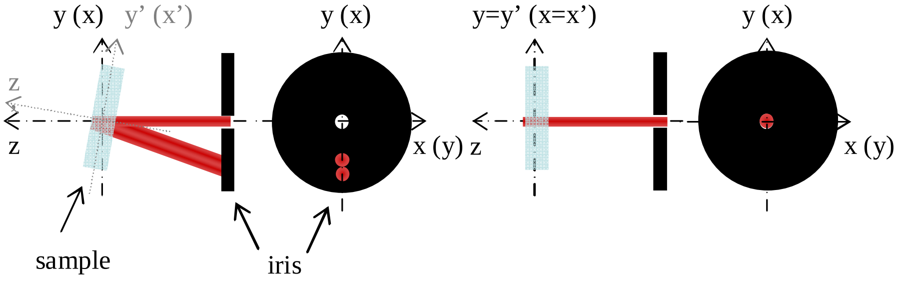

FIGURE 3.3: Schematic of the procedure utilized to ensure that the surface of the sample was perpendicular to the propagation direction of the laser.

Finally, in order to be able to record the directly written structures at the desired depth in the bulk of the material, it was essential to identify the initial position of the sample with respect to the focal spot. The technique utilized was based on the detection of the visible emission, via a CCD camera, generated by the plasma of electrons created during the interaction of the femtosecond laser with the transparent material. This involved focusing the laser onto the front surface of the sample, which was then set as an initial reference position. Throughout this positioning routine the power of the laser was set to the maximum available ensuring the creation of plasma, whilst visible band-pass filters were placed in front of the CCD camera, Figure 3.1, to avoid the laser beam intensity hiding the plasma signal. Finally, the sample was stepped along the z axis, initially towards the focal spot until the visible plasma light could be visually detected on the camera (Fig. 3.4), and subsequently in the opposite direction, causing the disappearance of the signal. The iteration of this procedure, utilizing ever decreasing steps, allowed the determination of the position of the surface of the sample relative to the focal spot to within a few micrometers.

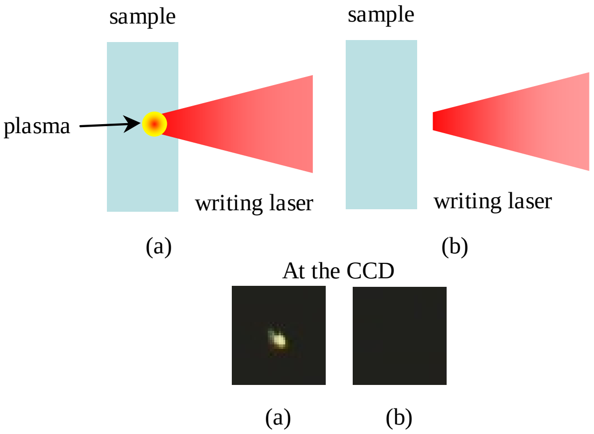

FIGURE 3.4: Typical images recorded at the CCD camera when the laser focal point was inside the material (a), or outside (b).

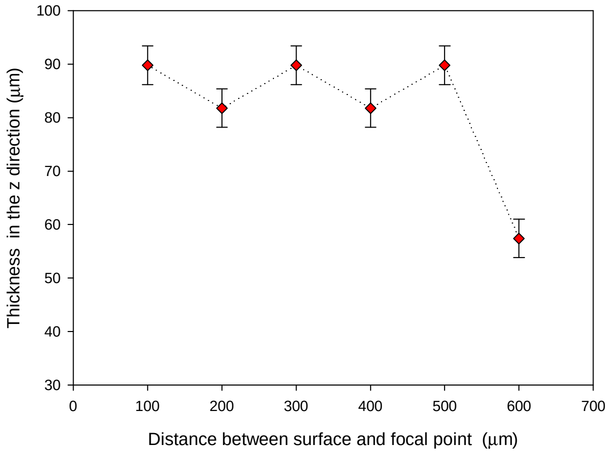

FIGURE 3.5: Thickness of the directly written structures versus the writing depth.

3.1.2 High-NA focusing into materials

When writing structures in the depth of the material it is necessary to consider the aberrations introduced by the objective. It is well known that the presence of an air-glass interface causes the marginal rays to focus late, hence resulting in a blur of the focal point on the axis. This problem has been considered in details in reference [31], where the author, neglecting non-linear propagation effects, calculated the depth at which focusing in silica at a given NA is no longer diffracted limited. The results show that the maximum depth is $900\,\mu m$ at 0.25 NA, $65\,\mu m$ at 0.45 NA, and only $9\,\mu m$ at 0.65 NA. These findings not only add a further complication in the calculation of the intensity at the focal point (Sec. 2.5), but potentially implicate that structures written with the laser focused in different points of the material might have different dimensions. In order to verify how much aberrations affect the dimension of the written structures, the laser ($E_p = 1\,\mu J$, $\lambda_w = 800\,nm$, $\tau \sim 200\,fs$, $r = 100\,kHz$) was focused with the 50x objective at increasing depths ($100\,\mu m$ step in the propagation direction of the laser z) in a platelet of silica glass (Herasil 1). After writing, the sample was polished on the zx plane and the structures were viewed and measured under an optical microscope (Fig. 3.5). Figure 3.5 shows that the dimension of the written structure is constant (within the experimental error of the measurement) for the first $600\,\mu m$ and then eventually decreases.

3.2 Measurement of the modification of refractive index

Whenever a new material was to be studied, a "characterization" sample was fabricated first. It usually consisted of an array of directly-written square structures, each realized with different irradiation conditions to investigate the dependence of the refractive index change versus the laser fluence. The area of each written structure was chosen to be of the order of $(100\,\mu m)^2$ which proved to be an excellent compromise between the optical

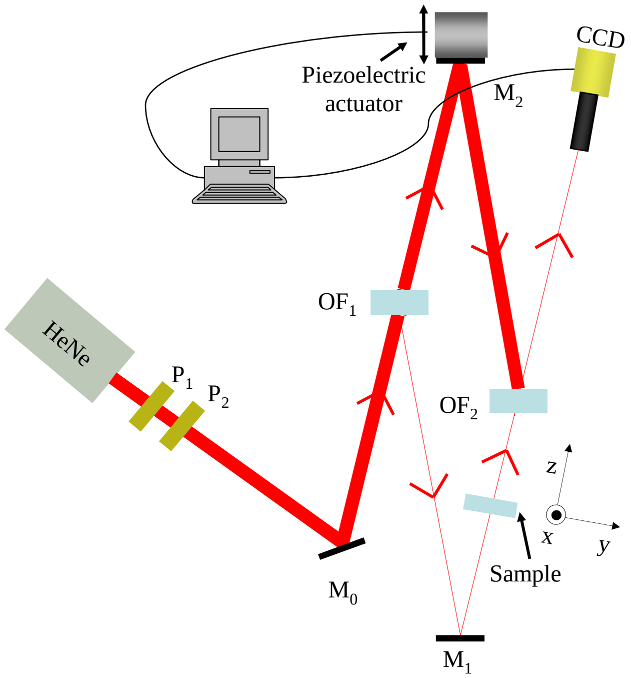

FIGURE 3.6: Schematic of an interferometer to measure changes in index of refraction. OF_1, OF_2: optical flat, M_0, M_1, M_2: mirrors, P_1, P_2: polarizers.

resolution of the setup utilized to measure the index change ($\sim 4\,\mu m$) and the fabrication time. The laser fluence was changed between the writing of one region to the next, either, by controlling the energy delivered to the sample, with ND in Figure 3.1, or by utilizing different focusing objectives or, finally, modifying the speed of the translation stage (s_s). While the first two parameters affect the intensity in the focal volume, the latter controls the time of exposure at a point ($t_{exp} = 2\omega_0/s_s$, with ω_0 the beam waist at the focal point) and hence the number of pulses hitting the same spot ($N_p = rt_{exp}$, with r repetition rate of the laser).

After irradiation, the strength of the laser-induced modification of the refractive index in the written regions was measured using a phase-stepping interferometric technique [77]. An interferometer was constructed as a general characterization tool for our group and it is illustrated in Figure 3.6.[1] A 633 nm He-Ne laser beam is split, by an optical flat OF_1 at the input to the interferometer, into two beams propagating in the reference arm (from OF_1 to OF_2 through M_2) and the fixed arm (from OF_1 to OF_2 through M_1) respectively. The two beams are then recombined at OF_2 and imaged by a CCD camera connected to a frame-grabber card in a computer. The polarization of the laser is set by the direction of P_2, while the average power is controlled by the relative position between P_1 and P_2 (maximum when the two polarizers are parallel and minimum when they are perpendicular). The sample under investigation is positioned in the fix arm of the interferometer, while the optical path of the reference arm is varied by moving mirror M_2 via a computer controlled piezoelectric actuator.

---

[1] The setup and the phase map retrieval algorithms were designed and realized by Dr. B. G. Klappauf.

The intensity I at the exit of the interferometer is given by

$$I =< \mathbf{E_R} + \mathbf{E_F} >, \tag{3.1}$$

where

$$\mathbf{E_R} = \Re\{\mathbf{A_R} e^{-i\omega t}\}, \tag{3.2a}$$

$$\mathbf{E_F} = \Re\{\mathbf{A_F} e^{-i\omega t}\}, \tag{3.2b}$$

with

$$\mathbf{A_R} = \quad \mathbf{a_R} e^{i(kl_R-\delta)} = \begin{bmatrix} a_x e^{-i\delta_x} \\ a_y e^{-i\delta_y} \end{bmatrix} e^{ikl_R}, \tag{3.3a}$$

$$\mathbf{A_F} = \mathbf{a_F} e^{i(kl_F-\delta-\phi)} = \begin{bmatrix} b_x e^{-i\delta_x} e^{i\phi_x} \\ b_y e^{-i\delta_y} e^{i\phi_y} \end{bmatrix} e^{ikl_F}. \tag{3.3b}$$

In (3.3) $\mathbf{a_R}$ and $\mathbf{a_F}$ are the amplitudes of the two fields at OF$_2$, l_R (l_F) is the optical path in air of the reference (fixed) arm, δ specifies the initial polarization state of the laser, and ϕ is the phase retardation acquired by the probe beam in the sample, which will also be referred to as *phase map* of the sample. Using (3.3), (3.1) becomes

$$I = \frac{a_x^2 + a_y^2}{2} + \frac{b_x^2 + b_y^2}{2} + 2a_x b_x \cos[k(l_F - l_R) + \phi_x] + 2a_y b_y \cos[k(l_F - l_R) + \phi_y]. \tag{3.4}$$

from which it is possible to appreciate that the intensity of the interference pattern depends on depends phase difference of the two interfering beams. It is interesting to notice that if the sample is birefringent the phase shifts in the x and y direction will be different ($\phi_x = f_1(n_e, n_o)$, $\phi_y = f_2(n_e, n_o)$). In general, the functions f_1 and f_2 describing the phase terms introduced by a birefringent material versus the ordinary and extraordinary indices of refraction can become rather complicated. Nevertheless, in the case which will be encountered in the following chapters of the thesis, of a uniaxial material with its optical axis along x, then $\phi_x = kn_e t_p$, with t_p thickness of the birefringent material and $\phi_y = kn_o t_p$ (Sec. B.2). Clearly, for an isotropic material $\phi_x = \phi_y = \phi$.

Since the optical path of the reference arm is varied by the movement of the piezoelectric actuator which is stepped through $\sim 2\pi$ in constant steps of $\widetilde{\varphi}$, the intensity at the CCD camera varies in time according to (3.4). Assuming that the probing beam is linearly polarized along x, and that the material is optically isotropic, and considering that $I_R = (a_x^2 + a_y^2)/2$ and $I_F = (b_x^2 + b_y^2)/2$, after the m-th step of the piezoelectric actuator, the intensity is given by

$$I_m = I_{\text{bias}}[1 + V\cos(\varphi_m + \phi)], \tag{3.5}$$

where $I_{\text{bias}} = I_R + I_F$, $V = 2\sqrt{(I_R I_F)}/I_{\text{bias}}$ is the visibility of the fringes, and $\varphi_m =$

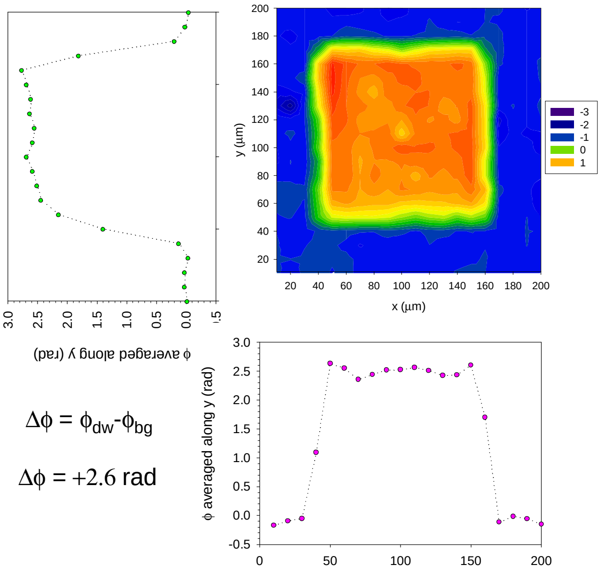

FIGURE 3.7: Phase map ϕ (rad) of the probing light travelling into a direct-written square (center). Graphs representing the cross-section of ϕ on x (bottom) averaged along y, and on y averaged along x (left) normalized to a zero background.

$\varphi_0 + (m-1)\widetilde{\varphi}$ is the variable phase induced by the movement of M_2.

In most of the algorithms presented in the literature, ϕ is calculated using basic trigonometric equations from the combination of three or more intensity frames (3.5) obtained after having calibrated $\widetilde{\varphi}$ to a known value (typically $\pi/2$ or $\pi/4$) [77]. Although conceptually similar, the algorithm utilized in our setup retrieves the phase ϕ from a fitting loop of the experimental intensity frames captured by the CCD after each step of the piezoelectric actuator, with the theoretical behaviour (3.5) leaving I_{bias}, V and ϕ, as free parameters. The output of the fitting loop is a phase map ϕ obtained with the best fit phase parameter. Retrieving the phase from a fitting loop rather than a trigonometric relation loosens the requirement on $\widetilde{\varphi}$, which does not need to be a known value making the technique robust to calibration errors [77].

Figure 3.7 shows, as an example, the phase map of a directly written characterization square in silica glass. The uniform background represents the phase delay of the light travelling in the unprocessed bulk (ϕ_{bg}), while the central region corresponds to the phase acquired traversing the directly-written square (ϕ_{dw}). From the measure of the phase difference $\Delta\phi = \overline{\phi_{dw}} - \overline{\phi_{bg}}$, (where $\overline{\phi_{dw}}$ and $\overline{\phi_{bg}}$ are ϕ_{dw} and ϕ_{bg} averaged in xy), the laser-induced modification of the refractive index Δn can be obtained from the equation:

$$\Delta\phi = \frac{2\pi}{\lambda} t_p \Delta n \tag{3.6}$$

where t_p is the thickness of the written structure. The thickness of the written structure in the direction of the laser propagation was usually measured utilizing calibrated microscope images.

3.3 Setup for the detection of birefringence

The investigation of the presence of laser-induced birefringence and the following determination of the directions of the polarization, became, as it will made more clear in the next chapters, an important routine characterization process. To perform this test, the samples were usually positioned between crossed-polarizers under an optical microscope in transmission mode (Fig. 3.8). The first polarizer selects a direction of polarization from the randomly polarized source, the second, oriented at 90° with respect to the previous, sets the direction of the polarization of the light exiting the system and going to the microscope objective.

From the theory of the propagation of light in a anisotropic material, detailed in Appendix B, we know that in general, the polarization state of light propagating through a birefringent plate, is elliptical (Sec. B.2.1). Hence, if the sample is birefringent, there is a component of the electric field parallel to the second polarizer and a portion of the light coming from the source, and passing through the anisotropic material reaches the microscope objective. When the polarizers are aligned with the directions of the **D** vector in the anisotropic material, then the polarization state is preserved after the propagation through the birefringent plate. In this case, all the light travelling through the birefringent material will be absorbed by the second polarizer. Finally, if the material is isotropic, or if the propagation direction is its optical axis, clearly the polarization is maintained after the propagation through the material and also in this case the light traversing the sample is absorbed by the second polarizer.

Figure 3.9 shows microscope images of a directly-written structure embedded in silica glass acquired with the setup, described in Figure 3.8, by aligning the direction of the polarizers (left), and with the polarizers crossed (right). In the last picture, the dark background corresponds to the unprocessed silica which is isotropic. The light travelling through it was therefore absorbed by the second polarizer. The central white region corresponds to the directly-written structure which is clearly birefringent. The directions of the polarization in the written structure were found by rotating the sample until all the image was uniformly dark.

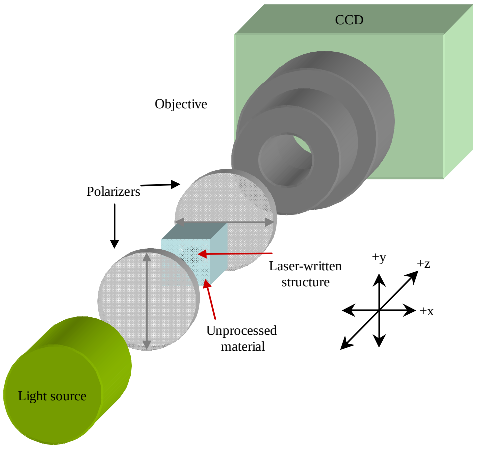

FIGURE 3.8: Schematic of the setup utilized to verify the presence of birefringence in the sample under test.

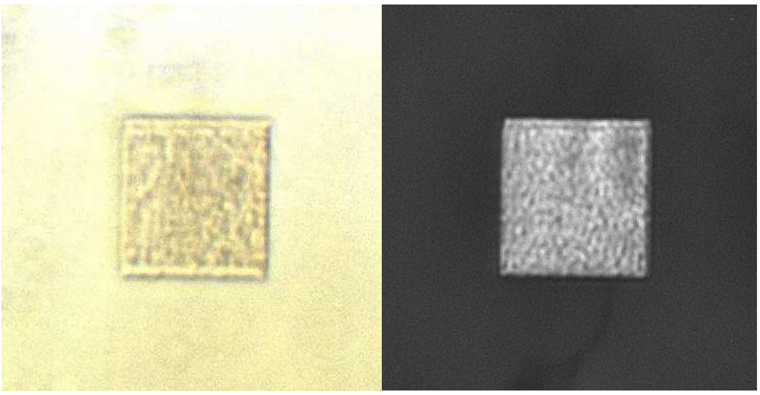

FIGURE 3.9: Microscopic pictures of a birefringent directly-written structure in silica glass: without polarizers (left) and between cross polarizers (right). The writing parameters for this structure (ERB$_4$) are specified on page 47 in Table 5.2.

Chapter 4

Fresnel zone plates fabricated by femtosecond direct writing

FZPs are attractive devices for micro-optics due to their focusing abilities and compactness [78]. However, methods of fabrication are usually based on either lithographic [79] or etching techniques [80], which may be lengthy processes limited to surface patterning. As a demonstration of the potential application of the femtosecond direct writing as a single-step fabrication technique of three-dimensional diffractive optic devices, this chapter reports Fresnel zone plates (FZPs) embedded in silica glass. A short overview of the main properties of the Fresnel focusing devices (FZDs) is summarized in Section 4.1, Section 4.2 reports the fabrication of FZPs by direct writing and in addition, the design of the devices is briefly discussed to give insight into the importance of each parameter involved in the fabrication. Section 4.3 reports the experimental results concerning the focusing properties of the directly written FZPs, while their efficiency and the laser-induced phase retardation are investigated in Section 4.4 and Section 4.5 respectively.

4.1 Fresnel focusing devices

Fresnel zone plates belong to the family of Fresnel focusing devices. As well as the more conventional refractive lenses, FZDs introduce a phase retardation to the incident light wave such that it will converge to a focal point on the axis (Fig. 4.1). But, while "common" glass lenses exploit the refraction of light, FZDs are based on diffraction. This concept may become more clear after comparing the phase retardation due to a refractive lens, $\phi(r)$, and $\phi(r)^{\mathrm{FL}}$, which is the phase shift given by a Fresnel lens (FL),

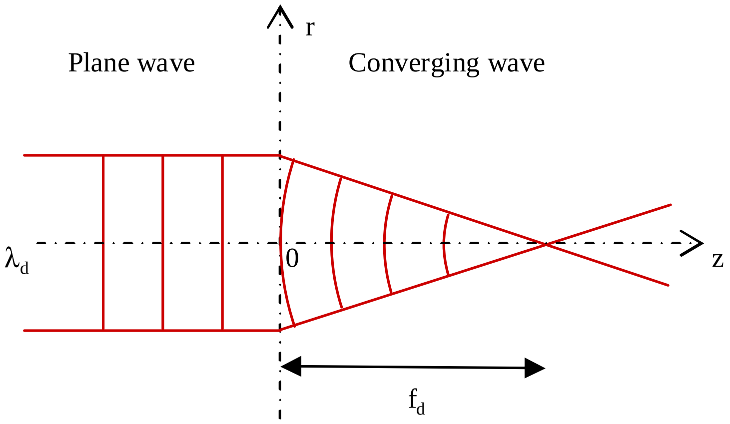

FIGURE 4.1: Schematic of the phase front of a plane wave of wavelength λ_d transformed into a converging wave after travelling trough a focusing element positioned at $z = 0$.

the fundamental device of FZDs (Fig. 4.2 (a)):

$$\phi(r) = \frac{2\pi}{\lambda}\left(\sqrt{f_d^2 + r^2} - f_d\right), \tag{4.1a}$$

$$\phi(r)^{\mathrm{FL}} = \phi(r) + 2m\pi, \quad r_{m-1} < r < r_m, \tag{4.1b}$$

where r is the radial coordinate, f_d is the focal length of the lens (Fig. 4.1), and r_m is the outer radius of the m-th zone of the Fresnel lens (Fig. 4.2 (a)) and is determined by

$$r_m = \sqrt{2mf_d\lambda_d + (m\lambda_d)^2}. \tag{4.2}$$

Equation 4.1b shows that the phase shift of a Fresnel lens is the retardation introduced by a refractive lens modified to have a modulus 2π (Fig. 4.2 (a)). The central ring of a FL is typically larger than the wavelength of light and behaves similarly to a refractive device. Nevertheless, moving away from the center, the period between concentric circles becomes smaller and smaller and the FL acquires the typical features of a circular diffractive grating. Considering the different nature of FLs compared to common lenses, it may be expected that their properties show some distinctiveness. Indeed, Buralli et al. [81] demonstrated that a FL behaves as a lens of infinite number of focal lengths

$$f_n = \frac{\lambda_d f_d}{n\lambda} \quad n \in \mathbb{Z}, \tag{4.3}$$

where λ is any wavelength other than the designed one λ_d. This strong dispersive behaviour is indeed a signature of the diffractive character of the FL.

Besides Fresnel zone lenses, the family of FZDs comprises the *multilevel Fresnel zone plates* (MFZPs). These focusing devices are characterized by a phase profile which is an approximation of the profile of FLs. Figure 4.2 shows the phase of a MFZP for $L = 4$ and $L = 2$, where L indicates the number of discrete levels quantizing the continuous phase profile of the corresponding FL (same λ_d and f_d). Clearly, MFZPs are devices

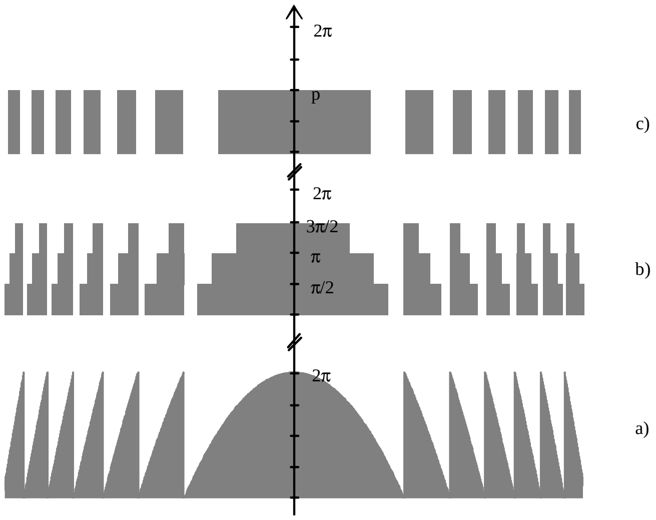

Figure 4.2: Phase profiles: (a) Fresnel zone lens, (b) and (c) multilevel Fresnel zone plates with $L = 4$ and $L = 2$ respectively.

that are more practical to fabricate, nevertheless one may expect that the approximation introduced in the ideal phase retardation profile will affect the efficiency. Indeed, the formula of the efficiency[1] of FLs and MFZPs confirms this intuitive consideration [81, 82]:

$$\eta^{\mathrm{FL}} = \left[\frac{\sin[\pi(1-n)]}{\pi(1-n)}\right]^2 \quad n \in \mathbb{N}, \tag{4.4a}$$

$$\eta^{\mathrm{MFZP}} = \begin{matrix} \left[\frac{\sin(\pi/L)}{n\pi/L}\right]^2 & \text{when } (n-1) \text{ is a multiple of } L, \\ 0 & \text{otherwise.} \end{matrix} \tag{4.4b}$$

It is interesting to note that if $\lambda = \lambda_d$, then $\eta^{\mathrm{FL}} = 1$ for $n = 1$ and it is zero for all other orders. Thus, FLs have a 100% diffraction efficiency for the design wavelength and a single focal length. On the other hand, multilevel Fresnel zone plates (MFZPs) always display higher order foci in addition to the primary focus. The theoretical diffraction efficiency of the primary focus of a MFZP versus the number of levels is shown in Figure 4.3 where it can be appreciated that starting from $4/\pi^2$ for $L = 2$, it quickly approaches unity (e.g. for $L = 4$, η^{MFZP} is already equal to 0.81).

The two level approximation of the FL's profile ($L = 2$) reduces to the well known *phase-reversal* Fresnel zone plate (FZP), realized by Wood [83] acting on a suggestion by Lord Rayleigh. Their aim was to improve the original design of the Fresnel focusing elements conceived by Soret [84], the so called *amplitude* Fresnel zone plates in which every other zone was screening the incident radiation in an overall diffraction efficiency, at the primary focal length, of only 10%.

---

[1] The efficiency being defined as the ratio of light flux in the area of the image and the light flux on the lens aperture.

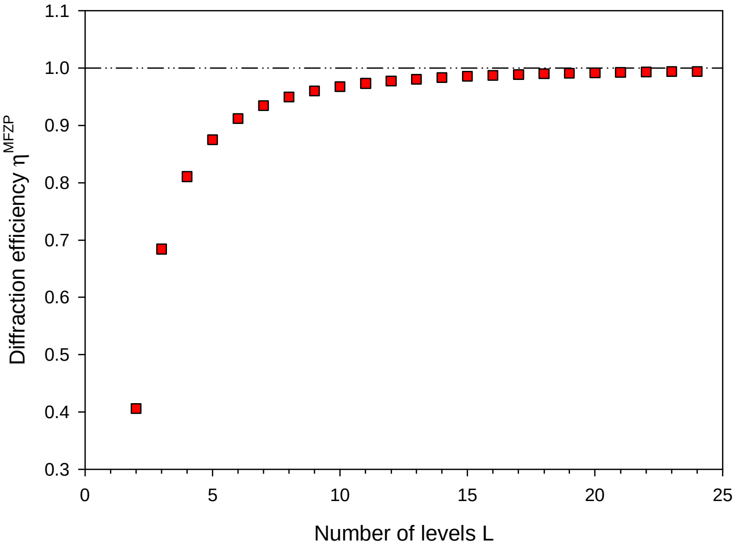

FIGURE 4.3: Diffraction efficiency of the first order (principal focus) versus the number of discrete levels L for MFZPs.

Together with the efficiency the other important parameter of a focusing device is its optical resolution [85], which for a FZDs is given by

$$\delta_n = 1.22\frac{\Delta r}{n}, \tag{4.5}$$

where δ_n is the FWHM (full width at half maximum) of the Airy disk (the central maximum of the diffraction pattern from a circular aperture) at the focal plane for the n-th diffraction order and Δr is the outermost zone width of the FZD device given by

$$\begin{aligned}\Delta r = &\sqrt{2\lambda_d f_d \frac{LM/2 - L + 1}{L} + \left(\lambda_d \frac{LM/2 - L + 1}{L}\right)^2} + \\ &- \sqrt{2\lambda_d f_d \frac{LM/2 - L}{L} + \left(\lambda_d \frac{LM/2 - L}{L}\right)^2},\end{aligned} \tag{4.6}$$

where M is the number of Fresnel rings. Clearly, the best optical resolution is achieved for the minimum value of Δr which is limited by the writing resolution of the fabrication technique (l_w).

4.2 Design and fabrication of directly written FZPs

As shown in Figure 4.2, to fabricate a FZP it is necessary to induce a phase retardation of π between odd and even numbered Fresnel zones. This can be achieved, either by modulating the thickness of the material, or by modifying the index change. We utilized the direct writing setup described in Section 3.1 to create regions of index modification within the bulk of commercial silica (Herasil 1). At the time of the experiments described in this chapter, the femtosecond system was tuned to 850 nm, it was operating at 250 kHz with a pulse duration of $\sim$ 200 fs and it was linearly polarized along x. In order to optimize the writing resolution, we chose to utilize the strongest focusing objective we had available (50x, NA=0.55). From previous experimental results we were expecting a writing resolution $l_w \sim 3\,\mu m$ (Sec. 5.1).

The sample (50x50x2 mm) was mounted on the translation stage with its main faces perpendicular to the z-axis, and the focal point was positioned 100 μm inside the silica plate (Sec. 3.1.1). A HP-VEE computer program was written to control the movements of the stage and the actuation of the shutter so that the sample was translated in circles of ever increasing radius inside the odd numbered Fresnel rings while the shutter was open. In order to ensure that the written zones were processed uniformly by the laser, without any gap between two adjacent circles, the spacing p between them was chosen to be smaller than the writing resolution ($p = 1\,\mu m$). After a Fresnel zone was written, the sample was translated towards the next zone to be processed. During the linear translation between two odd numbered zones, the shutter was closed and hence, the even numbered Fresnel rings were untouched by the laser.

Figure 4.4 shows a microscope image of the central region of a Fresnel zone plate (FZP$_\mathrm{A}$) created by the direct write method. The energy per pulse was set to the maximum available at the time of fabrication ($E_p = 0.73\,\mu J$), with the intent to induce the highest phase shift possible with the setup in use, and the stage was translated at a constant speed of 400 $\mu m/s$. This particular zone plate has a maximum radius of 1 mm, 158 zones, and was designed to focus light with wavelength $\lambda_d = 632.8\,nm$ at a length of 1 cm in air. Considering that the lens is embedded in a silica platelet of 1 mm, the effective focal length is expected to be 1.02 cm (See inset of Figure 4.7).

When designing a FZP, for a chosen wavelength λ_d and focal length f_d, M is the last

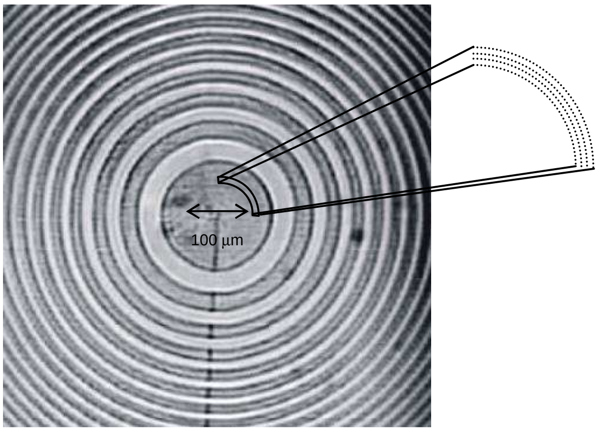

Figure 4.4: Microscope image of the central part of Fresnel zone plate A, directly written in silica by femtosecond laser. The inset represents a schematic of the fabrication technique used to process the written zones by writing adjacent circles with a spacing, p, of 1 μm.

parameter defining the device. In addition, the fabrication technique introduces more parameters to consider, namely the fabrication time, the stage translation speed, and the spacing p between adjacent lines forming a uniform area. The number of Fresnel zone rings affects the optical resolution following (4.5) and ideally, the maximum M allowed by the writing resolution l_w (4.6), should be preferred. On the other hand, the fabrication time is approximately given by the sum of the translation times between odd Fresnel zone rings and the ratio between all the circular trajectories written in the sample over the speed of the translation stage. Consequently, it can be reduced either by limiting the numbers of written circles, or by increasing the writing speed. Nonetheless, it might be expected, (as will be confirmed later in Section 5.5.2) that the retardation induced by the laser may depend on the translation speed, adding a further coupling condition to the parameters involved in the design of the device. Finally, the spacing p affects the precision of the Fresnel rings profile. In general, the fact that an area needs to be processed by writing adjacent lines of finite dimension l_w introduces an error on the width of the laser processed zones. The mismatch between the ideal width and the experimental one, leads to a phase error:

$$e_\phi = |\phi^{\mathrm{FZP}} - \phi^{\mathrm{exp}}_{\mathrm{FZP}}|, \tag{4.7}$$

where $\phi^{\mathrm{exp}}_{\mathrm{FZP}}$ is the phase retardation introduced by the fabricated FZP. The phase error e_ϕ was calculated for different values of p ($1\,\mu m$, $0.5\,\mu m$ and $20\,nm$) and with $f_d = 1\,cm$, $\lambda_d = 632.8\,mn$ (as in FZP$_\mathrm{A}$) and $M = 179$, which, from (4.6), is the maximum number of Fresnel zones allowed by a writing resolution of $l_w = 3\,\mu m$ (Fig. 4.5). As expected e_ϕ decreases for smaller values of p, nonetheless it may be noticed that even for $p = 1\,\mu m$ it is well below $\pi/2$, and hence within the Rayleigh's criterion for negligible phase error

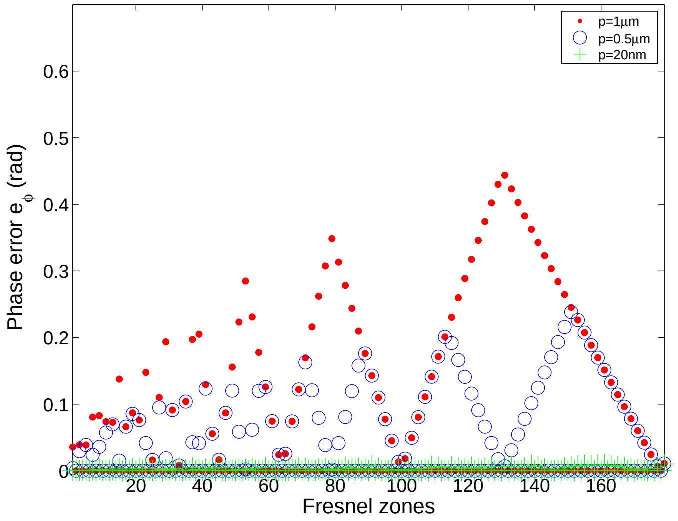

FIGURE 4.5: Phase error e_ϕ introduced by the fabrication technique and calculated for $p = 20\,nm$ (green), $p = 0.5\,\mu m$ (blue) and $p = 1\,\mu m$ (red).

[86]

$$| e_\phi | < \frac{\pi}{2}. \tag{4.8}$$

Although a smaller value of p leads to a better phase profile, nonetheless it also increases the number of circles written in each processed zone and hence extends the fabrication time.

The final design of a FZP fabricated by femtosecond direct writing is the best compromise between all these parameters, and it depends on the most stringent requirement. In our case, we wanted to minimize the fabrication time in order to ensure stability of the laser over the writing process, and the choices made of scanning the Fresnel zones at a speed of $400\,\mu m/s$, having $M = 158$ rings, and spacing adjacent lines of $p = 1\,\mu m$, led to a fabrication time of only 90 minutes.

4.3 Experimental characterization of the focusing properties of the FZPs

To determine the properties of the FZP fabricated with this femtosecond direct writing technique, the position of the primary and secondary foci was measured with the setup shown in Figure 4.6. Line filters were used in turn with a white-light source to select specific wavelengths ($488\,nm$, $550\,nm$, and $642\,nm$). An objective mounted upon a translation stage was moved along z to find the positions of the foci, and a CCD camera was used to image the intensity distribution on the focal plane of the objective. The results are displayed in Figure 4.7, where the focal positions (points) are compared to theoretical plots (lines) obtained from Equation 4.3, taking into account the dual media of silica and air (See inset in Fig. 4.7). As can be seen, the experimental results are within 1% of the theoretical value for all wavelengths at the primary and secondary foci. However, although the theory predicts only a series of odd numbered secondary foci at $f/3$, $f/5$ etc. (4.4b), in our FZPs there are also identifiable even numbered secondary foci at $f/2$ and $f/4$. This anomaly can been explained in terms of the Fresnel zones having slightly unequal areas [87]. As we have seen, in the case of the directly written

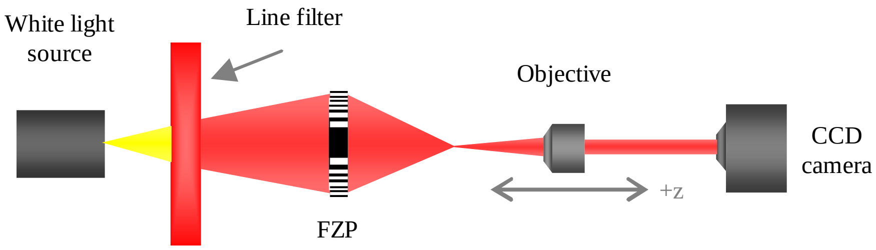

Figure 4.6: Schematic showing the setup used to record the focal lengths of both primary and secondary foci.

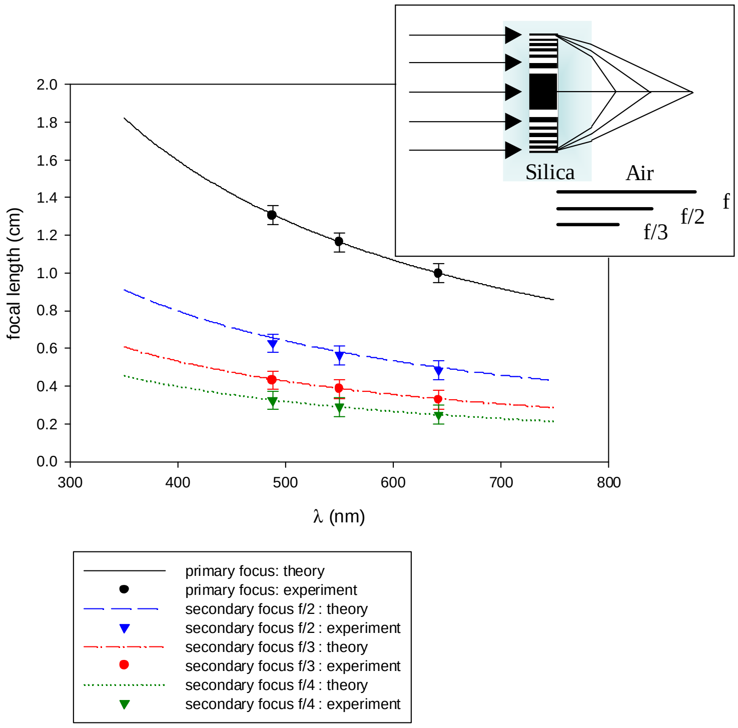

FIGURE 4.7: Measured focal lengths (points) and theoretical focal lengths (lines) of FZP_A.

zone plates described here, the fabrication error on the zone width is ascribable to the technique used to process an area by writing adjacent lines with a spacing between them of p.

To measure the size of the focused spot, a GENTEC silicon beam scope was positioned in the setup of Figure 4.6. By scanning its “finger” across a laser beam, this device enables the visualization of the incident irradiance profile. The instrument is equipped

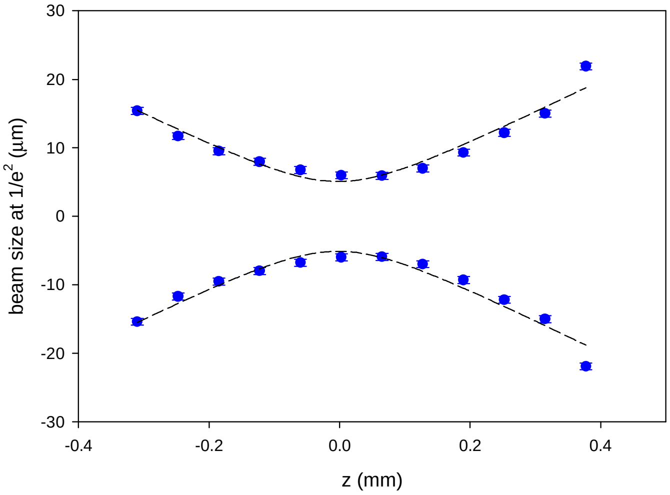

FIGURE 4.8: Experimental measurement of the beam waist of a He-Ne beam after traversing $\text{FZP}_\mathbf{A}$.

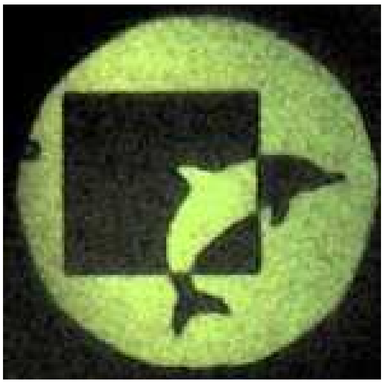

FIGURE 4.9: Image of the Southampton University logo produced by a femtosecond directly written Fresnel zone plate (FZP$_\mathrm{A}$).

with software capable of performing the calculation of the best fit of the measured profile with a Gaussian curve and provides the value of the beam radius at the $1/e^2$ of the intensity curve. The white light and line filters in the setup of Figure 4.6 were replaced by a $633\,nm$ He-Ne laser illuminating the FZP and the size of the beam was measured at the plane of the FZP ($2w_{1/e^2}(-f) = 577\,\mu m$). Then, the beam scope was mounted on a translation stage and stepped along the z-axis in the vicinity of the expected focal point of the lens and the waist of the focusing beam was measured at each step (Fig. 4.8). Finally, the experimental points were fitted with the theoretical focusing behavior of a Gaussian beam and this procedure allowed the calculation of the focal spot $w_{1/e^2}(0) = 5.1\,\mu m$ [88]. Equation 4.5 predicts a focused beam width of $3.9\,\mu m$ ($w_{1/e^2} = w_\mathrm{FWHM}/\sqrt{2\ln 2}$) which is one micron smaller than the experimental result.

To visually demonstrate the focusing quality of the directly-written Fresnel zone plate, Figure 4.9 shows an image of the Southampton University logo produced by FZP$_\mathrm{A}$. The logo was illuminated with a white light source transmitted through the line filter selecting $550\,nm$ and imaged by the zone plate. The focal plane was imaged via a CCD camera.

4.4 Birefringence and efficiency

In order to verify if the laser had induced birefringence in the written regions, the FZPs were positioned between two crossed polarizers (See Section 3.3 for details). The image shown in Figure 4.10 refers to a different Fresnel zone plate (FZP$_\mathrm{B}$), and it clearly shows that the laser processed zones are birefringent. FZP$_\mathrm{B}$ was written with an energy per pulse $E_p = 0.87\,\mu J$ slightly higher than that of FZP$_\mathrm{A}$, but at the same writing speed ($400\,\mu m/s$). It was designed to focus light with wavelength $632.8\,nm$ at a distance of $2.4\,cm$ and has 70 Fresnel zones. The dark zones in the image correspond to the even numbered Fresnel rings of pure silica, whereas the bright ones are the birefringent laser processed areas. Despite the different energy utilized during writing, both FZPs showed

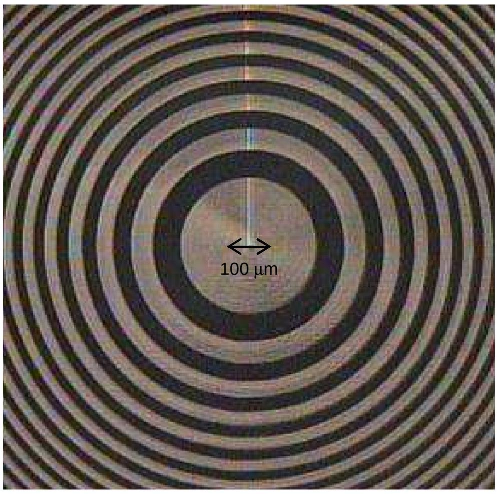

Figure 4.10: Microscope image of the central part of $\mathrm{FZP_B}$ positioned between cross polarizers.

birefringence.

As was explained in Section 3.3, the directions of polarization inside the anisotropic material can be found by rotating the FZPs, positioned between the two crossed polarizers, until the light traversing the birefringent regions is absorbed in the second polarizers and consequently, all the microscope image is uniformly dark. This assures that the directions of **D** are aligned with the polarizers. It was found that the polarization was parallel (e) and orthogonal (o) to the direction of the polarization of the laser used to write the device. This is in agreement with the results published in [46], where it was reported that directly written zones, processed in silica above a certain threshold intensity, display uniaxial birefringence and the optic axis is parallel to the direction of the polarization of the writing laser. Consequently, when the light is propagating along the z-axis, the extraordinary wave is vibrating along x with a phase velocity $v_p = c/n_e$ and the ordinary along y ($v_p = c/n_o$) (Appendix B). It follows that different polarizations of light incident on the Fresnel plates will experience a different phase retardation as the light passes through the directly written regions.

Table 4.1 elucidates these properties by showing a range of efficiencies measured as a function of wavelength and polarization for $\mathrm{FZP_A}$ and $\mathrm{FZP_B}$. The efficiency of the FZPs was measured with the setup of Figure 4.6, connecting a beam profiler to the CCD camera. The software available with the instrument allowed a region of the picture to be selected as the domain of the integration of the intensity collected on the CCD. The efficiency was finally calculated as the ratio of power in each primary focus over the total power transmitted by the zone plates. It is interesting to note, by examination of Table 4.1, that a wide range of efficiencies for $\mathrm{FZP_A}$ and $\mathrm{FZP_B}$ are produced for the variety of wavelengths and polarizations tested. This is due to the varying degrees of constructive/destructive interference given by the phase variations induced by the index modified zones. As mentioned above, FZPs have a theoretical maximum efficiency of

Zone plate	**λ (nm)**	**Polarization**	**Efficiency (%)**
A	**404**	e	28
	404	o	7
	550	e	24
	550	o	4
	642	e	17
	642	o	3
B	**404**	e	39
	404	o	11
	550	e	34
	550	o	10
	642	e	26
	642	o	9

Table 4.1: Experimental results on efficiency for $\mathrm{FZP_A}$ and $\mathrm{FZP_B}$ for given interrogating wavelengths and polarization.

approximately 40% assuming a variation of π and 100% transmission through the zone plate (Equation 4.4b). This can be compared to absorbing zone plates that have a maximum efficiency of just 10% [86]. With a maximum efficiency recorded of 39%, our results therefore indicate that the directly written zone plates behave as phase lenses. The intensity transmission coefficient (the ratio between the power transmitted by the lens and incident on it) was in fact measured to be $\sim 96\,\%$.

4.5 Measurement of the phase retardation

Finally, the phase retardation induced by the laser was measured with the interferometric setup described in Section 3.2. For each FZP the phase retardation was measured with the probing $633\,nm$ He-Ne polarized parallel to the optic axis of the birefringent structure ($\Delta\phi_e$) and perpendicular to it ($\Delta\phi_o$). The results are summarized in Table 4.2 and Figure 4.11. As expected from the efficiency results reported in Table 4.1, the phase retardation of light at the design wavelength is smaller than π, and more precisely almost $\pi/2$, suggesting that it may be possible to achieve an efficient FZP for $\lambda_d = 633\,nm$ by writing two identical adjacent FZPs at different depths (z) of the material, i.e. by combining the modulations of the index change and the thickness of the processed material.

Zone plate	**$\Delta\phi_e$ (rad)**	**$\Delta\phi_o$ (rad)**
A	-1.35 ± 0.05	-0.2 ± 0.05
B	-1.37 ± 0.05	-0.2 ± 0.05

Table 4.2: Experimental results on the phase retardation for $\mathrm{FZP_A}$ and $\mathrm{FZP_B}$ for a given polarization.

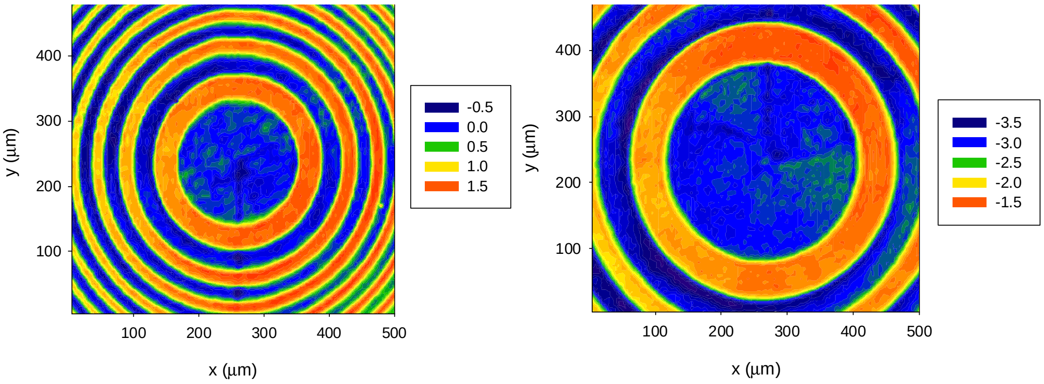

FIGURE 4.11: Phase retardation $\Delta\phi_e$ (rad) of the central part of $\mathrm{FZP_A}$ (left) and $\mathrm{FZP_B}$ (right) obtained with the interferometric setup described in Section 3.2.

Unexpectedly, the measurement of the phase shift induced in silica, revealed that the laser-induced index modification is *negative*. This is a rather surprising result, as most of the published work related to femtosecond writing in silica glass demonstrates guiding structures, hence characterized by a *positive* index change. Our findings seem to suggest that there is an irradiation regime which leads to anisotropic directly written structures characterized by a negative index change. This newly observed type of structure will be studied in the next chapter.

4.6 Conclusions

Exploiting the ability of femtosecond lasers to modify the index change of the processed material, we fabricated phase-reversal FZPs embedded in silica. This process offers advantages over current zone plate fabrication techniques since it is a one-step procedure enabling the creation of three dimensional diffractive optics components.

The focusing properties of the directly written FZPs compare well with the theoretical behaviour and the high efficiencies described in Section 4.4, with a maximum of 39%, indicate that phase variations between alternate zones of $\sim \pi$ can be achieved for particular wavelengths. The additional result demonstrating efficiencies that vary by a factor of up to $\sim$6 for orthogonal polarizations, may be useful for integrated optical circuits that require both focusing and polarization sensitive properties.

Nonetheless, the lack of information on the dependance of the laser-induced modification of the refractive index versus the laser fluence, makes it difficult to achieve the desired phase retardation at the design wavelength. Since the femtosecond direct writing is a relatively new technique, few studies have been carried out on this extremely important parameter and, therefore, it will be the main focus of the following chapters. Moreover, it was observed that the written structures were birefringent and showed a negative index change with respect to the unprocessed material. This is a new result in contrast with the previously reported measurements of a *positive* femtosecond laser modified refractive index, furthermore underlying the need to investigate in more details the response of the material to the laser irradiation.

Chapter 5

Femtosecond direct written structures of type I-fs and type II-fs

The results presented in the previous chapter highlighted how the lack of data regarding the characteristics of the modification induced in the bulk of transparent materials by the femtosecond direct writing, is a limiting factor in the efficient design and fabrication of photonic devices. This reason motivated the studies reported in this chapter, which were originally aimed to characterize the principal features of the laser written structures (i.e. the dimensions and the refractive index change). Nevertheless, the observation of new phenomena led to the discovery of a type of femtosecond written structure (type II-fs) characterized by birefringence, anisotropic reflection, and negative index change, which later became the main focus of our investigations.

Section 5.1 reports the experimental measurement of the writing resolution, l_w, versus the energy level used to irradiate the material. Further investigations on the sample, realized to measure l_w, showed evidence of a new anisotropic property, consisting of a reflection from the modified regions that only occurred in the direction corresponding to the polarization of the writing laser (Sec. 5.2). Section 5.3 details the dependance of the laser-induced modification of the refractive index versus the laser energy. We observed that, in silica glass, the refractive index change becomes negative at high pulse energy. The reported results demonstrate that uniaxial birefringence, anisotropic reflection and negative index change onset at the same intensity threshold. In addition, it is shown that some of the birefringent structures display a surprising characteristic, namely the sign of the index change is *positive* for the ordinary wave but *negative* for the extraordinary wave. All these newly observed phenomena are explained or justified in Section 5.4, where a sub-wavelength self-assembled periodic structure is ascribed as the common cause behind the experimental observations. Section 5.5 shows how the

SAMPLE JM3

Energy (μJ)	**Polarization**	**Line name**	$\mathbf{l_w^M}$ **(μm)**	$\mathbf{l_w^m}$ **(μm)**	$\mathbf{t_p}$ **(μm)**
0.24	y	JM3$_{1y}$	1.0 ± 0.1	1.0 ± 0.1	13 ± 2
	x	JM3$_{1x}$			
0.36	y	JM3$_{2y}$	1.7 ± 0.1	1.0 ± 0.1	24 ± 1
	x	JM3$_{2x}$			
0.48	y	JM3$_{3y}$	2.5 ± 0.1	1.4 ± 0.2	55 ± 3
	x	JM3$_{3x}$			
0.61	y	JM3$_{4y}$	3.6 ± 0.1	1.6 ± 0.4	60 ± 1
	x	JM3$_{4x}$			

TABLE 5.1: Some fabrication details of the sample JM3, written with the setup described in Section 3.1, with $\lambda_w = 850\,nm$, $r = 250\,kHz$, $\tau \sim 200\,fs$, $s_s = 200\,\mu m/s$ in y. s_s: Direction of travel of the translation stage. The laser was focused via a 50x objective (NA=0.55). This table also reports the experimental measurement of the maximum and minimum line widths (l_w^M and l_w^m respectively), and of the thickness t_p of the lines along the z-axis (See Fig. 5.1 for details).

transition between the written structures belonging to type I-fs and type II-fs onsets at a certain intensity threshold. Finally, after considering the repeatability of the experimental results in Section 5.6, the thermal stability of the femtosecond written structures is investigated in Section 5.7.

5.1 Writing resolution

In order to study the dependence of the laser resolution on the pulse energy, a series of lines (length $700\,\mu m$) was written inside silica glass (Herasil 1) at a depth of $100\,\mu m$ below the front surface. The femtosecond laser system used for the writing setup was configured with the same experimental conditions as used for the fabrication of FZPs ($\lambda_w = 850\,nm$, $r = 250\,kHz$, $\tau \sim 200\,fs$ Sec. 3.1). The light was focused by a 50x objective, with energy per pulse ranging from $0.24\,\mu J$ down to $0.61\,\mu J$. Pairs of adjacent

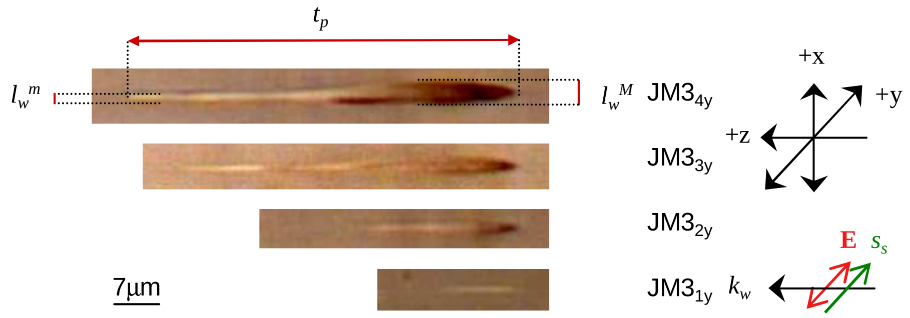

FIGURE 5.1: Microscope images of some of the directly written lines embedded in silica (Sample JM3, see Tab. 5.1 for details). k_w: laser wave vector. **E**: Polarization direction of the writing laser.

lines were written with the same energy level, but with orthogonal polarization of the writing laser (see Table 5.1 for details). In every case, the speed of writing was $200\,\mu m/s$ along the y-axis.

After writing, the sample's edges (on the xz and yz planes) were polished and used to view the interior of the silica plate, using a microscope incorporating a CCD camera (Fig. 5.1). During inspection, the structures were illuminated, with a randomly polarized white light source, in the y-direction from below the sample, i.e. with the microscope in transmission mode. These images were utilized to measure the line width l_w and the dimension t_p on the z-axis; the experimental results are reported in Table 5.1. One may expect that the modified region corresponds to the focal spot of the focused beam (beam radius in x and confocal parameter in z). However, observing Figure 5.1, it can be noticed that t_p increases with the pulse energy and that, even for $\mathrm{JM3}_{1y}$, written at the lowest energy level, t_p is greater than the confocal parameter, b. The confocal parameter of a Gaussian beam is defined as twice the Rayleigh range [31]

$$z_R = \frac{\pi \omega_0^2 n_{bg}}{\lambda_w}, \tag{5.1}$$

where ω_0 is the beam radius at the focal point. Neglecting aberrations and non-linear effects the beam waist at the focal point is given by

$$w_0 = \frac{\lambda_w}{\pi} \frac{\sqrt{1 - \mathrm{NA}^2}}{\mathrm{NA}}. \tag{5.2}$$

Equations (5.1), and (5.2) give $b = 2.1\,\mu m$, and $2\omega_0 = 0.9\,\mu m$ (NA $= 0.5$, and $\lambda_w = 850\,nm$), which do not correspond to the measured values of t_p and l_w respectively. In addition l_w is not constant along the beam propagation direction z; the first region of the cross-section of the written lines is characterized by a larger width, followed by a diffraction limited filament. In Table 5.1, we defined the maximum and minimum width as l_w^M and l_w^m respectively. Thus, we can establish that the writing resolution of the FZPs was $\sim 3.6\,\mu m$ and it can be reduced by decreasing the energy level delivered to the sample. However, anticipating the results reported in Section 5.3, the value of the laser-induced index change will decrease accordingly.

To justify the shape of the lines and their dimensions it is necessary to take into consideration the propagation of focused pulses in transparent material. Indeed, our results are in excellent agreement with the experimental and theoretical results reported in [46, 73], where the non-linear Shrödinger equation was numerically solved assuming Gaussian propagation of the focused laser beam, and including the effects of self-focusing, non-linear absorption, group velocity dispersion and plasma defocusing. As mentioned in Chapter 2, their results demonstrated that the shape and size of the modified material correspond to the zone where the electron density created by photoionization and avalanche is close to $10^{20}\,cm^{-3}$.

Finally, it can be observed in Figure 5.1 that, the lines written at higher energy appear of a red color when viewed with an optical microscope. This effect can be ascribed to scattering losses, which would scatter the shorter wavelengths of the light source more efficiently than the longer ones. The intensity transmission coefficient for the FZPs (written in similar irradiation conditions as $JM3_{4y}$) was measured to be ~ 0.96.

5.2 Anisotropic reflection

Surprisingly, when the directly written lines of the sample JM3 were viewed with the microscope in reflection mode, i.e. from above (through the microscope objective), a striking reflection in the blue spectral region was observed from some of the lines. Closer analysis revealed that the reflection only occurred when the viewing axis was both parallel to the electric field vector of the writing beam and the structure was written with an energy per pulse greater than $E_p = 0.24\,\mu J$. When the lines were viewed along the y direction, only $JM3_{2y}$, $JM3_{3y}$, $JM3_{4y}$ were reflecting blue light, while when illuminated in x, it was instead $JM3_{2x}$, $JM3_{3x}$, $JM3_{4x}$ displaying the blue reflection, i.e. no reflection is observed if viewing the written structures perpendicular to the direction of the writing **E** field (Fig. 5.2). *This indicates that the observed reflectivity is both energy dependent and anisotropic.*

Figure 5.3 displays the microscope image of the reflection from the lines created with a pulse energy of $0.48\,\mu J$ ($JM3_{3x}$, and $JM3_{3y}$). The illuminating light incident from above the sample through a viewing objective was set to an intensity level that ensured that the line itself was not imaged. The position of the written lines relative to the focus of

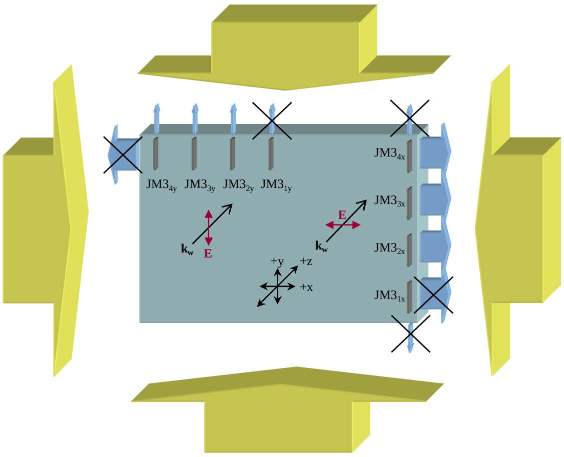

FIGURE 5.2: Schematic showing the anisotropic reflection from directly written lines. Reflection only occurs for incident light parallel to the electric-field vector of the writing laser. k_w: laser wave vector. **E**: Polarization direction of the writing laser. In the drawing, the position of the lines relative to each other and to the sample is for clarity purposes only and it is not representative the real position of the structure in the silica plate.

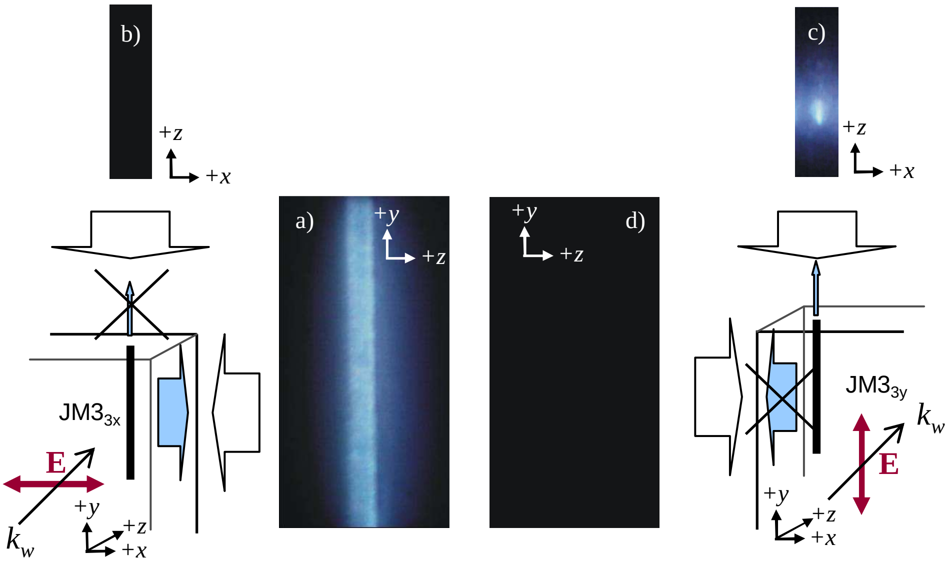

FIGURE 5.3: CCD camera images of the reflection from some directly written lines (**E**: polarization orientation). Reflection from JM3$_{3x}$ on (a): the yz plane and (b): the xz plane (no reflection). Reflection from JM3$_{3y}$ on (c): the xz plane and (d): the yz plane (no reflection).

the microscope objective was checked beforehand by illuminating from below, when the structure could be clearly observed. Figure 5.3 (a) shows the reflection from the side of JM3$_{3x}$; the resulting image of the same line, viewed in the orthogonal direction, was devoid of any reflected light (Fig. 5.3 (b)). Similarly, Figure 5.3 (c) shows the reflection from JM3$_{3y}$ viewed from above, while Figure 5.3 (d) images the absence of reflection from the side of the same line. The two lines JM3$_{3x}$ and JM3$_{3y}$, are identical as they were written exactly under the same experimental conditions, except for the direction of the polarization of the writing laser (Tab. 5.1), however, they reflect blue light in different directions (parallel to the direction of the writing laser). This observation clearly demonstrates that the written structures have been modified with a permanent reflective characteristic dependent upon the writing laser's polarization.

Next we wished to test the birefringent behaviour of the structures, therefore the silica plate was positioned between crossed polarizers to enable the regions of birefringence to be identified (Sec. 3.3). This analysis revealed that the onset of birefringence occurred at a pulse energy greater than $E_p = 0.24\,\mu J$, i.e. the same energy threshold as for the appearance of the anisotropic reflection. In Figure 5.4 the microscope images of the birefringence of the directly written lines, written with the polarization in y, are shown (left) together with the pictures displaying the reflection from the same lines (right). The first line from the bottom, written at lower energy (JM3$_{1y}$) is the only one not birefringent (together with JM3$_{1x}$, written at the same energy level, but not displayed in the figure). In all the birefringent lines, the polarization directions were found to be along x and y, in agreement with the results found in Section 4.4 for the FZPs. The images on the right of Figure 5.4 demonstrate that the blue reflection could be detected only

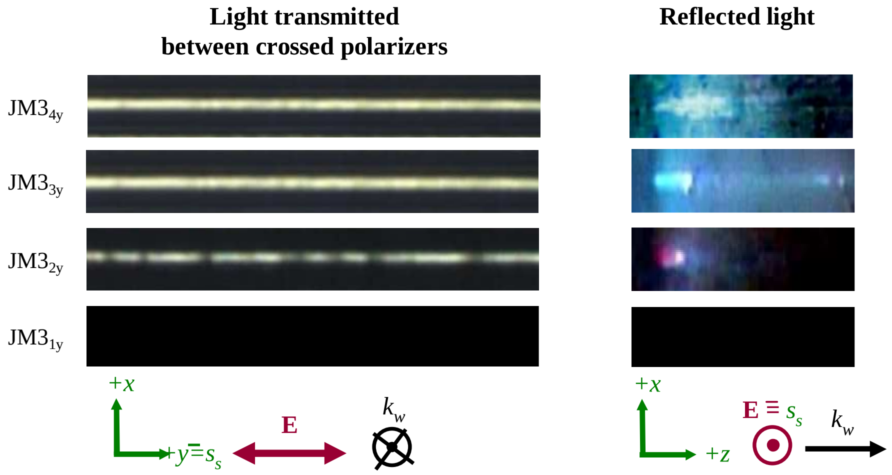

FIGURE 5.4: Microscopic images of some directly written lines. The images on the left were taken with the sample between cross polarizers and viewed via an optical microscope in transmission mode. $JM3_{2y}$, $JM3_{3y}$, $JM3_{4y}$ are birefringent, while $JM3_{1y}$ is not. In the images on the right, the same lines are illuminated and viewed from above (without cross polarizers). The birefringent structures show anisotropic reflection.

from the birefringent lines. This result strongly suggests that the observed birefringence and anisotropic reflection originate from the same mechanism and are dependent on the energy level utilized to irradiate the structures. Further results, that will be presented in Chapter 6, revealed that the line $JM3_{1x}$ also displays the anisotropic features responsible for birefringence and reflection. This future finding led us to the conclusion that the absence of anisotropic reflection and birefringence in $JM3_{1y}$, as shown here in Figure 5.4, was due to the limitation in the sensitivity of the CCD camera. Hence, the threshold of birefringence for this sample will be recognized to be $E_p < 0.24\,\mu J$.

Noting that the reflected light from all the lines exhibiting this anisotropic behaviour had a blue colour, its spectral component was studied further. The data collected with an OSA, are displayed in Figure 5.5 and show a strong peak at $460\,nm$, which indeed accounts for the blue color observed under the microscope (Fig. 5.3) and an additional smaller peak occurs at $835\,nm$.

Fluorescence could not account for this observation due to the directional dependence. We therefore suggest that the anisotropic reflectivity can only be explained as a consequence of Bragg reflection from a periodic structure. Indeed, a modulation in the refractive index with a period of $\Lambda \sim 150\,nm$, produced only along the direction of the incident laser's electric field can account for the observed anisotropic reflection at $\lambda_B = 460\,nm$ ($\lambda_B = 2n\Lambda$ [89]). Such a grating does not reflect when viewed edge on. The peak at $835\,nm$ suggests that an extra grating component may also have been formed, which has double the periodicity of the laser-induced sub-wavelength structures. Alternatively, this long wavelength reflection could be a second order diffraction peak of a grating component with period equal to the wavelength of the incident light. Surface ripples with a period equal to the wavelength of incident laser radiation, and that are

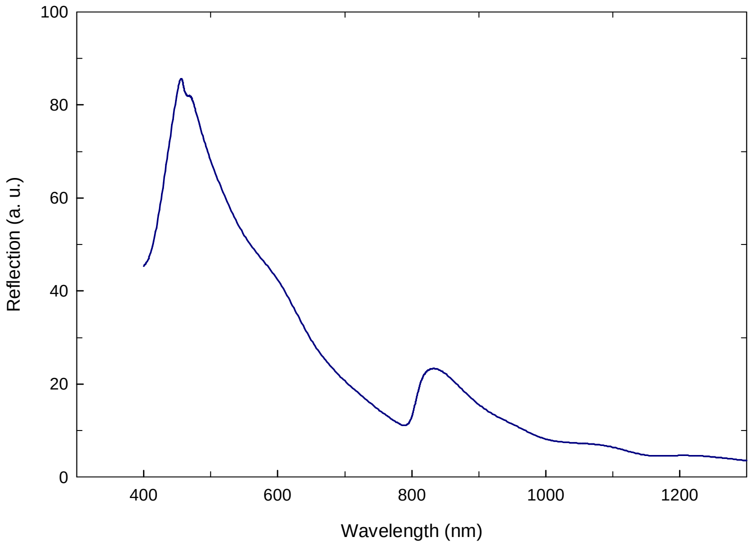

FIGURE 5.5: Spectrum of the reflected light from the structure shown in Fig. 5.3 (a), as a consequence of incident white light.

likewise aligned in a direction orthogonal to the electric field, have been observed in experiments involving laser deposition [90].

5.3 Laser-induced index change of the femtosecond direct-written structures

The results reported in the previous sections demonstrate that those femtosecond directly written lines which are birefringent, additionally display an anisotropic reflection. Previously, in Section 4.5 it was shown that the FZPs were birefringent and unexpectedly characterized by a laser-induced negative index change. However, from the data available in the literature it is well know that, with a femtosecond system like the one utilized to fabricate our structures, one can achieve structures with a *positive* index change (Chap. 1). Thus, all the evidence collected suggests that, according to the energy levels utilized to irradiate the sample, the directly written structures can either be optically isotropic and with a positive index change, or alternatively, display birefringence, anisotropic reflection and negative index change. The first structures will be denoted as “type I-fs”, and the latter as “type II-fs”.

The data reported in Table 5.1 show that the written structures, analyzed in the previous section, had a line width comparable to the optical resolution of the interferometric setup utilized for the measurement of the index change (Sec. 3.2), hence they are unsuitable for the measurement. Thus, to verify that the negative sign of the refractive index change indeed appears at the same threshold of birefringence and anisotropic reflection, a new sample was fabricated (ERB) using the same writing setup described in Section 3.1 ($\lambda_w = 835\,nm$, $r = 250\,kHz$ and $\tau \sim 200 fs$). For this experiment, the laser beam was

SAMPLE ERB

$\mathbf{E_p}$ (μ**J**)	**Square name**	$\mathbf{\Delta\phi_e}$ **(rad)**	$\mathbf{\Delta\phi_o}$ **(rad)**	$\mathbf{t_p}$ (μ**m**)
0.20 (μ**J**)	ERB$_1$	$+0.00 \pm 0.08$	$+0.00 \pm 0.05$	n.a.
0.27 (μ**J**)	ERB$_2$	$+0.63 \pm 0.08$	$+0.63 \pm 0.05$	50 ± 3
0.33 (μ**J**)	ERB$_3$	$+0.89 \pm 0.08$	$+0.74 \pm 0.05$	55 ± 3
0.53 (μ**J**)	ERB$_4$	-0.80 ± 0.08	$+0.41 \pm 0.05$	75 ± 3

TABLE 5.2: Fabrication details of the sample ERB, written with the setup described in Section 3.1, with $\lambda_w = 835\,nm$, $r = 250\,kHz$, $\tau \sim 200\,fs$, $s_s = 100\,\mu m/s$ in y. The laser was focused via the 10x objective (NA=0.21) and linearly polarized in y. This table also reports the measurement of the laser-induced phase retardation for the probing light polarized along y ($\Delta\phi_e$) or x ($\Delta\phi_o$) and the dimension of the square in the z-axis (t_p).

linearly polarized in y, and focused by a 10x (NA=0.21) objective, which allows lower levels of energy density to be obtained in the focal volume, in comparison to the 50x objective. The sample ERB consisted of an array of 4 square regions of side length of $100\,\mu m$, written in the bulk of fused silica glass (Herasil 1). To be able to find the transition between the structures of types I-fs and II-fs, we wrote each zone with different laser energy (see Table 5.2 for details). Each square was written utilizing a HP-VEE program, which controlled the translation stage and the shutter in Figure 3.1, so that the sample was moved along y for $100\,\mu m$ at a constant speed of $100\,\mu m/s$ while the shutter was open, and then translated in x for $1\,\mu m$ with the shutter closed; this process was then iterated 100 times.

The observation of the sample between cross polarizers revealed that only the structure written at the highest pulse energy shows birefringence (ERB$_4$ in Fig. 5.6). To facilitate the measurement of the refractive index change of each zone with respect to the unprocessed bulk, we used the interferometric phase-stepping technique (Sec. 3.2). The phase retardation introduced by the sample was measured twice with the probing laser polarized in y and x (ϕ_e and ϕ_o respectively). The resulting phase maps are shown in the top of Figure 5.7 (a) and Figure 5.7 (b). From these data it was possible to distinguish the phase values corresponding to the directly written zones (ϕ_{dw}) with respect to the unprocessed bulk (ϕ_{bg}). The average values of ϕ_{dw} and ϕ_{bg} were utilized to calculate the laser-induced retardation in each of the irradiated regions ($\Delta\phi = \overline{\phi_{dw}} - \overline{\phi_{bg}}$) as reported

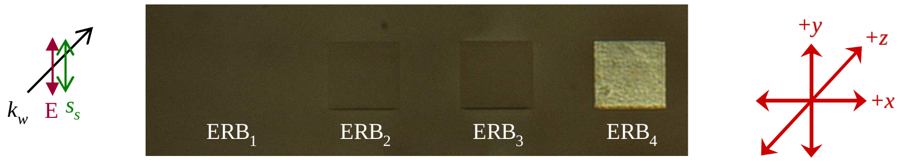

FIGURE 5.6: Microscope image of sample ERB positioned between two cross polarizers and acquired with the setup described in Section 3.3.

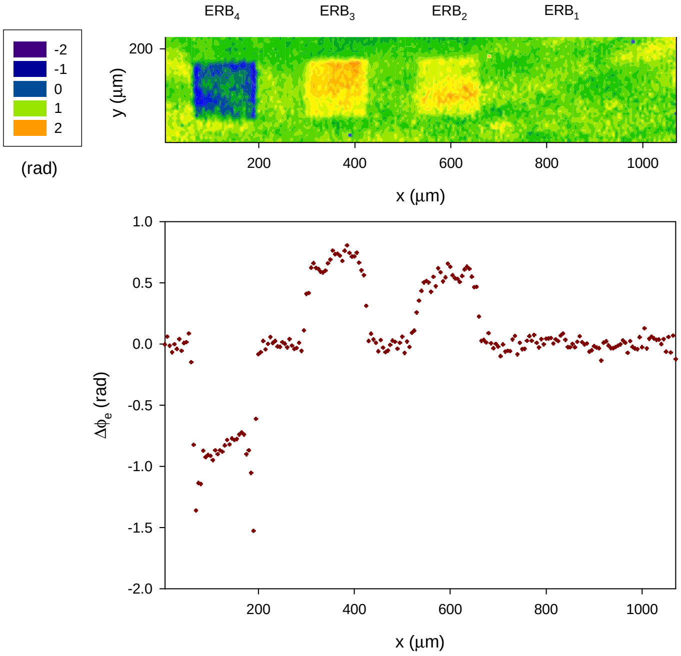

(a)

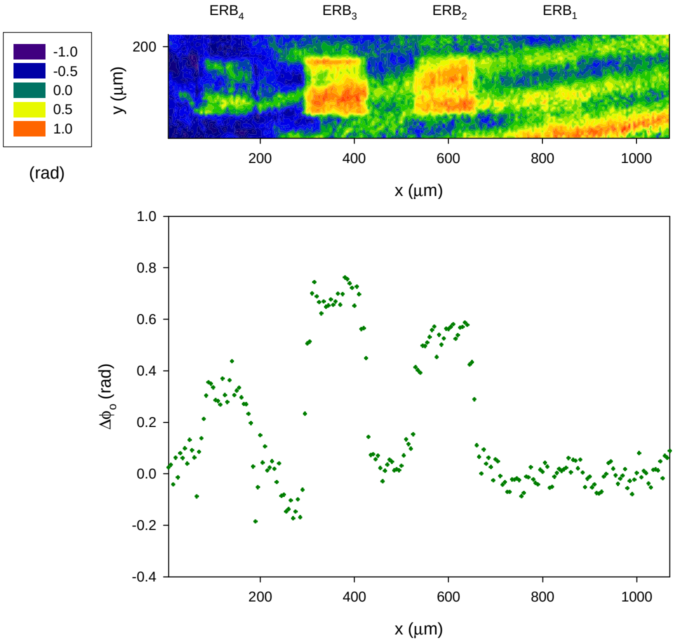

(b)

FIGURE 5.7: (a) Probe beam polarized parallel to the polarization of the writing laser. Top: Phase map ϕ_e of sample ERB (rad). Bottom: Laser-induced phase retardation plotted along x, averaged in y and corrected to a zero background. (b) Probe beam polarized perpendicular to the polarization of the writing laser. Top: Phase map ϕ_o of sample ERB (rad). Bottom: laser-induced phase retardation plotted along x, averaged in y and corrected to a zero background.

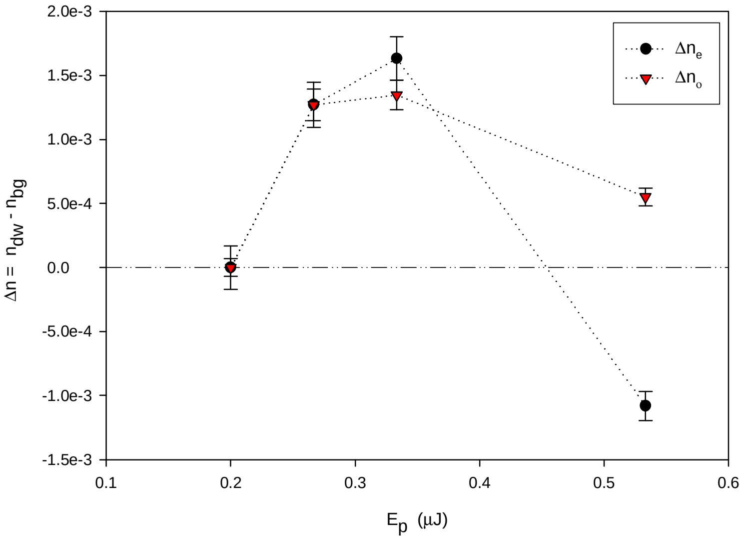

FIGURE 5.8: Laser-induced refractive index change versus pulse energy for the four structures of sample ERB (see Table 5.2 for fabrication details).

in Table 5.2. As reference, the images at the bottom of Figure 5.7 (a) and Figure 5.7 (b) show $\Delta\phi_e$ and $\Delta\phi_o$ in the x-axis averaged in y and corrected to have a zero background. Finally, the thickness of the squares in the z-axis (t_p) was measured from calibrated microscope images (Tab. 5.2) and the laser-induced index change was calculated from (3.6) (Fig. 5.8).

Indeed, the relative measure of the refractive index confirmed the previous optical observations, showing that the first three squares of ERB are optically isotropic. The difference between the ordinary and extraordinary indices is in fact within the error bars of the measurement for the first three points of Figure 5.8, whereas in the last structure (ERB_4) an evident anisotropy is observed. As previously predicted, an abrupt change in the sign of the laser-induced index change arises at the same threshold of birefringence. Following the experimental data depicted in Figure 5.8 it may be observed that no index change Δn is observed in the first structure (ERB_1), then Δn grows monotonically with pulse energy until a maximum positive value of $(+1.5 \pm 0.1) \times 10^{-3}$ for ERB_3. Finally, in ERB_4 the extraordinary index change becomes strongly negative reaching the minimum value of $(-1.1 \pm 0.1) \times 10^{-3}$. On the contrary, the ordinary index change is still positive i.e., the laser-induced index change in this birefringent structure, is positive for the ordinary wave and negative for the extraordinary. This is indeed a new observation, as the value of the laser-induced phase retardation measured for the birefringent FZPs in Section 4.5 was negative for both ordinary and extraordinary waves.

Finally, when the sample was checked under a microscope in reflection mode, it was confirmed that only ERB_4 displays anisotropic reflection.

5.4 Self-assembled sub-wavelength periodic structures

The results presented in the previous section confirmed that those characteristics that distinguish femtosecond directly written structures of type II-fs, namely birefringence, anisotropic reflection, and a negative change in the extraordinary refractive index, onset at the same energy threshold, and are therefore likely to originate from the same phenomenon.

When we first discussed the anisotropic reflection in Section 5.2, we speculated that the appearance of blue reflection, only in the direction of the polarization of the writing laser, could be explained assuming that a sub-wavelength period grating is formed within the irradiated focal volume, with its ruling parallel to the direction of the polarization of the writing laser (Fig. 5.9). At that time, this explanation was proposed as the only plausible justification of our experimental observation, and it was furthermore strengthened by the consideration that the orientation of the alleged nanostructure is identical to that implicated in a previous publication from our group describing the empirical observation of anisotropic light scattering [44].

Observing Figure 5.9, which shows a schematic of how the nano-grating may be arranged, it is immediately evident that such a type of periodic structure, whose period is smaller than the wavelength of light, has a known type of anisotropy defined as *form birefringence* (Sec. B.3). Our experimental evidence showed that the directions of polarization in the anisotropic structures are always parallel and perpendicular to the polarization of the writing field when the light is propagating in the z-axis. This is consistent with the scenario of Figure 5.9, where the direction parallel to the ruling of the periodic assembly is the optic axis (see Section B.3 for details). The experimental measurement of n_e and n_o (Sec. 4.5, and Sec. 5.3) revealed that the birefringent structures behave as a

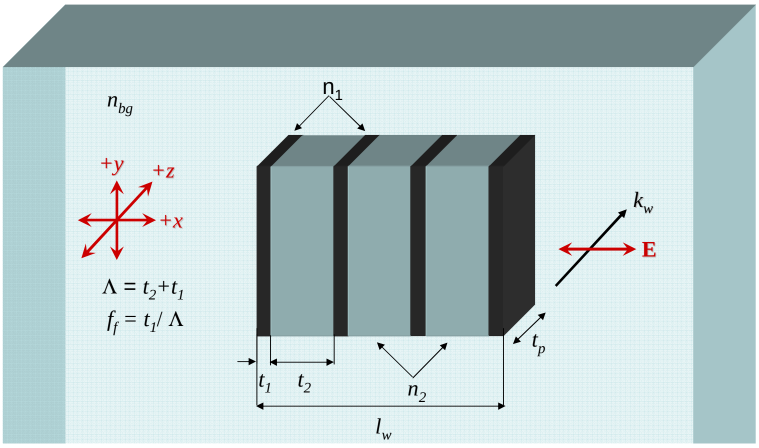

FIGURE 5.9: Schematic of the arrangement of the periodic assembly within the irradiated volume. k_w: laser wave vector. **E**: Polarization direction of the writing laser. n_1 and n_2: local refractive indices of the plates of thickness t_1 and t_2, respectively. n_{bg}: refractive index of the surrounding material.

negative uniaxial material, where the speed of the extraordinary wave is always greater than the speed of the ordinary one ($n_e < n_o$). This result is in agreement with what is expected from (B.24), furthermore reinforcing the hypotheses that anisotropic reflection and birefringence appears as the result of the formation of a sub-micron assembly of plates.

In conclusion proposing that a periodic modulation of the refractive index formed as a result of the femtosecond pulse laser irradiation of the material, besides being the only plausible explanation for the anisotropic reflection, can indeed explain the birefringent behaviour observed in the anisotropic structures. We now show that this theory can furthermore justify the unexplained evidence reported in Section 5.3, where it was demonstrated that, in ERB$_4$, the extraordinary index change is negative, while the ordinary is positive.

Starting from (B.23), the experimental values of the phase retardation induced by the laser in the birefringent structures ($\Delta\phi_e$ and $\Delta\phi_o$), measured with the interferometric technique (Sec. 3.2) can be expressed as a function of the local indices of refraction of the periodic assembly (n_1 and n_2 in Fig. 5.9) and of the filling factor $f_f = t_1/\Lambda$:

$$\Delta\phi_e = \frac{2\pi}{\lambda} t_p \left[\sqrt{\frac{n_1^2 n_2^2}{f_f n_2^2 + (1-f_f) n_1^2}} - n_{bg} \right], \tag{5.3a}$$

$$\Delta\phi_o = \frac{2\pi}{\lambda} t_p \left[\sqrt{f_f n_1^2 + (1-f_f) n_2^2} - n_{bg} \right], \tag{5.3b}$$

where, t_p is the dimension of the written structures in the z-axis (thickness), λ is the wavelength of the probing light in the interferometer and n_{bg} is the refractive index of the unprocessed material. A change of variables leads to

$$\Delta\phi_e = \frac{2\pi}{\lambda} t_p \left[\sqrt{\frac{(\Delta n_2 - \Delta n_{21} + n_{bg})^2 (\Delta n_2 + n_{bg})^2}{f_f (\Delta n_2 + n_{bg})^2 + (1-f_f)(\Delta n_2 - \Delta n_{21} + n_{bg})^2}} - n_{bg} \right], \tag{5.4a}$$

$$\Delta\phi_e = \frac{2\pi}{\lambda} t_p \left[\sqrt{f_f (\Delta n_2 - \Delta n_{21} + n_{bg})^2 + (1-f_f)(\Delta n_2 + n_{bg})^2} - n_{bg} \right], \tag{5.4b}$$

where $\Delta n_2 = n_2 - n_{bg}$ is the difference between the local index n_2 and the unprocessed material, and $\Delta n_{21} = n_2 - n_1$ where $\Delta n_{21} > 0$ is the difference between the two local indices, and hence a measure of the strength of the nano-grating.

Figure 5.10 shows contour plots of $\Delta\phi_e$ (dashed curve), $\Delta\phi_o$ (dashed-dotted curve), versus Δn_{21} and Δn_2 for $t_p = 70\,\mu m$, $\lambda = 632.8\,nm$ and $n_{bg} = 1.453$. The area between the black lines contains all the solutions for which $\Delta\phi_e\Delta\phi_o < 0$, i.e. the solutions for which the ordinary and the extraordinary index change has opposite sign. The experimental solutions (ERB$_4$ of Sec. 5.3, FZPs of Sec. 4.5) are highlighted by circles in the figure, sized to include the experimental error. We found that the experimental results match the theory for the values of $\Delta n_{21} = +0.077$ and $\Delta n_2 = +0.023$. These

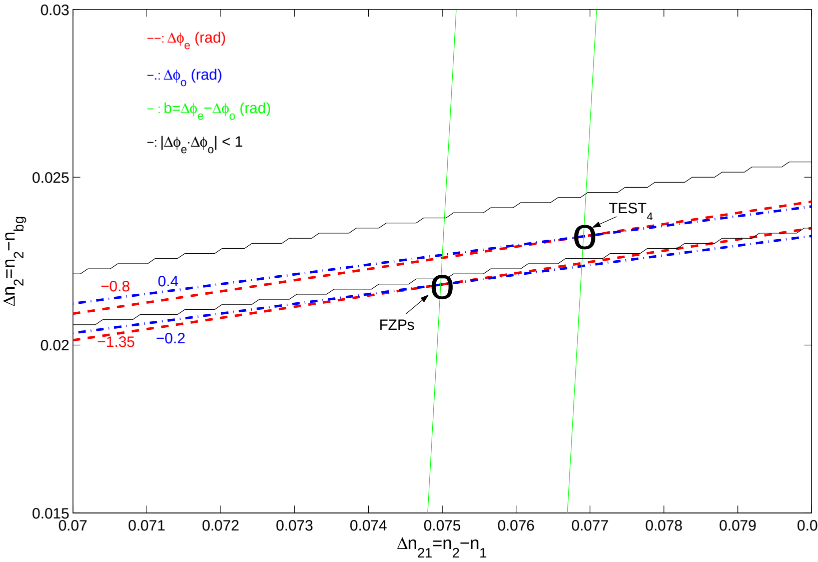

FIGURE 5.10: Contour plots of $\Delta\phi_e$ (red dashed curve), $\Delta\phi_o$ (blue dashed-dotted curve), $b = \Delta\phi_e - \Delta\phi_o = (2\pi t_p \beta/\lambda)$ (green line), and $\Delta\phi_e\Delta\phi_o < 0$ (black line) versus Δn_{21} and Δn_2 for $t_p = 70\,\mu m$, $\lambda = 632.8\,nm$, $f_f = 0.3$, and $n_{bg} = 1.453$.

	$\mathbf{\Delta n_{21} \times 10^{-1}}$	$\mathbf{\Delta n_{2} \times 10^{-2}}$	$\mathbf{\Delta n_{1} \times 10^{-1}}$
$\mathbf{f_f = 0.1}$	+1.15	+1.2	-1.03
$\mathbf{f_f = 0.3}$	+0.77	+2.3	-0.54
$\mathbf{f_f = 0.5}$	+0.71	+3.6	-0.36

TABLE 5.3: Values of the local indices of refraction (relative to the silica background) of the periodic sub-wavelength structures responsible for the onset of birefringence and anisotropic reflection in ERB$_4$. The data were calculated from (5.4) utilizing the experimental measurement of $\Delta\phi_e$ and $\Delta\phi_e$ and t_p reported in Table 5.2.

results show that locally, the laser induces a very strong grating consisting of a periodic series of plates in which the material is denser than the substrate, that alternates with other zones in which the material is more rarefied.

The plot was calculated for a filling form $f_f = 0.3$ because further experimental evidence, that will be discussed in Chapter 6, will show that this value corresponds to that measured in our structures. However, in Table 5.3 the values of Δn_{21}, Δn_2, and Δn_1 are calculated also for $f_f = 0.5$, which describes a uniform grating ($t_1 = t_2$ in Fig. 5.9), and for a filling form of $f_f = 0.1$ corresponding to other reported cases in the literature ([91] Chap. 6).

Figure 5.11 shows the contour plot of $b = \Delta\phi_e - \Delta\phi_o = (2\pi t_p(n_e - n_o)/\lambda)$ (calculated with the same parameters as before and for $f_f = 0.3$). The curves corresponding to various values of b are almost vertical, suggesting that the birefringence $\beta = n_e - n_o$ depends mainly on the strength of the self-assembled grating.

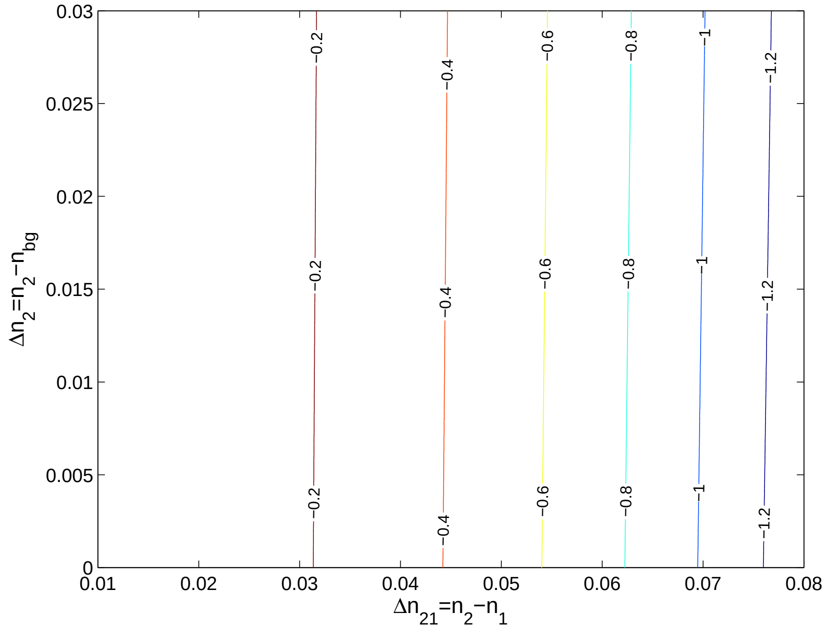

FIGURE 5.11: contour plot of $b = \Delta\phi_e - \Delta\phi_o = (2\pi t_p \beta/\lambda)$ versus Δn_{21} and Δn_2 for $t_p = 70\,\mu m$, $\lambda = 632.8\,nm$, $f_f = 0.3$, and $n_{bg} = 1.453$.

5.5 Transition between the directly written structures of type I-fs and type II-fs

In Section 5.3 we found that in the sample ERB, the transition between the directly written structures of type I-fs and type II-fs occurs at an energy level $0.33\,\mu J < E_b < 0.53\,\mu J$. In [46], birefringence onset was said to occur at the critical power for self-focusing, P_c, given by Equation 2.13. Table 5.4 reports the values of the birefringence threshold found for our samples, compared to the critical energy of self-focusing calculated from (2.13) for our experimental conditions, using $E_c = P_c\tau/0.9$ with $\tau = 200\,fs$ [31]. While for the sample ERB, the two values are indeed comparable, in the case of JM3, the birefringence onsets at an energy level lower than half of the energy value corresponding to the critical power of self-focusing. Considering that JM3 was written in tighter focusing conditions, hence with higher energy density, this discrepancy can only be explained if the transition between directly written structures of type I-fs and II-fs has an intensity (rather than a power) threshold. In order to verify this hypothesis, a new sample (TH) was written in silica with the setup described in Section 3.1 ($\lambda_w = 800\,nm$, $r = 100\,kHz$,

Sample	λ_w **(nm)**	$\mathbf{n_{bg}}$	$\mathbf{n_{2bg}} \times \mathbf{10^{-16}}$ $(\frac{\mathbf{cm^2}}{\mathbf{W}})$ [92]	$\mathbf{E_b}$ $(\mu\mathbf{J})$	$\mathbf{E_c}$ $(\mu\mathbf{J})$
JM3	850	1.452	3.753	$E_b < 0.24$	0.44
ERB	835	1.453	3.751	$0.33 < E_b < 0.53$	0.43

TABLE 5.4: Values of the birefringence threshold found for the samples JM3 (Sec. 5.1), and ERB (Sec. 5.3) compared to the critical energy levels for self-focusing.

SAMPLE TH			
10x		**50x**	
E_p (μ**J**)	**TH10**	E_p (μ**J**)	**TH50**
0.08	$TH10_1$	0.10	$TH50_1$
0.40	$TH10_2$	0.50	$TH50_2$
0.80	$TH10_3$	1.00	$TH50_3$
1.20	$TH10_4$	1.50	$TH50_4$
1.60	$TH10_5$	2.00	$TH50_5$
2.14	$TH10_6$	2.67	$TH50_6$

TABLE 5.5: Fabrication details of the sample TH, written with the setup described in Section 3.1, with $\lambda_w = 800\,nm$, $r = 100\,kHz$, $\tau \sim 200\,fs$, $s_s = 80\,\mu m$ in y. The laser was linearly polarized in y.

and $\tau \sim 200 fs$). It consisted of 12 squares directly written in silica (Herasil 1), 150 μm underneath the glass surface at a constant speed of 80 $\mu m/s$. Half of the squares were written with the laser focused by the 50x objective (TH50 in Table 5.5), the others utilizing the 10x objective (TH10 in Table 5.5). The laser was linearly polarized along y.

After fabrication, the sample TH was positioned between crossed polarizers and viewed under an optical microscope in transmission mode to verify the presence of laser-induced birefringence (Sec. 3.3). Figure 5.12 shows that, while all the structures written with the light focused with the 50x objective transmit light, only 2 of the squares written with the 10x objective ($TH10_5$ and $TH10_6$) are birefringent. It may also be appreciated that some light is transmitted in the region surrounding the non birefringent structures $TH10_4$ (but not through the actual laser written region). This phenomenon can be attributed to stress birefringence induced in the surrounding material of the densified regions [32, 93]. After measuring the thickness t_p of each directly written structure using calibrated images (Fig. 5.13), and the laser-induced extraordinary ($\Delta\phi_e$) and ordinary phase retardation ($\Delta\phi_o$), utilizing the interferometric setup described in Section 3.2, the

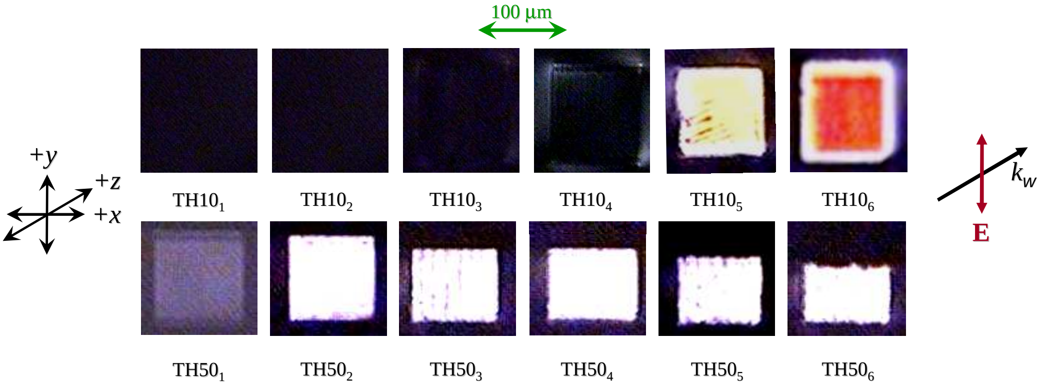

FIGURE 5.12: Microscope images of all the squares of the sample TH between cross polarizers.

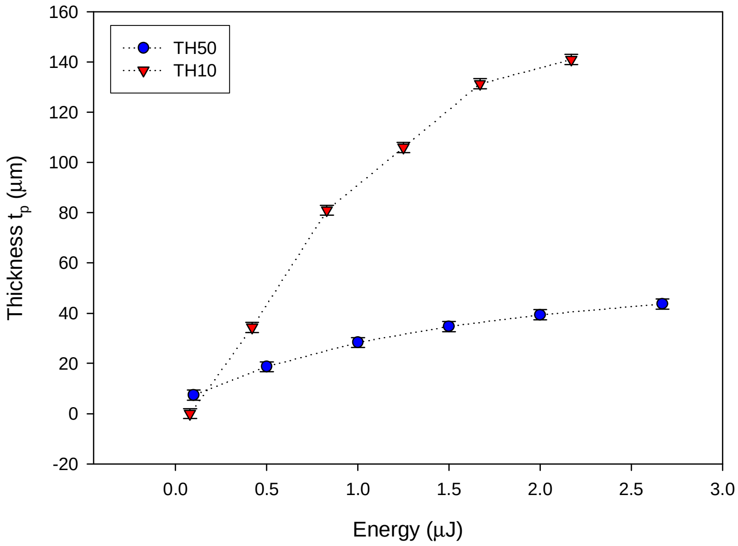

FIGURE 5.13: Experimental measurement of the thickness t_p of the squares of the sample TH, plotted versus the pulse energy.

modification of the refractive index in the irradiated region was calculated from (3.6) (Fig. 5.14). Indeed, the experimental results confirmed the previous optical observation showing that all the structures written with the 50x objective were birefringent (Fig. 5.14 (b)), while, amongst all the squares irradiated with the 10x objective, only TH10$_5$ and TH106 exhibited dissimilar refractive indices $n_e \neq n_o$ (Fig. 5.14 (a)). The critical power for self-focusing, was in this case equal to $1.78\,MW$, corresponding to $E_c = 0.39\,\mu J$. At this energy level, the squares written under tight focusing conditions are already birefringent, whilst the squares written with the 10x objective remain optically isotropic. This proves that the onset of the anisotropy of the directly written structures and the self-focusing are not correlated.

A further interesting feature that the reader might have noticed is that, the light transmitted by the birefringent zones, positioned between cross polarizers, is white for TH50, and of a specific color for TH10$_5$, and TH10$_6$ (Fig. 5.12). This observation can be easily explained considering that a birefringent plate of thickness t_p positioned between cross-polarizers, is a filter for the wavelength satisfying

$$\lambda_c =\mid n_e - n_o \mid t_p. \tag{5.5}$$

For λ_c, ordinary and extraordinary waves traversing the plate experience a phase shift of 2π and therefore add up in phase after the propagation through the birefringent material thus preserving the initial linear polarization. After the second polarizer (positioned at 90° with respect to the first one), the light propagating with a wavelength satisfying (5.5) is therefore suppressed (Sec. B.2). If λ_c is in the visible spectrum, the light exiting the second polarizer will lack this component and it will therefore appear as its complementary color. The images recorded demonstrate that λ_c falls in the visible spectrum

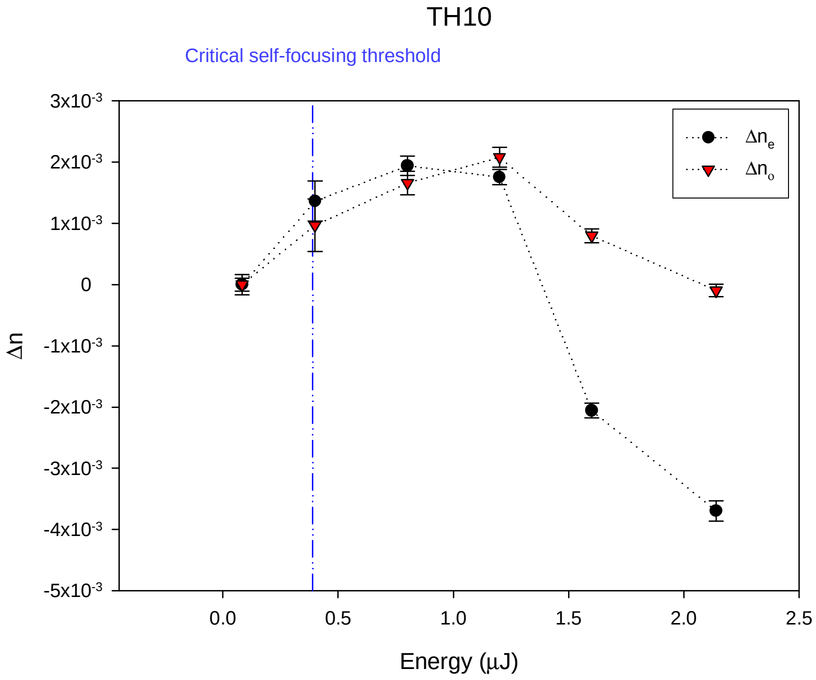

(a)

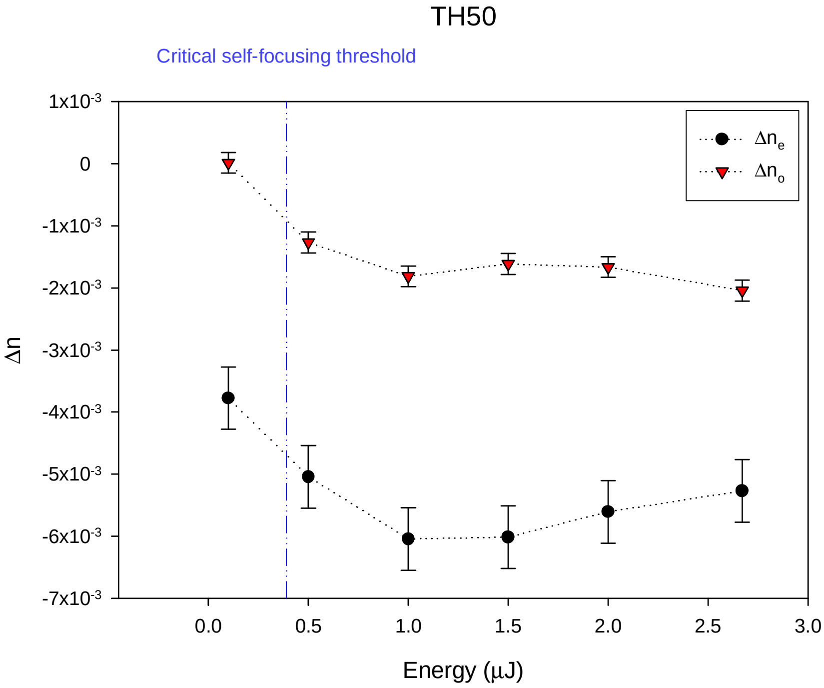

(b)

FIGURE 5.14: Laser-induced modification of the refractive index of the sample TH. (a): TH10, (b): TH50.

for TH10_5, TH10_6.

5.5.1 Dependance of the induced index change on the laser intensity

Figure 5.15 shows the behaviour of the index change of the sample TH plotted on a single graph versus the laser intensity ($I = 1.8E_p/(\tau\pi\omega_0^2)$, with ω_0 beam waist at the focal point [31]). At the lowest level of intensity utilized to irradiate the sample, no index change is detected. Following the data on the plot from left to right Δn is initially positive, growing monotonically until a saturation level of $(+2.1 \pm 0.2) \times 10^{-3}$ is reached. From TH10_5 the laser written zone becomes strongly birefringent, with $n_e < n_o$. The index change of the extraordinary wave is always negative and saturates at a level of $(-5.7 \pm 0.5) \times 10^{-3}$, which, in absolute value, is the largest refractive index modification induced in this silica sample. The ordinary index change is initially positive with respect to the silica background, but finally becomes negative reaching a saturation level of $(-1.8 \pm 0.2) \times 10^{-3}$.

It is important to underline that the graph reported in Figure 5.15 has to be regarded with a certain caution. The values of the beam size utilized to calculate the intensity have been calculated from (5.2) for NA=0.5 ($\omega_0^{50\text{x}} = 0.44\,\mu m$), and NA=0.10 ($\omega_0^{10\text{x}} = 2.5\,\mu m$). However, as was discussed in Section 2.5, the calculation of ω_0 requires the solution of the wave equation in a non-paraxial approximation and taking into account the non-linear effects produced by the propagation of a focused beam of ultrashort pulses in the

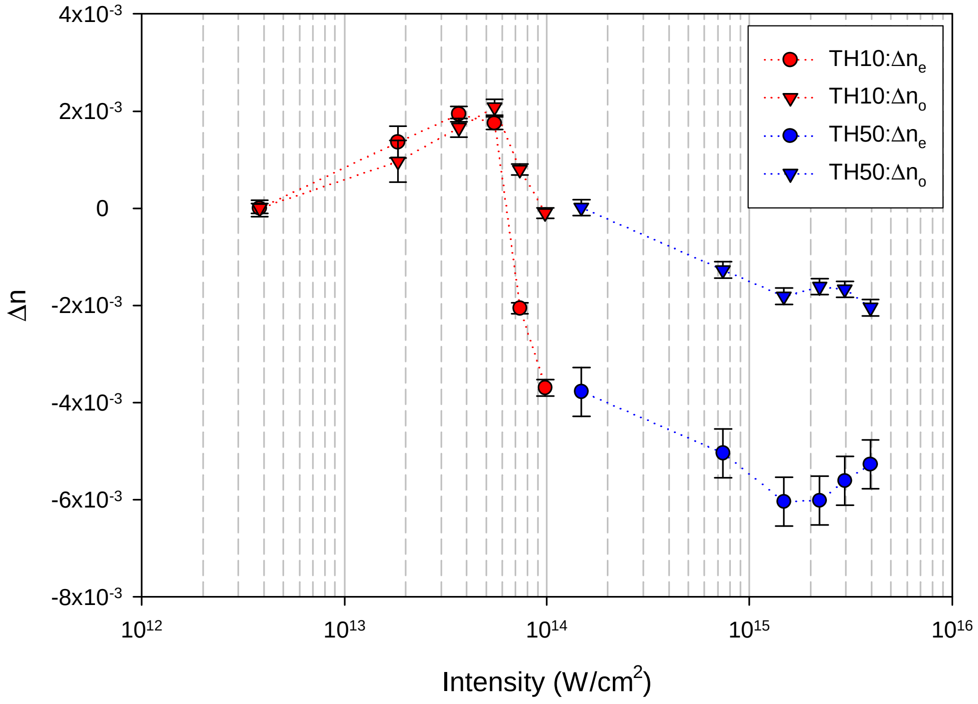

FIGURE 5.15: Laser-induced index change of the sample TH versus the laser intensity.

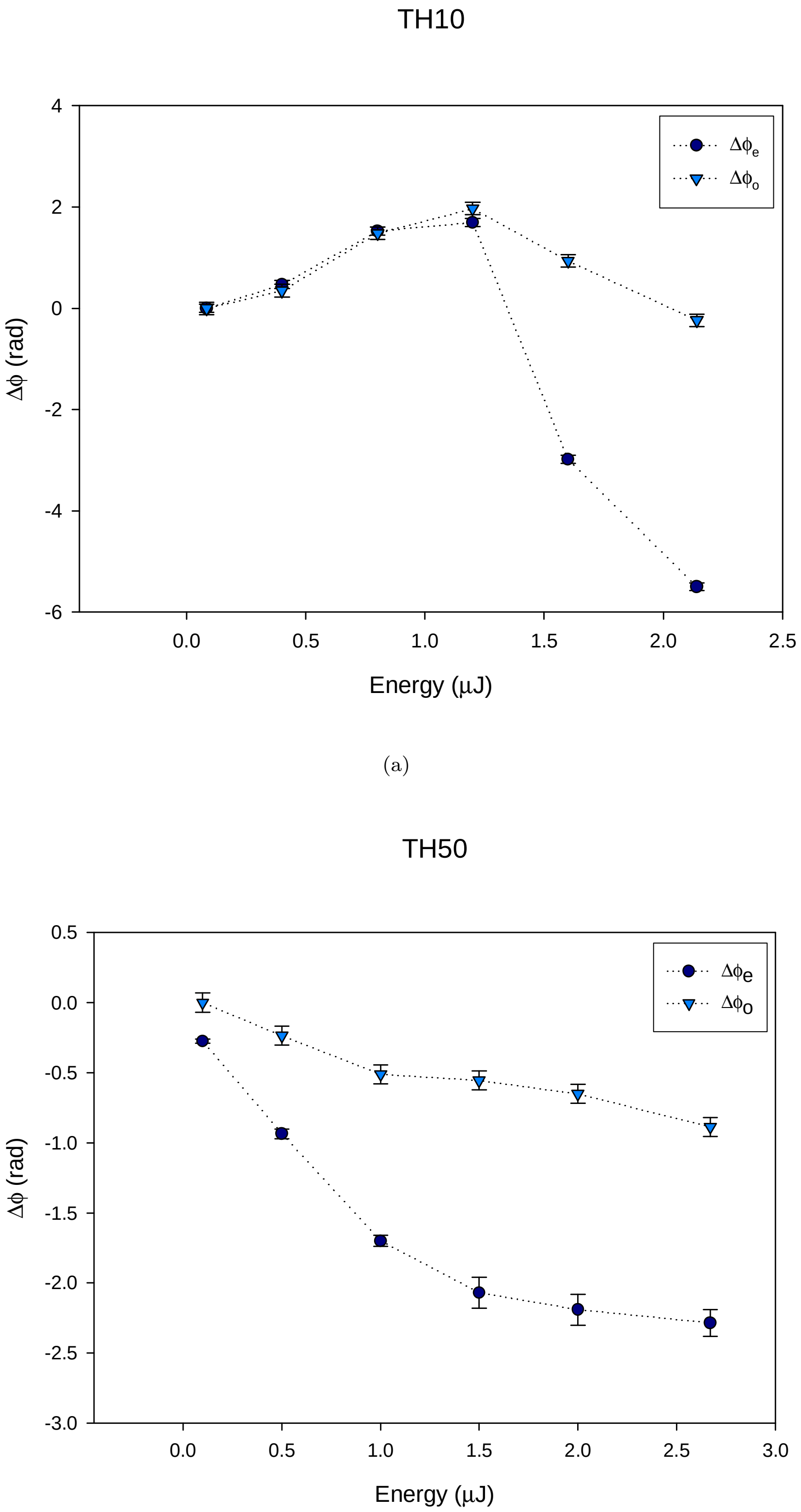

(a)

(b)

FIGURE 5.16: Phase retardation induced by the laser in the silica sample TH. (a): TH10, (b): TH50.

SAMPLE THS			
E_p (μJ)	**TH10S2**	**TH10S3**	**TH10**
0.08	TH10S2$_1$	TH10S3$_1$	TH10$_1$
0.40	TH10S2$_2$	TH10S3$_2$	TH10$_2$
0.80	TH10S2$_3$	TH10S3$_3$	TH10$_3$
1.20	TH10S2$_4$	TH10S3$_4$	TH10$_4$
1.60	TH10S2$_5$	TH10S3$_5$	TH10$_5$
2.14	TH10S2$_6$	TH10S3$_6$	TH10$_6$

TABLE 5.6: Fabrication details of the sample THS, written with the setup described in Section 3.1, with $\lambda_w = 800\,nm$, $r = 100\,kHz$, $\tau \sim 200\,fs$. The laser was focused with the 10x objective and linearly polarized in y. TH10S2: $s_s = 40\,\mu m/s$, TH10S3: $s_s = 60\,\mu m/s$, TH10: $s_s = 80\,\mu m/s$.

material. To our knowledge, this complete theoretical model is not yet available in the literature, and its solution was beyond the scope of this thesis.

Finally, it may be worth noting that, although the index change achieved in a stronger focusing condition is higher, the thickness of the modified region is shorter (Fig. 5.13). Therefore, the highest phase retardation of almost 2π is induced in the structure TH10$_6$ (written with the 10x objective) (Fig. 5.16).

5.5.2 Anisotropic threshold versus the translation speed

In order to verify if the transition between the directly written structures of type I-fs and type II-fs is affected by the writing speed, the squares of TH, created with the

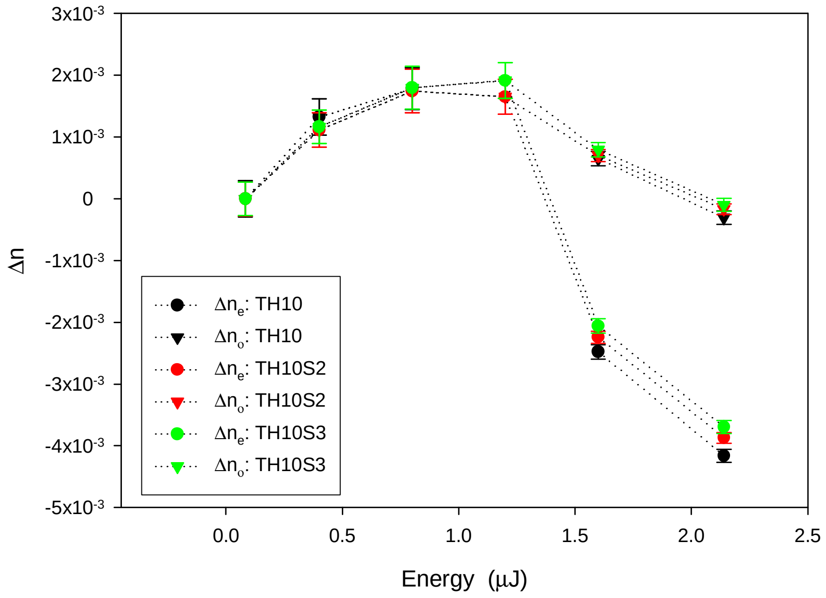

FIGURE 5.17: Laser-induced index change in THS versus the laser energy.

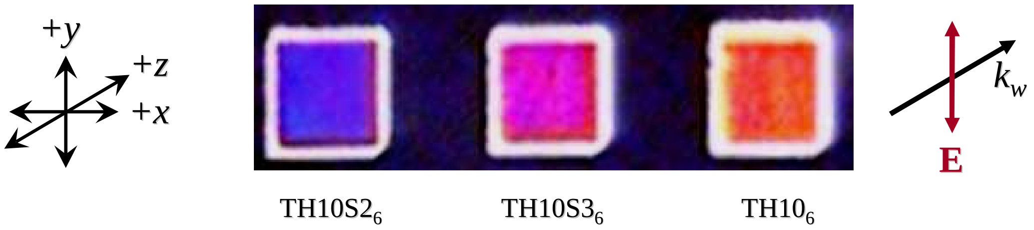

FIGURE 5.18: Microscope image of TH10S2$_6$, TH10S3$_6$, and TH10$_6$ between cross polarizers.

laser focused via the 10x objective (TH10 of Table 5.5), were replicated in the same experimental conditions except for translation speed of the stage. A series of written squares (TH10S2) was fabricated with the sample translated at $40\,\mu m/s$, the other (TH10S3) with $s_s = 60\,\mu m/s$ (See Table 5.6 for details).

The measure of the modification of the index change in all the structures reveals, that the birefringence threshold is $1.2\,\mu J < E_b < 1.6\,\mu J$, regardless of the translation speed (Fig. 5.17). In addition it can be appreciated that the variation of the index change versus the speed is of the same order as the experimental error for the non birefringent structures, while in the birefringent squares $|\Delta n|$ decreases with the speed, both for ordinary and extraordinary index, leading to reduction of the birefringence. This can be visually appreciated in Figure 5.18, where the colour transmitted by squares written at the same energy (and with the same t_p) shifts towards longer wavelength with an increasing writing speed. Since the transmitted colour is the complementary of (5.5), Figure 5.18 demonstrates that the laser-induced birefringence decreases with the speed.

5.6 Repeatability of the results

To verify the repeatability of the results, two different samples (R1 and R2) were irradiated with the same experimental conditions, but on two different days. For both samples the parameters of the laser were: $\lambda_w = 800\,nm$, $r = 100\,kHz$, $\tau \sim 200\,fs$. The beam was focused with the 10x objective and linearly polarized in y. Finally, the translation speed was set to $s_s = 40\,\mu m/s$

The results concerning the measure of the phase retardation induced in each sample, shown in Figure 5.19 are qualitatively in good agreement, however the phase shift measured for R2 is slightly lower than in R1. This discrepancy could be ascribed to the variation of the laser pulse duration which, as mentioned in Chapter 3, could not be monitored daily.

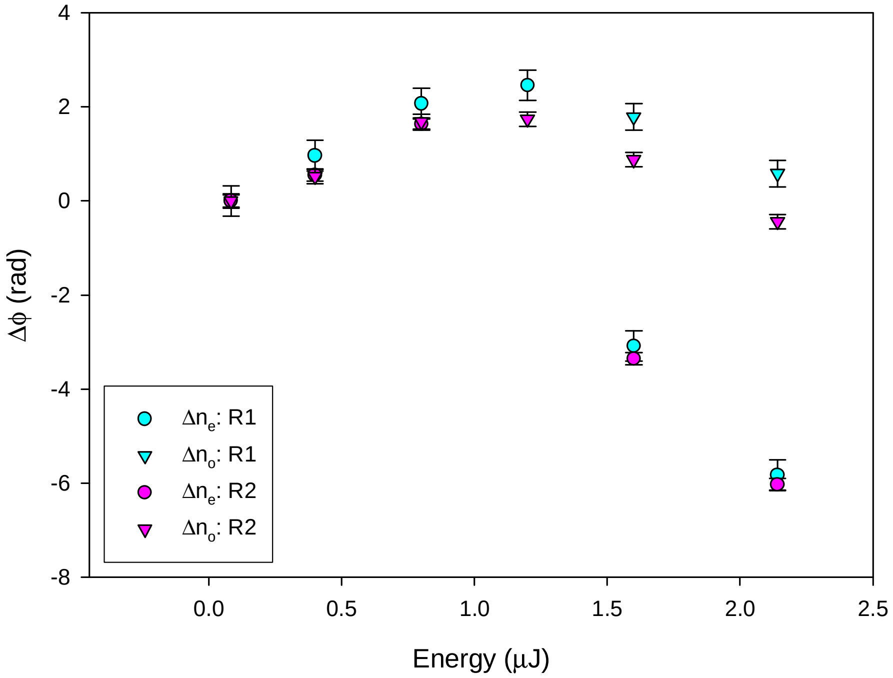

FIGURE 5.19: Laser-induced phase retardation of the samples R1 and R2.

5.7 Annealing

The results reported in [36, 94] have proven that the femtosecond direct written structures of type I-fs have a higher stability at increased temperatures with respect to direct-write UV laser-induced index changes. As discussed in the previous sections, type II-fs femtosecond modified regions written in silica over a certain intensity threshold, become birefringent and display a negative average index change with respect to the surrounding material. In order to investigate the stability of these anisotropic structures (type II-fs), in comparison with the non birefringent ones, an annealing experiment was performed.

The 6 squares of sample TH10S3 (Table 5.6) were heated at rate of $3\,^{\circ}C$ per minute, kept at $200\,^{\circ}C$ for one hour and then cooled to room temperature at $1\,^{\circ}C$ per minute. This treatment was then repeated up to maximum temperatures of $500\,^{\circ}C$, $800\,^{\circ}C$, $1100\,^{\circ}C$ and $1400\,^{\circ}C$, and after each annealing step the index change was measured, except for the last case $T_{\max} = 1400\,^{\circ}C$, where the sample crystallized during the operation. The interferometric setup (Sec. 3.2) was again utilized to measure the index change, thus it was not possible to perform the measurement while the temperature increase was applied to the sample. Therefore, the reported results refer to the steady state value assumed by the modified structures after being heated and cooled to room temperature (Fig. 5.21).

The index change of all the structures was unaltered up to a temperature of $500\,^{\circ}C$, but after annealing above this temperature structures belonging to type I-fs ($\mathrm{TH10S3}_1$,

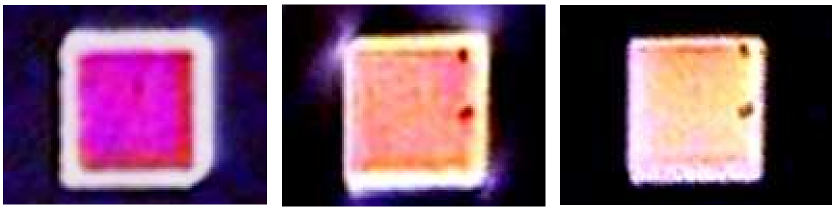

Figure 5.20: Microscope images of TH10S3_6 between cross polarizers before any annealing step and after being heated at $800\,°C$, and $1100\,°C$.

TH10S3_2, TH10S3_3, TH10S3_4) behaved very differently to those of type II-fs (TH10S3_5, TH10S3_6). In agreement with previously reported results [36] the index change of the isotropic non birefringent structures decreased by a factor of ~ 0.4 with respect to the initial value after heating at $800\,°C$, and finally disappeared after annealing at $1100\,°C$. On the contrary the birefringent regions were still clearly visible under an optical microscope even after annealing at $1100\,°C$ (Fig. 5.20).

Rather unexpectedly, however, it was found that both the ordinary and extraordinary index change in the birefringent structures become more negative with respect to silica (Fig. 5.21). This behavior can be better appreciated in Figure 5.22 (a) where the normalized extraordinary index change, measured after each annealing step, is plotted versus the maximum exposure temperature. It should be noted that, while for the structures of type I-fs, the index change decreases after $500\,°C$, for the two structures of type II-fs, an increase is measured. Our observations lead to the surprising conclusion that, in the anisotropic structures of type II-fs, the absolute value of the modification of the refractive index induced by the laser, *increases* with the temperature. Yet, as can be visually appreciated in Figure 5.20, the birefringence of the structures $\beta = |n_e - n_o|$ decreases with the temperature. This observation is confirmed in Figure 5.22 (b), where the birefringence was calculated and plotted as a function of the temperature. As mentioned in Section 5.4, the birefringence of the structures is a measure of the strength of the nano-grating formed in the irradiated volume. Using the experimental values of, $\Delta\phi_e$, $\Delta\phi_o$ and t_p, $\Delta n_1 = n_1 - n_{bg}$, $\Delta n_2 = n_2 - n_{bg}$ and $\Delta n_{21} = n_2 - n_1$ where calculated from (5.3) with $f_f = 0.3$ (Fig. 5.23 (a), 5.23 (b), 5.24 (a), respectively). Indeed, as might be expected, both Δn_1 and Δn_2 decrease in their absolute values, with increasing annealing temperature, hence the grating becomes weaker and, consequently, the birefringence reduces. However, since n_2 anneals more rapidly than n_1 (Fig. 5.24 (b)), their relative weight in (5.3) is such that the absolute values of the ordinary and extraordinary index change increase.

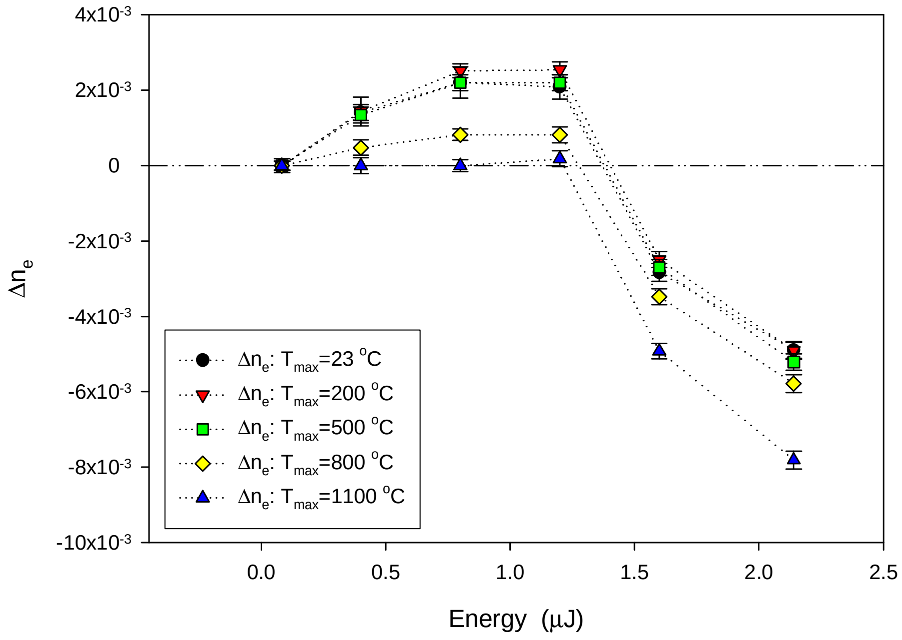

(a)

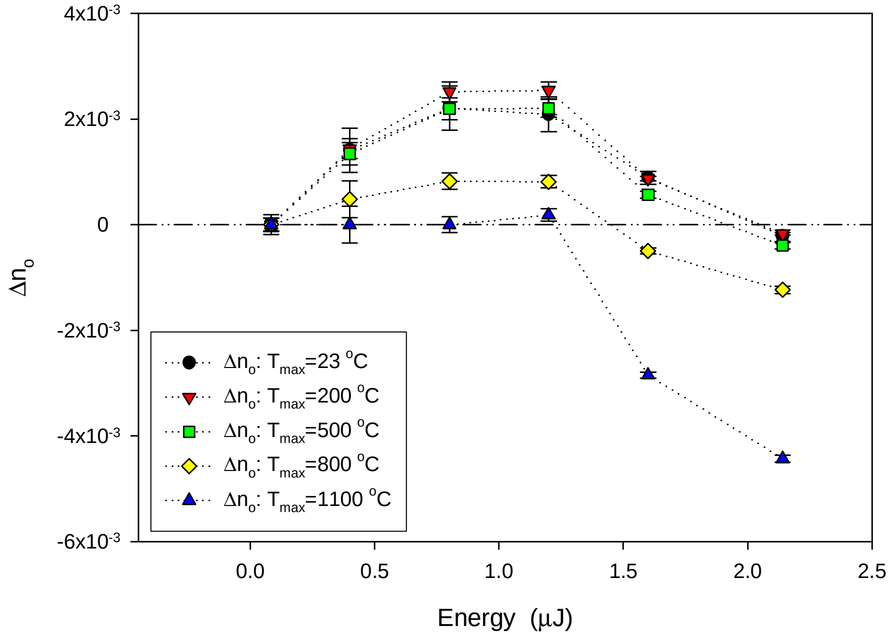

(b)

FIGURE 5.21: Measure of the laser-induced index change of the sample TH10S3 versus the energy after each annealing step. (a): Δn_e. (b): Δn_o.

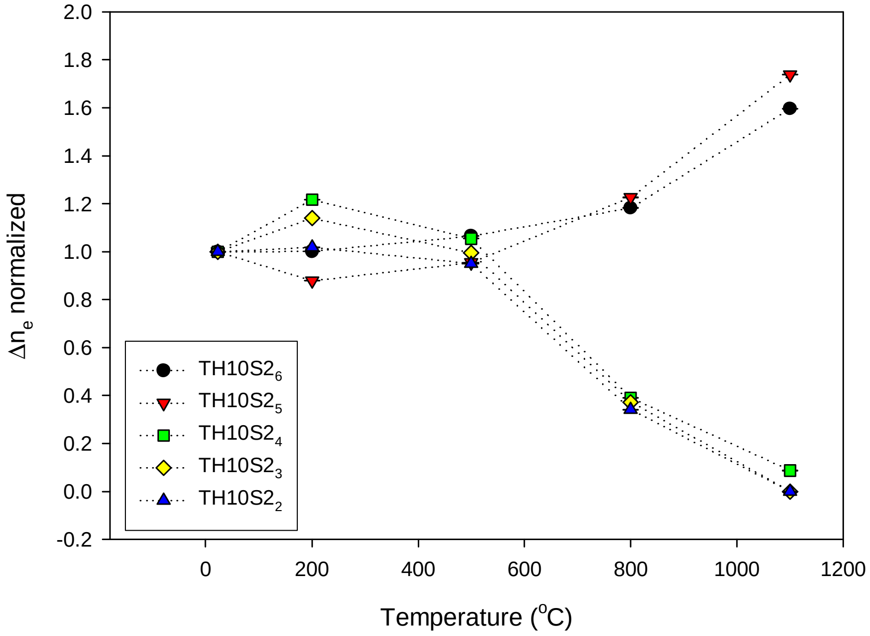

(a)

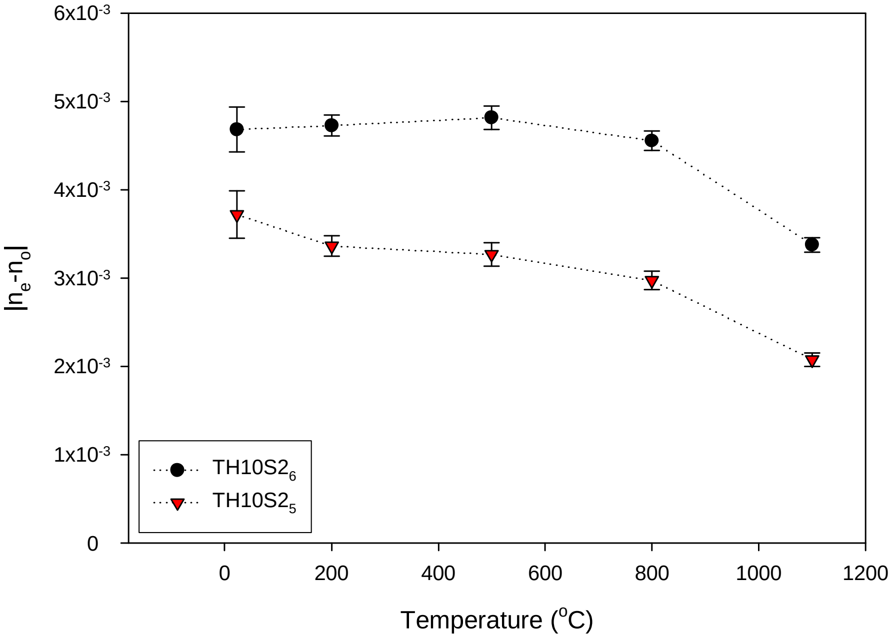

(b)

FIGURE 5.22: (a): Extraordinary index change of the sample TH10S3 normalized to the value measured before any annealing step versus the temperature. (b): Birefringence of the sample TH10S3 versus the temperature.

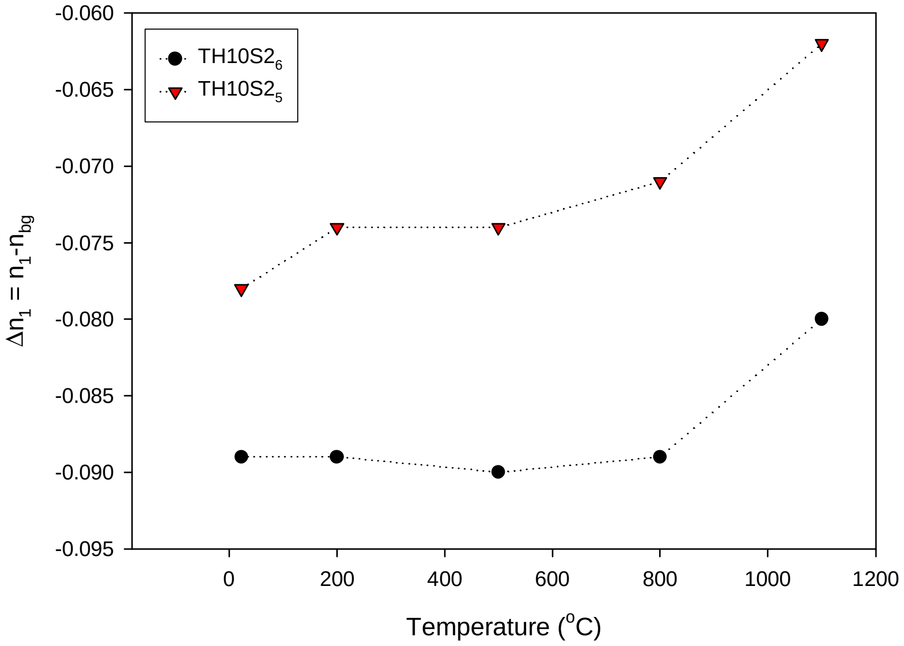

(a)

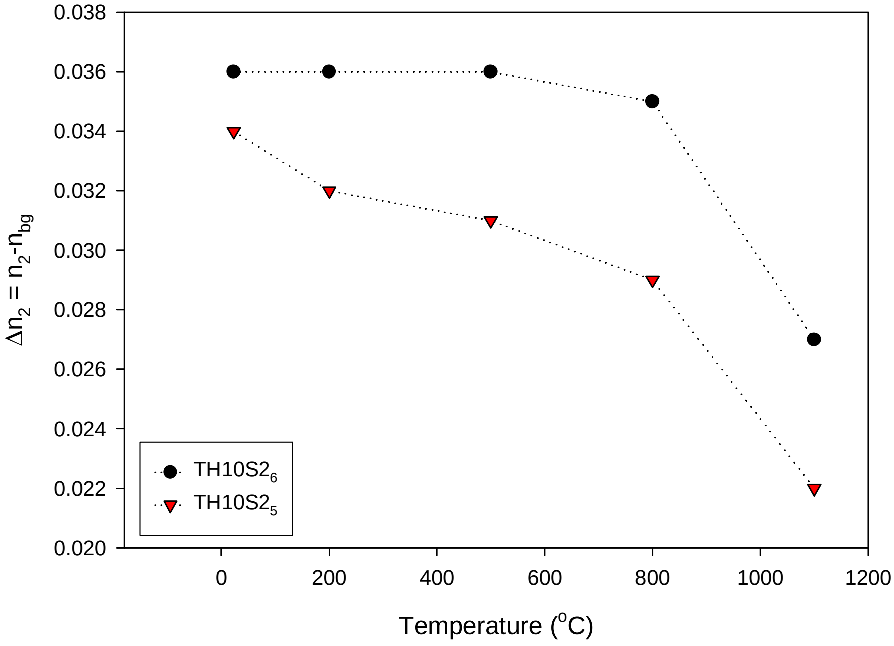

(b)

FIGURE 5.23: Local indices of refraction of the nano-grating formed in the irradiated volume of TH10S3$_5$ and TH10S3$_5$ calculated from (5.3) with $f_f = 0.3$, and using the experimental values of, $\Delta\phi_e$, $\Delta\phi_o$ and t_p. (a): $\Delta n_1 = n_1 - n_{bg}$, (b): $\Delta n_2 = n_2 - n_{bg}$.

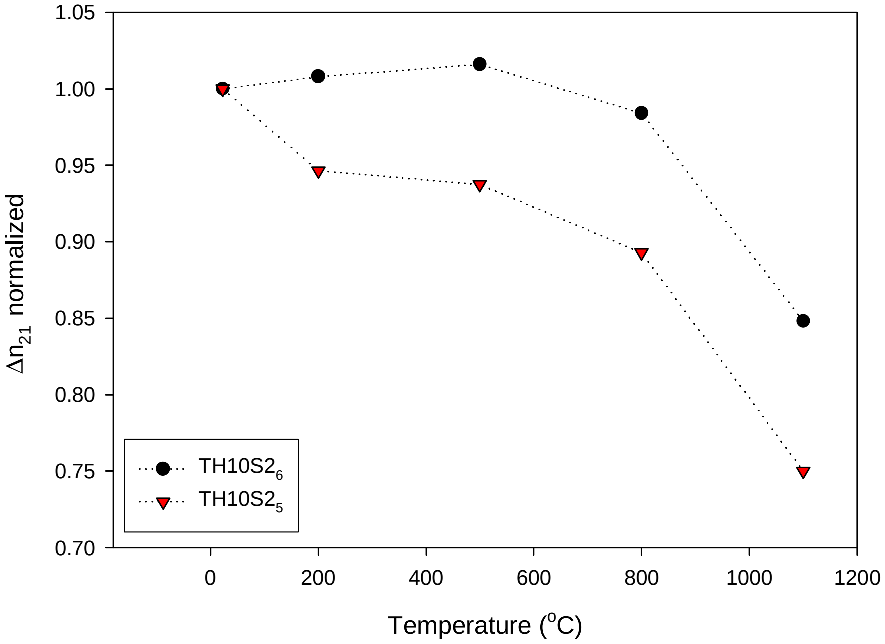

(a)

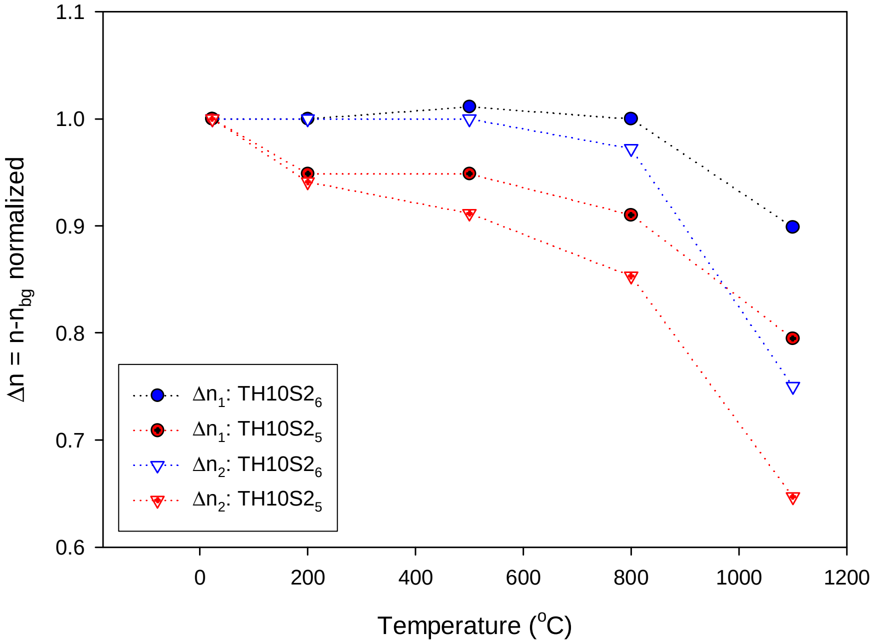

(b)

FIGURE 5.24: Local indices of refraction of the nano-grating formed in the irradiated volume of TH10S3$_5$ and TH10S3$_5$ calculated form (5.3) with $f_f = 0.3$, and using the experimental values of, $\Delta\phi_e$, $\Delta\phi_o$ and t_p. (a): $\Delta n_{21} = n_2 - n_1$ normalized to the value before any annealing step, (b): Δn_1 and Δn_2 normalized to their initial value (before annealing).

5.8 Conclusions

The analysis carried out on some of the structures created with the femtosecond direct writing technique, lead to the observation of a novel anisotropic effect, namely a strong reflection occurring only along the direction of the polarization of the writing laser. The reported results were interpreted as the first evidence of a self-assembled grating formed in the bulk of silica glass with its ruling parallel to the polarization of the writing laser, and whose period is smaller than the wavelength of light. This structure behaves as a Bragg grating, hence accounting for the anisotropic reflection. Moreover, it also explains the origin of the optical anisotropy, arising at the same intensity threshold as the anisotropic reflection, in terms of form birefringence. Furthermore, the presence of such a periodic structure in the irradiated volume supports the experimental observation of a polarization sensitive index change reported in some of the birefringent structures. Our observations suggest that, below a certain intensity threshold, the written structures are isotropic with a positive index change (type I-fs). However, when the intensity level used to irradiate the material is above this threshold, a periodic modulation in the refractive index change formed in the focal volume causes the written structures to behave as a negative birefringent material, additionally displaying anisotropic reflection and negative index change (type II-fs).

The behaviour of the index change versus the laser intensity, showed that the largest modification to the refractive index of the irradiated material is achieved at the highest intensity value utilized to process the material, i.e. when the laser was focused in tightest available conditions. However, since the thickness of the written structures depends on the focusing conditions, the maximum value of laser-induced phase retardation (almost 2π) was measured in a sample written with the laser focused by a weaker objective (10x).

Using the measured values for the laser-induced phase retardation we calculated the local indices of refraction of the grating formed by the laser in the focal volume (up to -0.1). This result was in agreement with the extraordinary stability shown by the birefringent structures versus the temperature increase, making the type II-fs of directly written structures attractive for the development of embedded photonic devices, such as half-waveplates and micro-reflectors.

Chapter 6

Self-assembled periodic nanostructures by femtosecond direct writing

All the results presented in the previous chapters strongly corroborated our initial speculation that self-assembled nanostructures are formed in the irradiated volume of silica glass. This theory had been formulated to justify birefringence, anisotropic reflection, and negative index change observed in the femtosecond laser directly written structures of type II-fs. However, any experimental evidence of the presence of modified regions of nanometer size was still missing.

In this chapter, we report the direct imaging of the nano-grating, both on the plane of propagation of light (Sec. 6.2), and on the perpendicular plane (Sec. 6.1, Sec. 6.3). The phenomenon is interpreted in terms of interference between the incident light field and a bulk electron plasma wave, resulting in periodic modulation of electron plasma concentration (Sec. 6.4). Finally, an alternative technique for the imaging of the sub-wavelength structures is discussed in Section 6.5 where, in addition, a polarization dependent etching rate of the nanostructures is demonstrated.

6.1 Direct observation of the laser-induced sub-wavelength modulation of the refractive index

In order to image the periodic assembly formed in the focal volume of the irradiated material, we initially attempted to utilize an Atomic Force Microscope (AFM) combined with a differential etching technique (Sec. 6.5). In parallel to our effort, a Japanese

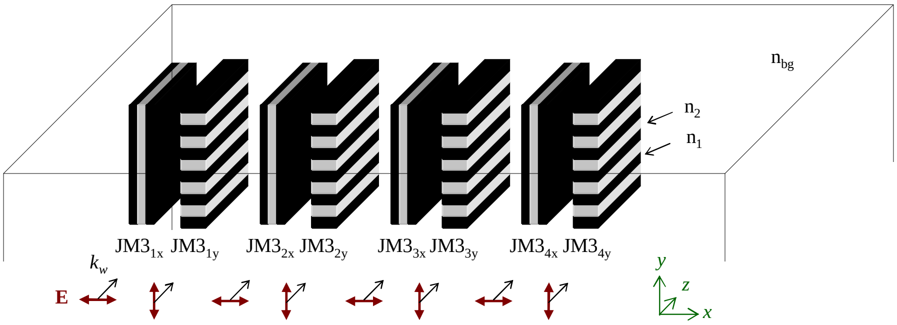

Figure 6.1: Schematic of the sample JM3 described in Table 5.1 showing how the self-assembled periodic structures are expected to be arranged. E: electric field of the writing laser, k_w wave vector of the writing laser propagationg along the z-axis.

team,[1] working in collaboration with our group, succeeded in the task utilizing Scanning Electron Microscopy (SEM) [91]. The reported results revealed the presence of stripe-like regions of $\sim 20\,nm$ width in the irradiated volume of silica glass. These periodic stripes were constituted of material with lower density and periods as small as $140\,nm$ aligned to the direction of the electric vector of the writing laser. As such, the existence of a self-assembled periodic structure formed by the interaction of ultrashort pulses and matter was finally experimentally verified.

6.2 Distribution of the self-assembled nano-grating in the plane of propagation of the writing laser

While the results presented by Shimotsuma et al. [91] had shown the image of the self-assembled nano-structures on the plane perpendicular to the propagation of the writing laser, here we present the investigation of the distribution of the periodic assembly on this plane (xz in Fig. 6.1). For this experiment we utilized the sample JM3 described in Section 5.1 on page 41. The sample was formed by pairs of directly written lines irradiated with different pulse energy levels. Each pair was fabricated in identical writing conditions, except that each line was produced with orthogonal polarization of the writing laser (Table 5.1). Figure 6.1 shows a schematic of the sample, where the expected geometry of the periodic assembly is sketched. As reported in Section 5.2, all the lines, with exception of JM3$_{1y}$ and JM3$_{1x}$, show birefringence. In addition, the lines written with the polarization along y (x), display blue reflection only when illuminated in the y (x) direction. The sample, had been polished in the xz plane back to the structures and etched for the experiment described in Section 6.5. After coating with a thin carbon film, was imaged under a scanning electron microscope (JSM-6500F) in backscattering

---

[1] **Yasuhiko Shimotsuma**, *R&D Center Kagoshima, Kyocera Corporation*, Japan, **Jiarong Qiu**, *Shanghai Institute of Optics and Fine Mechanics, Chinese Academy of Sciences and Japan Science and Technology Corporation*, Japan and **Kazuoki Hirao**, *Department of Material Chemistry, Graduate School of Engineering, Kyoto University*, Japan.

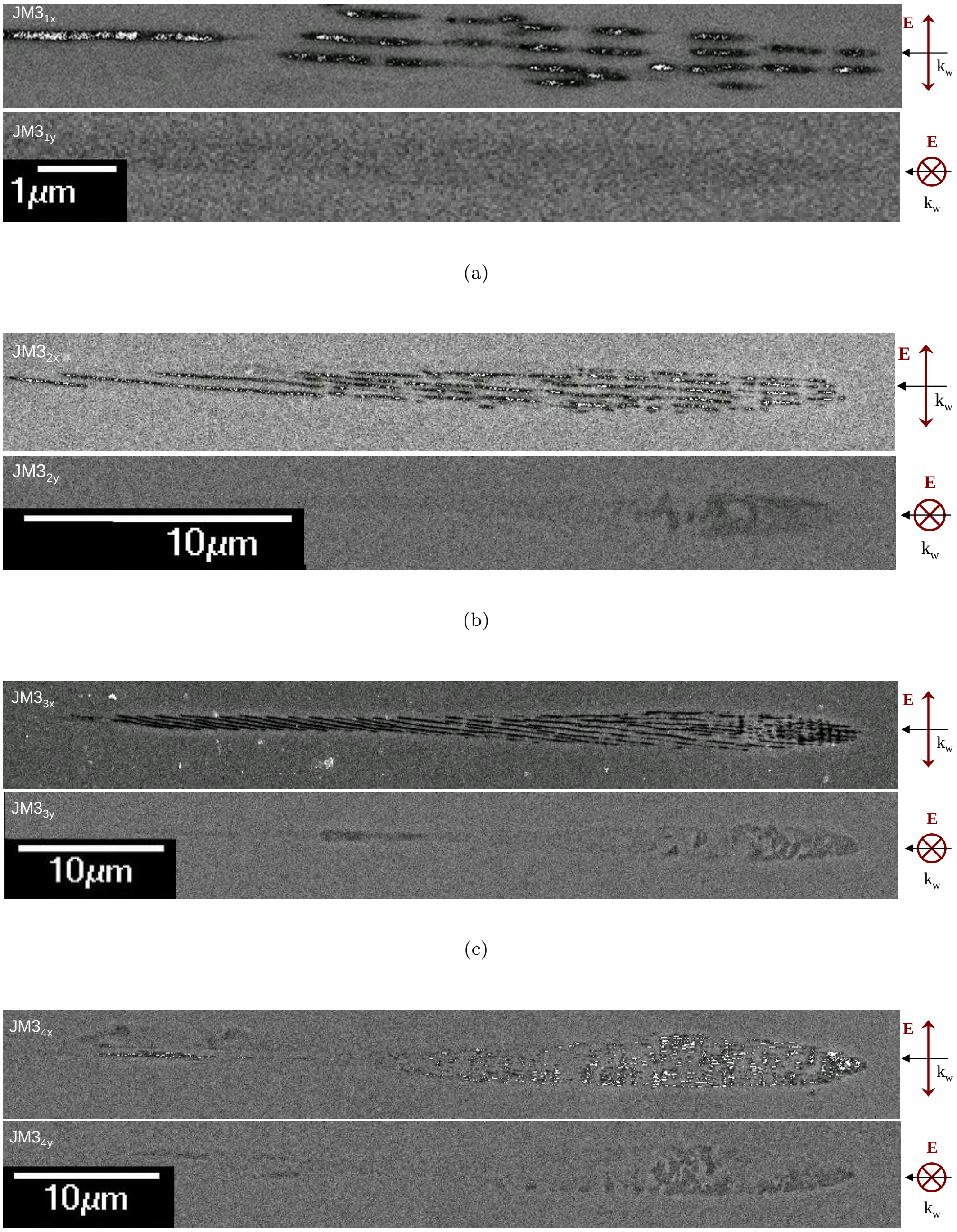

(a)

(b)

(c)

(d)

FIGURE 6.2: SEM BE images of the sample JM3 on the xz plane (See Table 5.1 for fabrication details).

emission mode (BE), which is sensitive to the atomic weight of the elements or the density of material constituting the observation surface (Fig. 6.2).

As expected, only the lines written with the polarization on the plane of observation

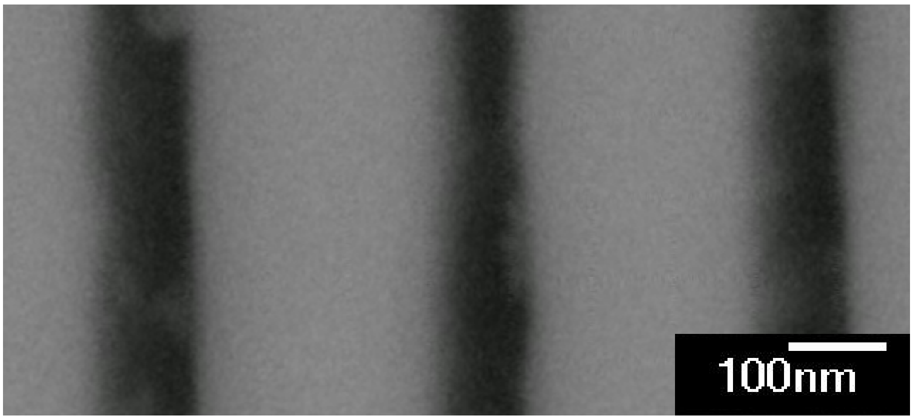

FIGURE 6.3: Detail of the sub-wavelength periodic structure formed in $\mathrm{JM3}_{3x}$.

(xz) reveal the periodic modulation of the index change (for these structures, in fact, xz is the plane parallel to the ruling of periodic assembly, hence perpendicular to the plates forming the nano-gratings). On the contrary, the corresponding lines, written in the same conditions, but with the polarization along y, show a homogeneous profile (for these structures, in fact, xz is the plane perpendicular to the ruling of periodic assembly, hence parallel to the plates forming the nano-grating). The line written at the highest value of pulse energy ($\mathrm{JM3}_{4x}$) displays a rather irregular distribution of the periodic structure (Fig. 6.2 d). On the contrary, all the other lines are characterized by well-ordered periodic dark stripes, arranged with their ruling parallel to the direction of the writing laser. Figure 6.3 is a close-up of the nano-grating revealing that the filling factor is $f_f \sim 0.3$, twice as high as the results reported in [91]. In addition, the image demonstrates an abrupt change of density between the stripes (i.e. the zones of refractive index n_1 in Figure 6.1) and the surrounding regions (i.e. the zones of refractive index n_2 in Figure 6.1), suggesting that the mechanism leading to the modulation of the refractive index is highly non-linear. Rather surprisingly, also the line $\mathrm{JM3}_{1x}$ is characterized by the presence of the stripe-like structures. When inspected between cross polarizers, this particular structure had not shown any birefringence, nor had its “twin” line $\mathrm{JM3}_{1y}$, which furthermore, had not manifested visible anisotropic reflection when illuminated with white light in the y direction (Fig. 5.4 on page 45). Hence, the threshold of birefringence for the sample JM3 was believed to be $0.24\,\mu J < E_b < 0.36\,\mu J$. However, this new experimental evidence reveals that $E_b < 0.24\,\mu J$, suggesting that the optical inspection might not be sensitive enough to discriminate the femtosecond structures belonging to type I-fs or type II-fs. The measurement of the index change for the ordinary and extraordinary wave should always be performed to complete the characterization. Indeed, in this particular case, the index change had not been measured, eventually leading to a temporary misjudgement in classifying the structures $\mathrm{JM3}_{3x}$ and $\mathrm{JM3}_{3y}$.

The SEM images of our sample allowed a closer inspection of the typical head-tail structure already observed under the optical microscope in Figure 5.1. In particular, it was revealed that the modulation of the index change is generally arranged more

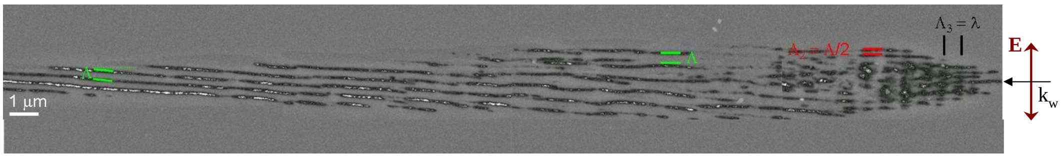

FIGURE 6.4: Zoom of the SEM image of $JM3_{3x}$ in which all the three periods Λ, Λ_2, and Λ_3 are highlighted.

Line	**Λ (nm)**	**Λ_2 (nm)**	**Λ_3 (nm)**
$JM3_{1x}$	260 ± 20	-	-
$JM3_{2x}$	320 ± 60	180 ± 25	-
$JM3_{3x}$	320 ± 60	220 ± 50	580 ± 30
$JM3_{4x}$	280 ± 50	190 ± 50	530 ± 30

TABLE 6.1: Values of Λ, Λ_2 and Λ_3 measured from Figure 6.2.

regularly in the tails than anywhere else in the written track. In addition, it was found that the periodicity is not uniform everywhere in the focal volume. Indeed, in certain parts of the cross-section of the written lines, it is possible to observe two distinct periods, one (Λ_2) is roughly half of the other (Λ) (Fig. 6.4). To verify this observation, the distance between adjacent stripes was repeatedly measured in each image. The results are shown in the histograms of Figure 6.5 (a), (b), (c), (d), which represent the frequency of *all* the counts for each written line versus the measured period. It may be noticed that a two-peaks structure is visible in most of the histograms, however it is not extremely pronounced. The presence of two distinct periods Λ and Λ_2 became extremely clear in $JM3_{3x}$ when, the counts of the periodicity performed in the head, in the tail, and in the central part of the track were considered independently (Fig. 6.5 (e)). The resulting periods were obtained by fitting the histograms with Gaussian curves; these values are summarized in Table 6.1. It is interesting to highlight that the evidence of the presence of two periods Λ and Λ_2 in the structure $JM3_{3x}$ finally explains the appearance of two maxima in the reflection spectrum (reported in Section 5.2) collected from its twin structure $JM3_{3y}$. Furthermore, in some of the images of the cross-sections of the lines, a third periodicity Λ_3 was identified perpendicular to Λ and Λ_2, and hence orthogonal to the direction of propagation of light (Table 6.1). This periodicity, clearly visible in Figure 6.4, is confined to the first few micrometers of the head of the written tracks. These experimental observations will be discussed in Section 6.4.

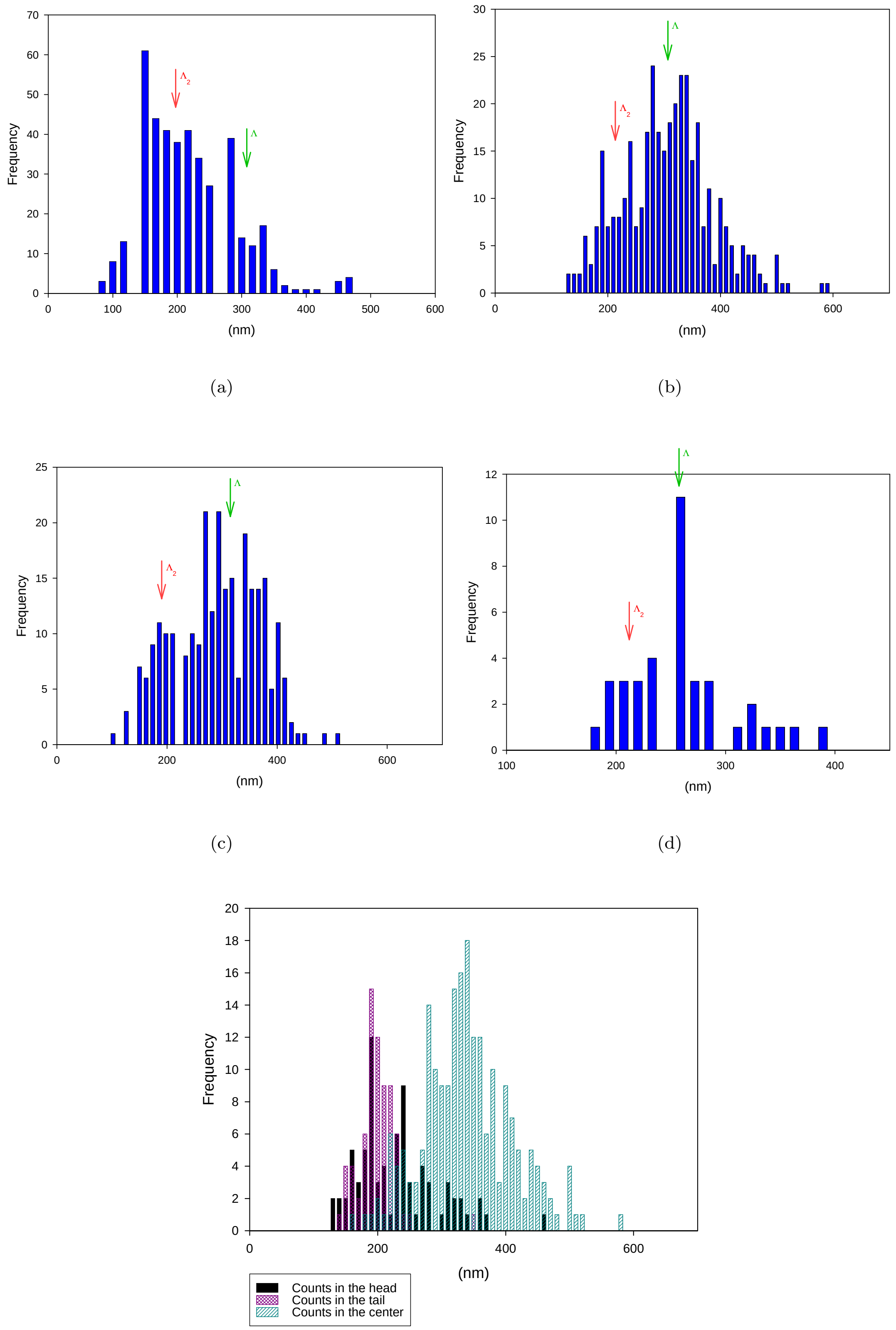

(a)

(b)

(c)

(d)

(e)

FIGURE 6.5: Histograms representing the frequency of counts of the period Λ versus its value for some of the direct written lines of the sample JM3. (a) $JM3_{4x}$, (b) $JM3_{3x}$, (c) $JM3_{2x}$, (d) $JM3_{1x}$. (e): histogram representing the measurements of the period in $JM3_{3x}$ performed in the head, in the tail and central part of the track.

6.3 Spatial coherence

As a further analysis, we studied how the self-assembled periodic structures arrange themselves across adjacent written zones. For this experiment, we chose Fresnel zone plate B, described in Section 4.4, as it offered a wide area to be imaged under the SEM and additionally, it was written in similar conditions to the sample JM3 analyzed in the previous section. The silica plate containing the FZP was polished on the plane perpendicular to lens's axis (xy plane) until the direct written Fresnel rings were brought to the surface and, after being coated with a thin gold layer, the sample was analyzed with an SEM (JSM-5910) in backscattering emission mode. Figure 6.6 shows how the laser processed zones are easily distinguished from pure silica by the presence of the nanostructures. As expected, the ruling of the grating ($\Lambda = 320\,nm \pm 50\,nm$) is perpendicular to the direction of the polarization of the writing laser. In addition, the image clearly shows that the self-assembled nanostructures formed in adjacent lines are aligned. As described in Chapter 4, the Fresnel rings were realized by writing adjacent circles with a spacing between them smaller than the writing resolution, hence the processed zones are formed by a series of partially overlapped directly written circles (Fig. 6.6). Given the geometry of the lens and the speed of the translation stage, point B in Figure 6.6 was written $\sim 2\,s$ after point A. Despite the long time elapsing between the formation of the periodic structures in the two points, the nano-grating is continuous across the two written lines. This evidence suggests that the structure imprinted in a line provides an

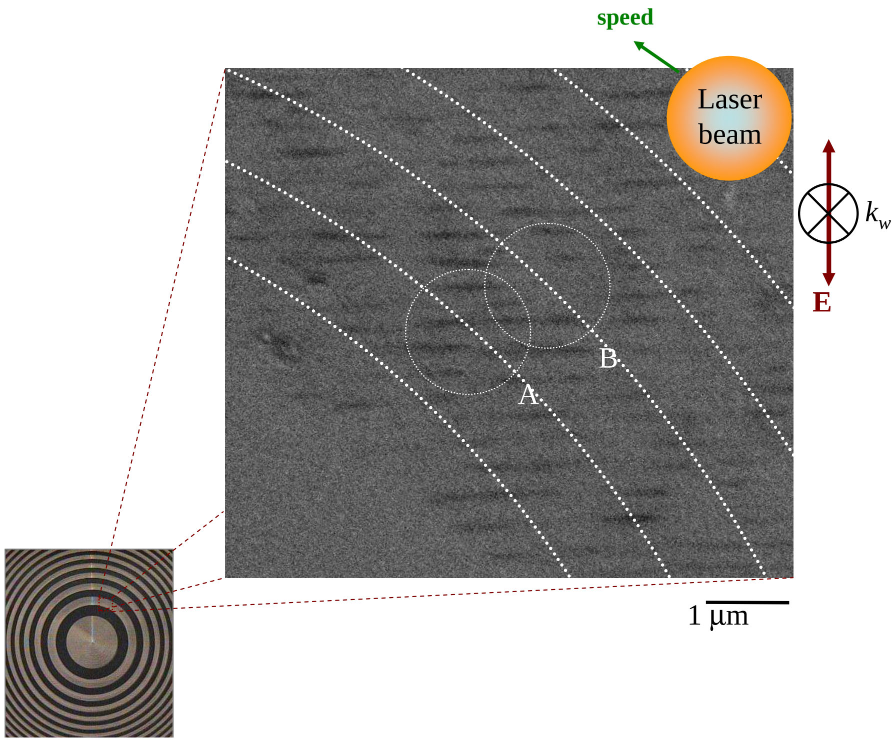

Figure 6.6: SEM image of the nano-gratings in Fresnel zone plate B.

initial "seeding" condition during the formation of the self-organized periodic assembly in the adjacent line. This is a very important property as it demonstrated the ability of realizing periodic nanostructures on an area of the desired dimensions, rather than being limited to the size of the focused spot.

6.4 Optical/plasma wave interference to explain the formation of self-organized form birefringence

Surface ripples with a period equal to the wavelength of incident laser radiation and that are likewise aligned in a direction perpendicular to the electric field of the light wave, have been observed in many experiments involving laser deposition [90] and laser ablation [95]. Such gratings are generated as a result of interference between the light field and the surface plasmon-polariton wave that is launched because of initial random surface inhomogeneities. However, until now there has been no observation of periodic structures being generated within the bulk of a material just by a single writing laser beam. We suggest that the self-organized nano-structures are produced by a pattern of interference between the incident laser radiation and a plasma wave generated within the sample.

Once a high free electron density is produced by multiphoton ionization, the material in the focal volume is a plasma. A characteristic peculiarity distinguishing a plasma from other media is the possibility of existence therein of longitudinal electrical oscillations (plasma or Langmuir waves), namely waves whose electric field component is parallel to the direction of propagation (Sec. A.2.1). When an electromagnetic wave is propagating through a plasma in the presence of density fluctuations, plasma waves can be generated [96].

We suggest that once generated, a Langmuir wave interferes with the electromagnetic wave creating a periodic modulation of the electron plasma concentration, which finally becomes frozen within the material. The electron plasma wave is efficiently generated only with wave vector $\mathbf{k_{pl}}$ in the plane of light polarization and only in the direction defined by conservation of the longitudinal component of the momentum (Fig. 6.7 (a)). Consequently, the interference pattern has to be perpendicular to the direction of the laser propagation (hence parallel to the polarization of the laser). The amplitude of the wave vector of the plasma wave is defined by this momentum conservation condition [54]:

$$k_{gr} = \frac{2\pi}{\Lambda} = \sqrt{k_{pl}^2 - k_w^2}, \tag{6.1}$$

where k_w is given by the dispersion relation of an electromagnetic wave propagating in plasma

$$\omega^2 = \omega_p^2 + \frac{c^2}{n_{bg}^2} k_w^2, \tag{6.2}$$

with ω_p the plasma frequency (A.19). Hence, given the material and the optical frequency, k_w only depends on the plasma electron density. k_{pl} in Equation 6.1 is given by the dispersion equation for the plasma wave (A.27):

$$\omega_{pl}^2 = \omega_p^2 + \frac{3}{2} v_e^2 k_{pl}^2,$$

where for the energy conservation $\omega_{pl} = \omega$.

Figure 6.7 (a) elucidates the interference mechanism between the electron plasma wave and the electromagnetic field giving rise to the grating with period Λ, offering an explanation of the appearance of the self-assembled nanostructures. Indeed, the presence of $\Lambda_2 = \Lambda/2$, observed in Figure 6.4 can now be explained, considering the interference between the two plasma waves satisfying (6.1) (Fig. 6.7 (b)). In analogy, also Λ_3 may be explained as a result of interference between waves. In this case, though, it is necessary to invoke the interaction of all the three waves, namely the two plasma waves and the electromagnetic field as sketched in Figure 6.7 (c). If this is the case, it can be seen that $\Lambda_3 = \lambda_w$. Indeed, this is in good agreement with the experimental results on the value of Λ_3 reported in Table 6.1. The wavelength of the electromagnetic wave, which in air is $800\,nm$, due to the dispersion becomes $\sim 550\,nm$ in glass. In presence of a plasma λ_w increases according to (6.2), where $\lambda_w = 2\pi/k_w$. Using (6.2) to calculate the plasma frequency w_p, from Equation A.19 the maximum measured value of $\lambda_w = 580\,nm$ corresponds to a plasma density of $\sim 10^{20}\,cm^{-3}$, which is in excellent agreement with the value found in [73].

Although this theory of optical/plasma wave interference is extremely interesting and would justify the presence of all the three periods observed experimentally, however it leaves space to some criticism. In particular, from Equation A.27 we can see that the amplitude of the plasma wave vector depends on the electron density (via ω_p Equation A.19) and electron temperature (via v_e), which are both spatially and temporally varying. This makes difficult to understand the mechanisms which preserve the periodicity while the plasma is cooling and highlight the need for further investigations.

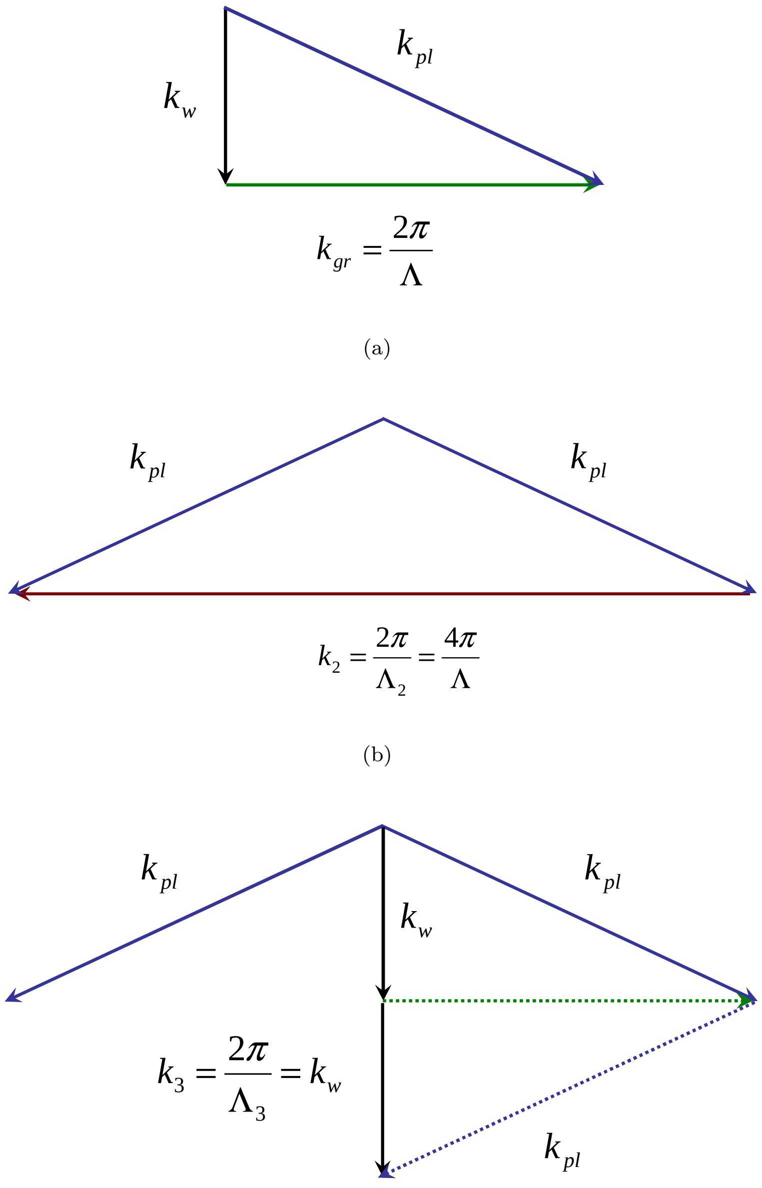

(a)

(b)

(c)

Figure 6.7: Diagram explaining the interference between the light wave and plasma waves, giving rise to the three periods observed in Figure 6.4. k_{pl} is wave vector of electron plasma wave, k_w is wave vector of light. (a): interference diagram for the grating of period Λ (b): Two waves interference between the two plasma waves satisfying (6.1) and originating in a grating with period $\Lambda_2 = \Lambda/2$. (c): Three-waves interference between two plasma waves and the light wave originating in a grating of period Λ_3.

6.5 Anisotropic etching rate in structures of type II-fs

In our first attempt to image the periodic modulation of the index change imprinted in the laser modified regions, an atomic force microscope (AFM) was utilized. This device is equipped with a probing tip of a few nanometer radius, which is scanned almost in contact with the surface of the sample under test. Exploiting the relationship between the attractive/repulsive forces applied on the tip, and the distance between the tip and the sample, it is possible to obtain a profile map of the area of interest with nanometer resolution. Indeed, such resolution is adequate for the dimensions of the sub-wavelength structures. However, to enable the AFM to "image" the periodic assembly, it is necessary to transform the modulation of the index change into a surface relief. This was attempted exploiting the different etching rate of materials with a diverse index change. Indeed, wet chemical etching in hydrofluoric acid (HF) of cleaved optical fiber, followed by atomic force microscopy, was used to achieve a surface profile which is a replica of the index distribution [80, 97]. However, while the etching rates for pure and doped silica are well documented, no information is available on the behaviour of the laser modified regions. The sample was etched with a series of different solutions in turn with the aim of finding a set of parameters (acid concentration and etching time) which allowed the imaging of the index modulation between n_1 and n_2. After each process, the sample was analyzed under the AFM. If the etch time was too long, a deep track was formed correspondingly to the written lines, and the AFM probe tip could not map the topography. In this case, the xz plane of the sample was polished again, before a new HF solution was applied. In order to avoid loosing the written lines (of 700 μm length) with the etching and lapping of the sample, the process was attempted for a last time with a solution of 5% HF for 2 minutes (Fig. 6.8). It is interesting to note that the two "twin" structures analyzed with the AFM (JM3$_{4x}$ and JM3$_{4y}$ of Figure 6.1) showed a different response to the same etching solution. In JM3$_{4y}$ the material removal was small enough to enable the AFM tip to image the bottom of the groove and, as expected, no periodic structures were imaged in this line (Fig. 6.8 (a)). On the contrary, the groove formed in correspondence with JM3$_{4x}$ was still too deep to allow the imaging of the index profile (Fig. 6.8 (b)). This behaviour proves that the two lines have a different

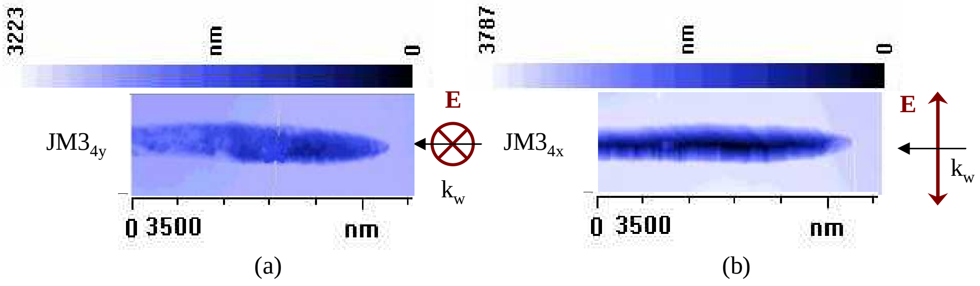

(a) (b)

Figure 6.8: AFM images of the sample JM3 after etching the xz plane with a solution of HF 5% for 2 minutes. (a): Part of the line JM3$_{4y}$.(b): Part of the line JM3$_{4y}$.

etching rate, which may be ascribed to the geometry of the periodic structures in the two lines (Fig. 6.1). In the structures fabricated with the writing polarization perpendicular to the imaged plane, the written region has a homogenous refractive index on the (xz) plane, hence the acid acts on the periodic assembly plane by plane. On the contrary, in the lines written with the polarization on the xz plane, the area exposed to the acid is characterized by a modulation of the refractive index, whose depth Δn_{21} can be as high as 0.1 (Section 5.4). We therefore suggest that in these latter structures, the HF solutions etches one of the two material (n_1 or n_2) much faster than the other, hence exposing a larger area of the remaining material to the eroding action. Consequently the etching rate of these lines is faster, as demonstrated from our experimental evidence.

After this initial experiment, we chose to image the modulation of the refractive index with the SEM, which can reveal the sub-wavelength periodic structure without the need for etching of the sample. However, recent results have proved the validity of the AFM/etching technique [98].

6.6 Conclusions

The successful imaging of the self-assembled form birefringence created by irradiating silica glass with a femtosecond laser, conclusively proved the theory constructed to explain the anisotropic reflection, uniaxial birefringence and the polarization dependent sign of the index change reported in the previous chapters.

The observation of the index modulation created in the glass on the plane of the propagation of light, gave evidence of interference between the light wave and longitudinal electron plasma waves, which allowed the explanation of the physical mechanism behind the formation of the *smallest signature of light* ever reported.

Besides revealing the presence of three distinct periods, which were explained as the result of two and three-waves interference between the longitudinal plasma waves excited in the plasma and the electromagnetic field propagating through it, the images acquired with the SEM (Fig. 6.2) contain even more interesting features, whose explanation may lead, in the future, to a better understanding of the interaction between ultrashort laser and silica glass. In particular, our attention was captured by the aspect ratio of the modulation of the index change. The small width of the black stripes appearing in the SEM images had been already observed in [91], where it was furthermore demonstrated that these regions were characterized by oxygen deficiency. This may suggest that, during the formation of the structural change, the presence of clouds of electrons may locally repel negative ions. However, the dynamics of the energy deposition process are still largely unexplained and more investigation is still required. Furthermore, the most astonishing feature, emerging from the images of Figure 6.2, was the evidence of a tilt of the nano-grating with respect to the direction of the propagation of the writing light, appearing in the tails of the tracks (Fig. 6.4). Indeed, this observation is currently under investigation and no explanation has been yet formalized.

Finally, the spatial coherence displayed by the self-assembled nanostructures make them extremely attractive for new applications such as embedded micro-reflectors, or photonic band-gap devices.

Chapter 7

Study of the femtosecond laser-induced index change in various transparent materials

The reduced requirements on the photosensitivity necessary to modify the properties of the materials irradiated by ultrashort pulsed sources makes this class of laser a promising processing tool, especially for those materials which have proved to be challenging via other methods. Although femtosecond lasers can modify any material, nonetheless, as was discussed in the previous chapters, depending on the laser intensity, and the material parameters, one can achieve positive or negative index change, or even voids. It is clear that a characterization of the response to the femtosecond irradiation of the key materials developed and utilized in the photonic industry is required. This chapter therefore presents a collection of results concerning the measurement of the index change[1] induced by the femtosecond laser in some in-house made glasses (glass-ceramics (Sec. 7.1), bismuthate (Sec. 7.2), and chalcogenide glass (Sec. 7.3)), as well as commercial sapphire crystal (Sec. 7.4), and silicate glasses (Sec. 7.5).

During the analysis of the response of all these transparent materials to the irradiation by a femtosecond pulsed laser, particular attention was dedicated to the verification of the formation of sub-wavelength periodic structures, which were observed in SiO_2 and discussed in the previous chapters. Direct imaging of this self-assembled nano-grating within the irradiated volume requires the costly utilization of a SEM (Sec. 6.1). However, in (Sec. 5.3), it was demonstrated that the negative sign of the refractive index and the onset of uniaxial birefringence in the laser processed regions are signs of the formation of sub-wavelength periodic structures. Hence, the presence of the nano-grating, was

---

[1] The interferometric setup utilized for the characterization of the samples measures the phase retardation induced in the laser written regions, which is proportional to the laser-induced index change (Sec. 3.2). Wherever possible, the thickness of the written regions t_p was measured and the value of the index change derived from (3.6).

SAMPLE EMF		
E_p (μJ)	**EMF10**	**EMF50**
2.40 μJ		$EMF50_{10}$
2.00 μJ		$EMF50_9$
1.75 μJ		$EMF50_8$
1.50 μJ	$EMF10_7$	$EMF50_7$
1.25 μJ	$EMF10_6$	$EMF50_6$
1.00 μJ	$EMF10_5$	$EMF50_5$
0.75 μJ	$EMF10_4$	$EMF50_4$
0.50 μJ	$EMF10_3$	$EMF50_3$
0.25 μJ	$EMF10_2$	$EMF50_2$
0.10 μJ	$EMF10_1$	$EMF50_1$

Table 7.1: Fabrication details of the sample EMF, written in nanostructured optical grade Tm-doped SiO_2:SnO_2 glass-ceramic with the setup described in Section 3.1, with $\lambda_w = 800\,nm$, $r = 100\,kHz$, $\tau \sim 200\,fs$, $s_s = 80\,\mu m/s$. The laser was focused via the 10x (50x) objective for the squares of EMF10 (EMF50) and linearly polarized.

inferred, in a practical way, utilizing the setups described in Section 3.2 and Section 3.3.

Some of the glasses analyzed in this chapter, were provided by research groups developing new glass compositions for specific photonic applications. The part of these collaborative works relevant to this thesis is limited to the measurement of the laser-induced index change, and the investigation of the presence of laser-induced self-assembled form birefringence in the irradiated volume. For this reason the overview of each material is reported very briefly, and the further results following these initial characterization steps are not included here.

7.1 SnO_2 nanostructured silica glass-ceramics

We have analyzed the index change induced in a nanostructured optical grade Tm-doped SiO_2:SnO_2 glass-ceramic, recently developed in the Department of Science and Materials of Milan University[2]. Due to its low-absorption losses at $1.5\,\mu m$ (comparable with pure silica), high-third-order non-linearity, and a small crystallite size, this material is very promising for photonic applications [99]. The sample was synthesized from a modified sol-gel route [100], and a reference silica sample without SnO_2 nanoclusters was prepared for comparison following the same procedure.

The writing setup described in Section 3.1 was used to irradiate the two samples. The wavelength of the laser was $800\,nm$, the pulse duration was $\sim 200\,fs$ and the repetition rate was $100\,kHz$. Squares of $(100\,\mu m)^2$ were written at a constant speed of $80\,\mu m/s$, both in the glass-ceramic (EMF10, EMF50) and in the glass reference samples (REF10,

---

[2] The glass samples utilized for the experiment described in this section had been provided by Dr. E. Franchina, Dipartimento di Scienza dei Materiali, Università di Milano-Bicocca, Italy.

SAMPLE REF		
E_p (μJ)	**REF10**	**REF50**
2.00 μJ	$\mathrm{REF10_9}$	$\mathrm{REF50_8}$
1.75 μJ	$\mathrm{REF10_8}$	$\mathrm{REF50_7}$
1.50 μJ	$\mathrm{REF10_7}$	
1.25 μJ	$\mathrm{REF10_6}$	$\mathrm{REF50_6}$
1.00 μJ	$\mathrm{REF10_5}$	$\mathrm{REF50_5}$
0.75 μJ	$\mathrm{REF10_4}$	$\mathrm{REF50_4}$
0.50 μJ	$\mathrm{REF10_3}$	$\mathrm{REF50_3}$
0.25 μJ	$\mathrm{REF10_2}$	$\mathrm{REF50_2}$
0.10 μJ	$\mathrm{REF10_1}$	$\mathrm{REF50_1}$

TABLE 7.2: Fabrication details of the sample REF, written in silica glass with the setup described in Section 3.1, with $\lambda_w = 800\,nm$, $r = 100\,kHz$, $\tau \sim 200\,fs$, $s_s = 80\,\mu m/s$. The laser was focused via the 10x (50x) objective for the fabrication of the squares of REF10 (REF50) and linearly polarized.

REF50). The energy density was varied from one region to the other changing either the focusing objective, or the energy level (Tab. 7.1, Tab. 7.2).

After the irradiation, the samples were optically inspected to verify the presence of birefringence (Sec. 3.3) and finally, the difference in optical path between the irradiated and unprocessed regions, experienced by the probing laser while traversing the samples, was measured with the setup of Section 3.2. The measurements reported in Figure 7.1, where the phase change is proportional to the laser-induced index change, were repeated with the probing light polarized in the direction of the electric field of the writing laser $\Delta\phi_e$, and orthogonal ($\Delta\phi_o$).

The results revealed that all the squares written in the reference silica glass (REF), which does not contain SnO_2 nanoclusters, display negative values of the phase shift (corresponding to a lowering of the effective refractive index in the irradiated regions) regardless of the objective utilized to focus the beam. In addition a large birefringence is observed, with a higher refractive index (in absolute value) in the direction parallel to the polarization of the writing beam. This behaviour, combined with a negative index change, is in good agreement with the results reported for fused silica, in Chapter 5, and it can be ascribed to the formation of self-assembled nano-gratings within the processed area. Unlike fused silica, no positive index change could be achieved in the sample. This discrepancy with the previous results might be explained considering the uncertainty related to the pulse duration. Indeed, a change in the temporal width of the pulse would shift the energy threshold for the onset of birefringence.

On the contrary, the glass-ceramic sample containing nanoclusters displays a totally different response to the femtosecond laser irradiation as compared to silica. Remarkably, the modification of the refractive index changes sign accordingly to the focusing conditions, namely it is negative for the low-NA (EMF10) and positive for the high-NA

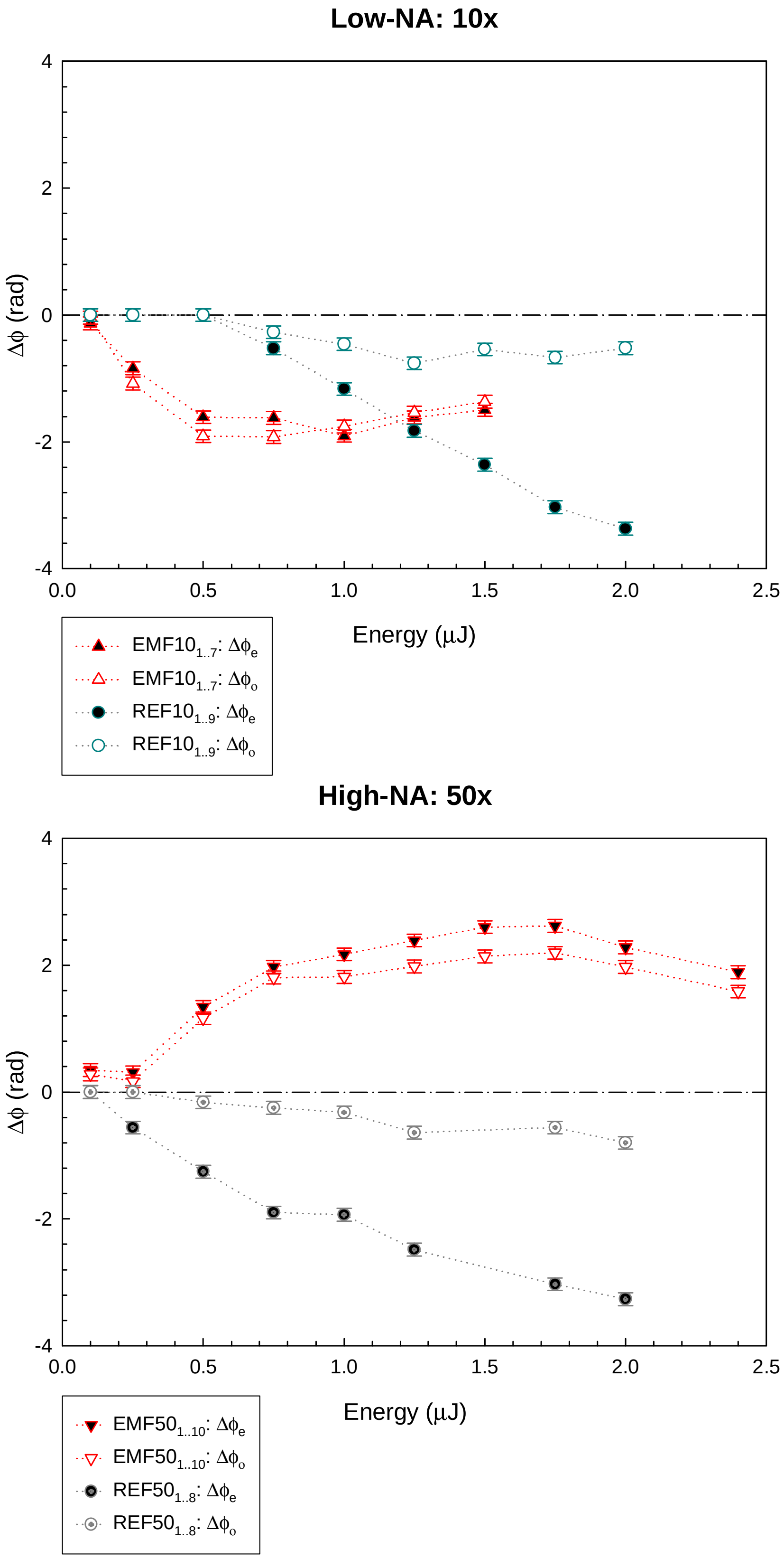

FIGURE 7.1: Laser-induced phase retardation versus the pulse energy, measured for the ordinary ($\Delta\phi_o$) and extraordinary ($\Delta\phi_e$) wave. (Top): REF10 and EMF10. (Bottom): REF50 and EMF50. Refer to Table 7.1 and Table 7.2 for experimental details.

(EMF50). Moreover, the regions in EMF50, display some birefringence, which is nevertheless smaller than in the reference sample, while the squares processed in EMF10, have a negligible birefringence.

Indeed, the negative phase shift in the regions of the glass-ceramic sample irradiated at low-NA (Fig. 7.1) is consistent with the negative photorefractive effect observed in previous experiments with unfocused ns-pulsed or CW laser sources in the same kind of material [101, 102]. This effect was interpreted to occur as of the amorphization of the cluster surface and the consequent lowering of the refractive index. Also, as already mentioned, the negative shift observed in the reference glass is just the result of the onset of self induced form birefringence. Therefore, the positive phase-shift displayed by the squared regions of EMF50 cannot be interpreted as the superposition of the independent responses of the coexistent phases, silica and SnO_2 nanoclusters, since the resulting effect should be negative. In other words, a new process takes place at high-NA focusing.

Further investigations were carried out on the glass-ceramic sample utilizing Raman spectroscopy and TEM[3]. The results, reported in [103] suggest that the new mechanism involves relevant reduction of the fraction of crystalline nanophase present with a structural effect on the glassy host. In particular, the growth of a broad bell-shaped band was observed centred at about $560\,cm^{-1}$ ascribable to amorphous-like SnO_2 [104], and the shift of the silica ω_1 band [105] to $440\,cm^{-1}$ at higher energy. The analysis of the process shows that the non-linear interaction between intense laser pulses and oxide nanoparticles triggers a chain of physical mechanisms giving the superposition of competitive negative and positive refractive index changes, caused by nanophase amorphization, and silica compaction.

The different behaviour displayed by EMF10 with respect to the response of the regions irradiated in tighter focusing conditions (EMF50), can be justified considering that the optical absorption edge of the material is in the range $450 - 350\,nm$ [102], and hence this mechanism implies two-photon absorption. As a result, in a high-NA condition, the beam attenuation is negligible far from the focus and the energy is absorbed in a narrow region at high power density. In fact, Raman data show detectable effects in a restricted volume close to the focal layer [103]. In the low-NA focusing condition, the power losses due to non-linear processes are distributed along a larger distance. This fact prevents the occurrence of a high density of two-photon events close to the focus and the structural modifications of the nanophase.

As regards birefringence, we note that it is barely detectable in glass-ceramic in the structures written at high-NA, and it is negligible in the regions processed at low-NA. This indicates that the interference mechanism occurring in glass, responsible for the creation of form birefringence, is not relevant in this nanostructured material, mainly

---

[3] These experiments have been carried out and analyzed by Dr. E. Franchina

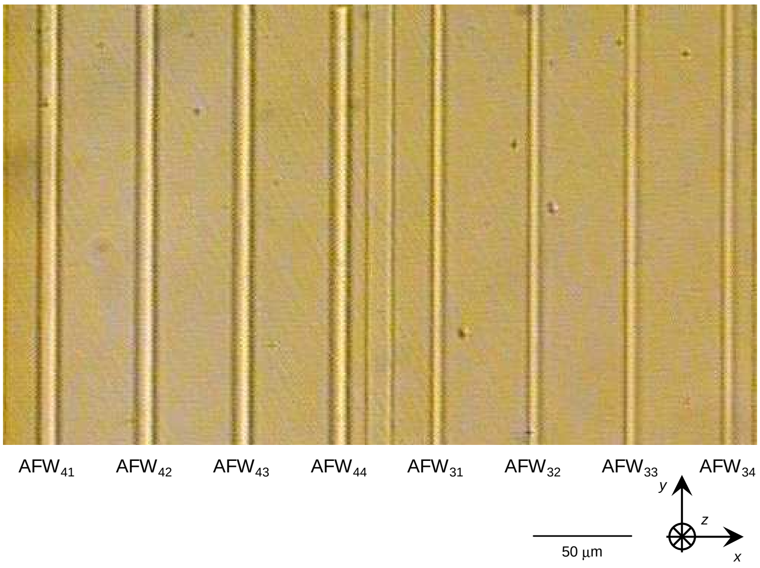

FIGURE 7.2: Microscope image of some of the lines of bismuthate sample AFW (Tab. 7.3).

because the radiation is principally absorbed by nanoparticles, making multi-photon events of glass ionization much more rare. On the other hand, since the weak birefringence of the glass-ceramic is observed only at high-NA, a relationship with anisotropic stresses due to the micro-machining seems likely.

7.2 Bismuthate glass

Bismuthate glasses have recently attracted attention as promising materials for the realization of amplifiers. Compared to silicate glasses, Bi_2O_3-based glass can accept a high concentration of Er^{3+} with broadband emission [106, 107]. This represents a potential for making compact amplifiers such as erbium-doped planar waveguide amplifiers. An oxide composition based on Bi_2O_3, fabricated in the ORC[4], was irradiated by femtosecond pulses with the writing setup described in Section 3.1 ($\lambda_w = 800\,nm$, $\tau \sim 200\,fs$, and $r = 100\,kHz$). The beam was polarized parallel to the direction of translation of the sample, and focused by the 50x objective ($NA = 0.55$). Several lines were written in the sample by translating the stage at constant speed along y. All the lines were written $50\,\mu m$ under the surface and the laser dosage was varied from one to the other either increasing the energy or varying the translation speed (Tab. 7.3, Fig.7.2). After writing, the sample was optically inspected, and no birefringence could be detected on the xy plane. The end faces (yz) of the sample were polished to allow the measurement of the written lines in the z direction (Tab. 7.3).

Figure 7.3 shows the measured index change of the lines, written in the bulk of bis-

---

[4] The samples of Bi_2O_3 utilized for the experiments reported in this section were prepared by Dr A. Favre.

SAMPLE AFW				
E$_\mathbf{p}$ (μJ)	**40 μm/s**	**t$_\mathbf{p}$** (μm)	**80 μm/s**	**t$_\mathbf{p}$** (μm)
2.72 μJ	AFW$_{61}$	91.0 ± 2.5	AFW$_{62}$	79.0 ± 2.5
2.00 μJ	AFW$_{51}$	67.0 ± 2.5	AFW$_{52}$	64.0 ± 2.5
1.50 μJ	AFW$_{41}$	67.0 ± 2.5	AFW$_{42}$	62.0 ± 2.5
1.00 μJ	AFW$_{31}$	46.0 ± 2.5	AFW$_{32}$	48.0 ± 2.5
0.50 μJ	AFW$_{21}$	37.0 ± 2.5	AFW$_{22}$	37.0 ± 2.5
0.10 μJ	AFW$_{11}$	31.0 ± 2.5	AFW$_{12}$	31.0 ± 2.5
	120 μm/s	**t$_\mathbf{p}$** (μm)	**160 μm/s**	**t$_\mathbf{p}$** (μm)
2.72 μJ	AFW$_{63}$	77.0 ± 2.5	AFW$_{64}$	82.0 ± 2.5
2.00 μJ	AFW$_{53}$	63.0 ± 2.5	AFW$_{54}$	63.0 ± 2.5
1.50 μJ	AFW$_{43}$	65.0 ± 2.5	AFW$_{44}$	65.0 ± 2.5
1.00 μJ	AFW$_{33}$	51.0 ± 2.5	AFW$_{34}$	48.0 ± 2.5
0.50 μJ	AFW$_{23}$	37.0 ± 2.5	AFW$_{24}$	37.0 ± 2.5
0.10 μJ	AFW$_{13}$	26.0 ± 2.5	AFW$_{14}$	n.a.

TABLE 7.3: Fabrication details of the sample AFW, written in Bi_2O_3-based glass, with the setup described in Section 3.1, with $\lambda_w = 800\,nm$, $r = 100\,kHz$, $\tau \sim 200\,fs$. The laser was focused via the 50x objective (NA=0.55) and linearly polarized in y. This table also reports the measurement of the thickness of the lines in the z-axis (t_p).

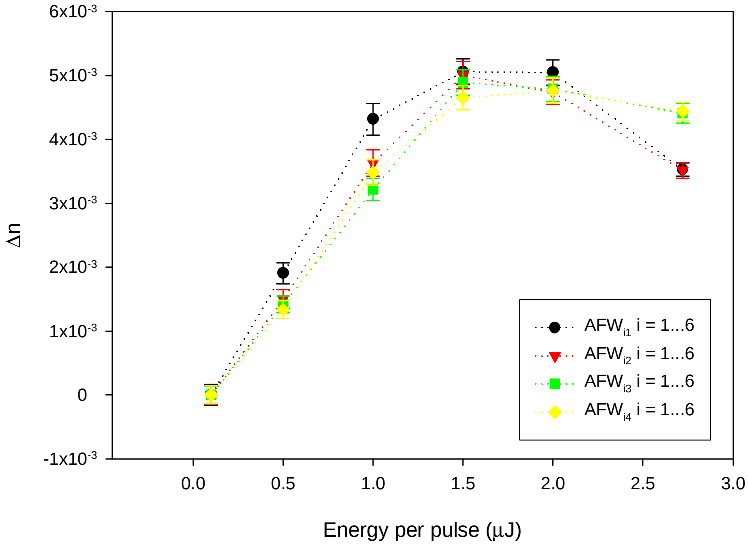

FIGURE 7.3: Laser-induced index change in the written lines of the sample AFW (Tab. 7.3).

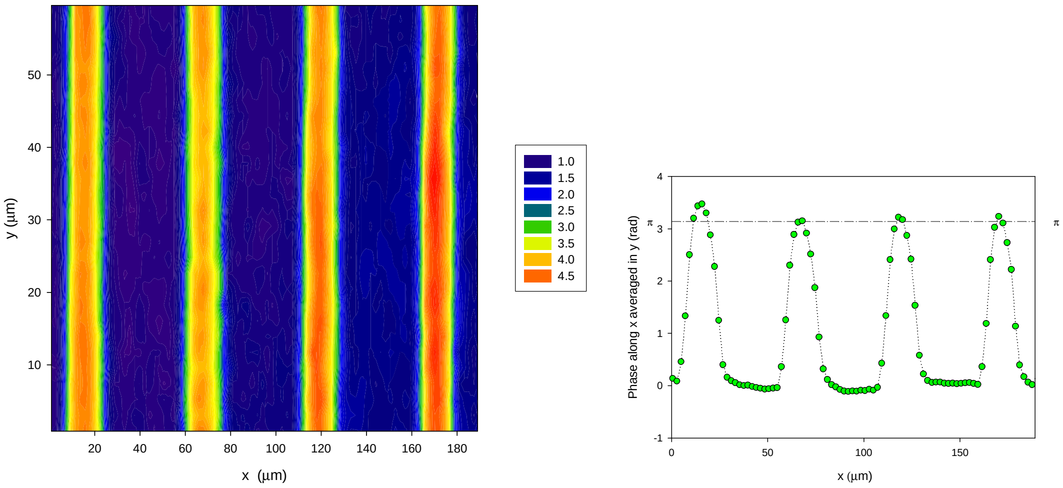

(a) (b)

Figure 7.4: (a): Phase map of part of the sample AFW, representing the phase retardation of the probing light traversing the sample. (b): Phase retardation along x, averaged in y and corrected to a zero background.

muthate, versus the energy delivered to the sample. In all the structures the modification of the refractive index has a positive sign, with a maximum of $(5.1 \pm 0.2) \times 10^{-3}$ in AFW$_{51}$, one order of magnitude higher than the index modification previously achieved in the same glass by UV-writing [12]. Furthermore, while the results reported in [12] indicated that the positive index change was confined to the region *surrounding* the laser processed (and damaged) area, in our case, the index change was induced in the region irradiated by the femtosecond laser, as can be appreciated from the phase map reported in Figure 7.4. This ability to control the pattern of the refractive index by directly imprinting it into the glass adds flexibility to the writing technique. Indeed, the results reported in this section have been further developed within our group, leading to the demonstration of a symmetric waveguide fabricated in Bi_2O_3-based glass by femtosecond direct writing [108].

7.3 Chalcogenide glass

Gallium lanthanum sulphide (Ga:La:S) optical glass is an interesting material for both fiber and planar technologies, as it offers possibilities for a wide array of devices suitable for use in both non-linear applications and as IR lasers [109]. Typically, the transmission window for Ga:La:S-based glasses extends from 1 μm to longer infrared wavelengths, as compared with common oxide glasses. The high-refractive index, high non-linearity, excellent rare-earth solubility, and an ability to exhibit localized material changes (reversible or irreversible) when irradiated with light, suggest that Ga:La:S glasses are

SAMPLE MKAM				
E$_p$ (μJ)	**MKAM10**	**$\Delta\phi$ (rad)**	**MKAM50**	**$\Delta\phi$ (rad)**
2.25 μJ	MKAM10$_{10}$	1.5 ± 0.1		
2.00 μJ	MKAM10$_9$	1.3 ± 0.1		
1.75 μJ	MKAM10$_8$	1.4 ± 0.1		
1.50 μJ	MKAM10$_7$	1.1 ± 0.1		
1.25 μJ	MKAM10$_6$	1.1 ± 0.1	MKAM50$_6$	4.0 ± 0.1
1.00 μJ	MKAM10$_5$	0.9 ± 0.1	MKAM50$_5$	3.0 ± 0.1
0.75 μJ	MKAM10$_4$	1.0 ± 0.1	MKAM50$_4$	2.1 ± 0.1
0.50 μJ	MKAM10$_3$	0.7 ± 0.1	MKAM50$_3$	1.1 ± 0.1
0.25 μJ	MKAM10$_2$	0.3 ± 0.1	MKAM50$_2$	1.1 ± 0.1
0.10 μJ	MKAM10$_1$	n.a.	MKAM50$_1$	0.6 ± 0.1

TABLE 7.4: Fabrication details of the sample MKAM, written in Ga:La:S glass with the setup described in Section 3.1, with $\lambda_w = 800\,nm$, $r = 100\,kHz$, $\tau \sim 200\,fs$, $s_s = 80\,\mu m/s$. The laser was focused via the 10x (50x) objective for the fabrication of the squares of MKAM10 (MKAM50) and linearly polarized.

indeed interesting candidates for optical waveguide development [11]. A homemade (Ga:La:S) glass[5], was irradiated by femtosecond pulses with the writing setup (Section 3.1, $\lambda_w = 800\,nm$ pulse duration $\sim 200\,fs$ and repetition rate $100\,kHz$). Various regions of $(100\,\mu m)^2$ were written at a constant speed of $80\,\mu m/s$ (Fig. 7.5). The energy density was varied from one region to the other, changing either the focusing objective or the energy level (Tab. 7.4).

As for the bismuthate glass (Sec. 7.2), optical inspection revealed the absence of birefringence on the xy plane. The measurements of the laser-induced phase retardation (Sec. 3.2), reported in Table 7.4, show that in all the different irradiation conditions, the laser-induced a positive index change in the processed regions. The position of the squares within the block of glass enabled measurement of the dimension of the written squares in the z direction, t_p, only for the structures written in MKAM50, which

---

[5] The samples utilized for the experiments reported in this section were prepared by Dr A. K. Mairaj [110].

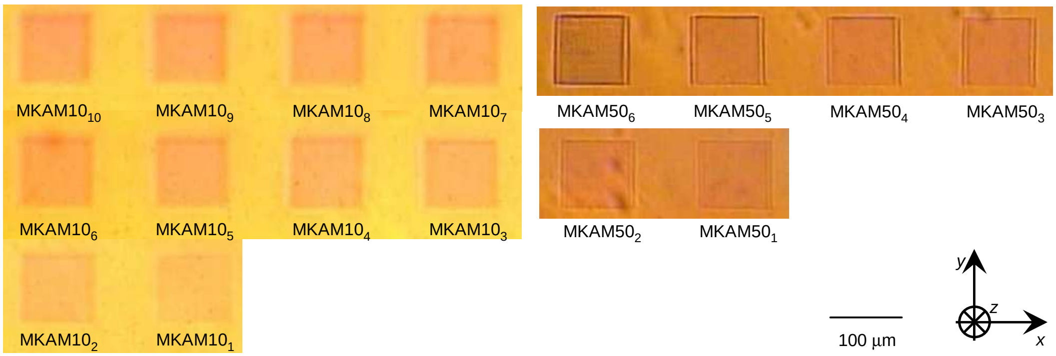

FIGURE 7.5: Microscope image of the sample MKAM (See Table 7.4 for fabrication details).

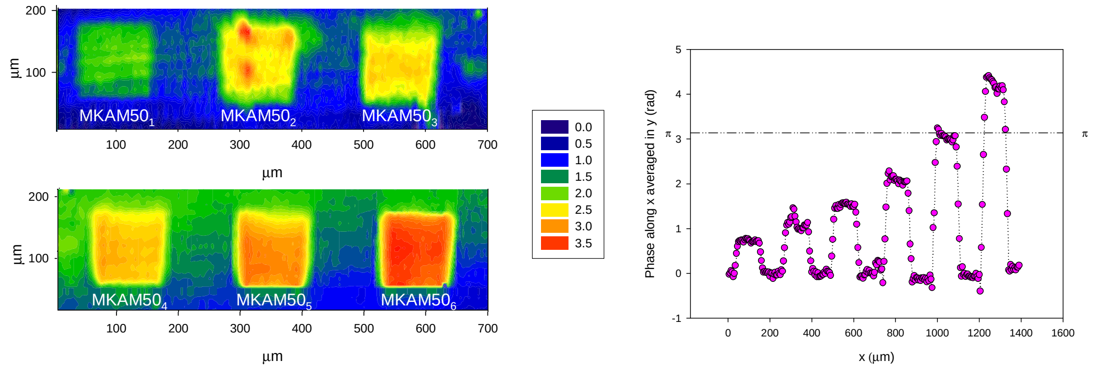

(a) (b)

FIGURE 7.6: (a): Phase map of the sample MKAM50, representing the phase retardation of the probing light traversing the sample. (b): Phase retardation along x, averaged in y and corrected to a zero background.

were closer to the end-face yz. The maximum index change is displayed in MKAM50$_6$ ($\Delta n = +5.8 \times 10^{-3}$). This result is almost six times higher than what was previously achieved by UV writing in the same material [111], where the index change was observed in the region *below* the damaged processed area. On the contrary, our analysis demonstrates that, also in this glass, the femtosecond laser increases the index change of the material within the irradiated volume (Fig. 7.6).

7.4 Sapphire crystal

Although the reduced photosensitivity requirements have encouraged testing the femtosecond direct write technique in many different glasses, the interaction between femtosecond pulsed lasers and crystals has received little attention. Study of the effects on crystals, such as sapphire, irradiated by ultrashort lasers, is attractive because of its wide applications. Indeed, sapphire is an important laser host and window material because of its excellent optical and mechanical properties.

The sample utilized for the experiment was an a-plane sapphire plate. Utilizing the writing setup (Sec. 3.1), various squares of $(100\,\mu m)^2$ were written at a constant speed of $80\,\mu m/s$ (Tab. 7.5). Figure 7.7 shows microscope images of some of the written squares. While the structures written in tighter focusing conditions ($Al_2O_3 50$) show cracks within and around the irradiated area (Fig. 7.7 (a)), the zones processed with the laser focused via the 10x objective ($Al_2O_3 10$) are devoid of fractures (Fig. 7.7 (b)). This allowed the measurement of the laser-induced retardation whose results, reported in Table 7.5, revealed a negative index change in all the measured squares. In order to verify if this finding could be justified by the onset of form birefringence, the sapphire platelet

SAMPLE Al_2O_3				
E_p (μJ)	**Al_2O_310**	**$\Delta\phi$ (rad)**	**Al_2O_350**	**$\Delta\phi$ (rad)**
2.25 μJ	$Al_2O_310_{10}$	-2.6 ± 0.2		
2.00 μJ	$Al_2O_310_9$	-2.4 ± 0.2		
1.75 μJ	$Al_2O_310_8$	-2.3 ± 0.2		
1.50 μJ	$Al_2O_310_7$	-2.1 ± 0.2		
1.25 μJ	$Al_2O_310_6$	-1.9 ± 0.2		
1.19 μJ			$Al_2O_350_6$	n.a.
1.00 μJ	$Al_2O_310_5$	-1.7 ± 0.2	$Al_2O_350_5$	n.a.
0.75 μJ	$Al_2O_310_4$	-1.6 ± 0.2	$Al_2O_350_4$	n.a.
0.50 μJ	$Al_2O_310_3$	-1.1 ± 0.2	$Al_2O_350_3$	n.a.
0.25 μJ	$Al_2O_310_2$	0.0 ± 0.2	$Al_2O_350_2$	n.a.
0.10 μJ	$Al_2O_310_1$	0.0 ± 0.2	$Al_2O_350_1$	n.a.

Table 7.5: Fabrication details of the sample Al_2O_3, written in sapphire crystal with the setup described in Section 3.1, with $\lambda_w = 800\,nm$, $r = 100\,kHz$, $\tau \sim 200\,fs$, $s_s = 80\,\mu m/s$. The laser was focused via the 10x (50x) objective for the fabrication of the squares of Al_2O_310 (Al_2O_350) and linearly polarized. The table also reports the measurement of the phase retardation induced in the written squares.

containing the squares of Al_2O_310 was positioned between cross polarizers (Fig. 7.7 (c)). In this sample, birefringence could only be detected *around* the written structures, but not *within* the squares, suggesting that the decrease of the index change might be due to amorphization of the crystal structure rather than the onset of form birefringence. These results found confirmation in a recent paper reporting waveguiding of light in Ti^{3+}: sapphire crystal in the regions *surrounding* the irradiated material [52].

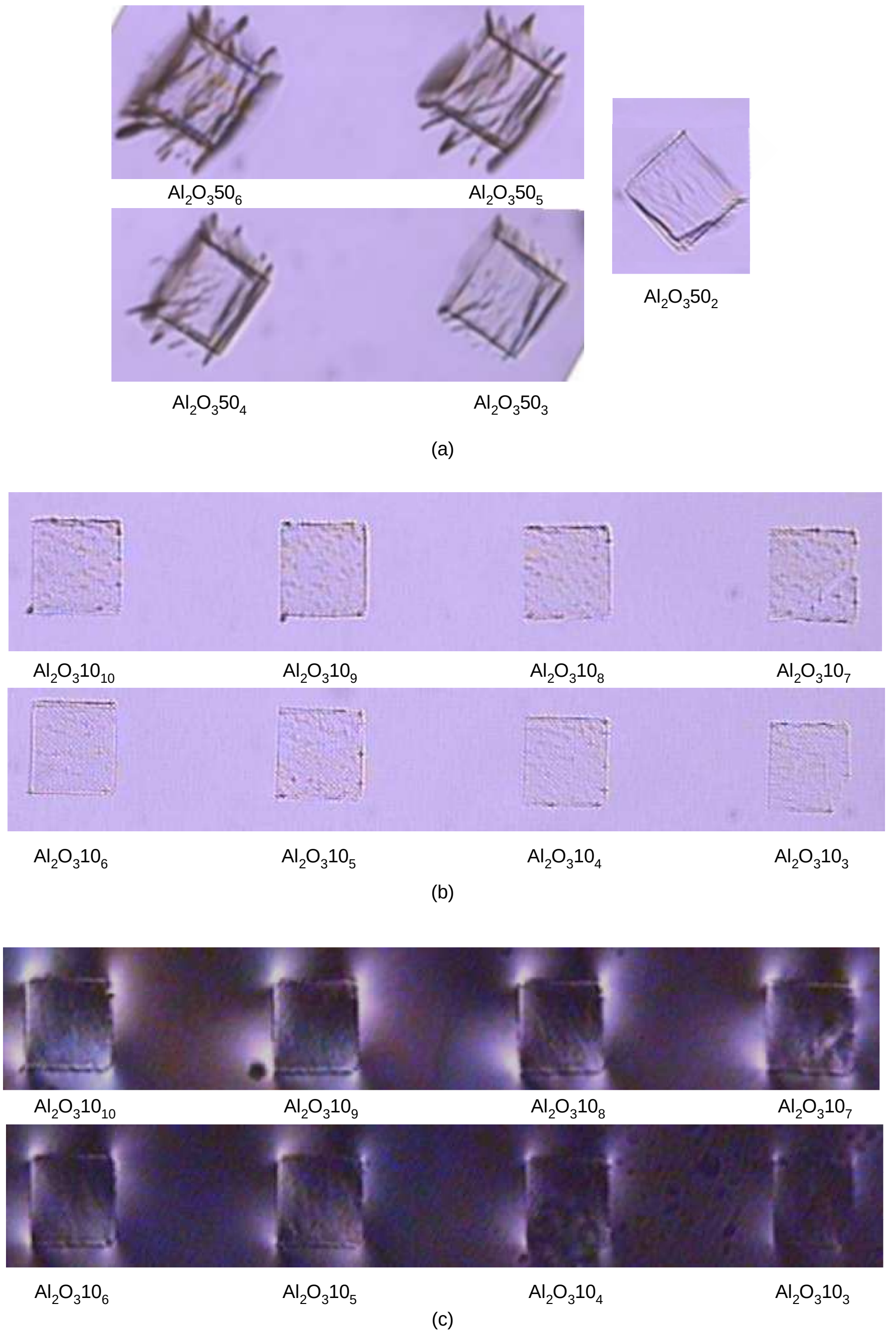

FIGURE 7.7: Microscope images of the sample Al_2O_3. (a) Al_2O_350. (b) Al_2O_310. (c) Al_2O_310 between cross polarizers.

7.5 Search for self-assembled nanostructures in some silicate glasses

The results presented in the previous sections showed that it was not possible to find an energy threshold for birefringence in any of the investigated materials. This suggests that in the various irradiation conditions tested on the samples, no self-assembled form birefringence was formed in the processed area (with the exception of the silica reference sample of Section 7.1). These results imply that the creation of anisotropic structures during the irradiation with femtosecond pulses is a phenomenon highly dependent on the processed material.

We therefore investigated more transparent materials in an attempt to reproduce the results achieved in silica, where periodic sub-wavelength structures have been observed. In particular, we studied the sign of the laser-induced index change, and the appearance of laser-induced birefringence in some silicate glasses (soda-lime, borosilicate and lead silicate glass). In each sample various squares were written at a constant speed of $80\,\mu m/s$ utilizing the setup of Section 3.1 ($\lambda_w = 800\,nm$, $\tau \sim 200\,fs$, and $r = 100\,kHz$). The energy levels and focusing conditions utilized to irradiate the samples are specified in Table 7.7. After writing, the samples were optically inspected to verify the presence of birefringence (Sec. 3.3) and finally, the laser-induced index change was measured (Sec. 3.2).

When inspected between cross polarizers, none of these samples showed an appreciable birefringence within the irradiated region. Furthermore, the measurement of the laser-induced phase retardation, presented in Table 7.5, demonstrated that almost all the written squares showed a positive laser index change. The only exception was found in some structures of the borosilcate sample, namely in $\mathrm{BFS}_{1\ldots3}$, displaying a negative index change. However, even these structures were not birefringent. Table 7.6 reports some of the main parameters of the materials we investigated. Silica has the highest bandgap and the lowest density (this parameter is actually comparable with soda-lime's

Material	$\mathbf{E_g}$ **(eV)**	**Softening point (° C)**	$\mathbf{n_{bg}}$	**Density** $\times\,\mathbf{10^3}$ **(kg/m^3)**
SiO_2	9	1600	1.47	2.2
SiO_2:SnO_2 (EMF)	2.8-3.5			
Bi_2O_3 (AFW)	2.5	560	2.5	8.9
Ga:La:S (MKAM)	2.6		2.4	4.4
Sapphire	7.3	2053	1.76	4.0
Soda-lime	4.0	720	1.52	2.5
Borosilicate	3.8	736	1.52	2.7
Lead-silicate (SF57)	3.2	519	1.82	5.5

Table 7.6: Some of the principal properties of the investigated transparent materials. The value of n_{bg} is for $\lambda \sim 800\,mn$.

and borosilica's). However, since our experimental observations did not manage to find another material displaying negative index change and birefringence, it is extremely difficult to speculate which parameter may play a pivotal role in the mechanism leading to the formation of the nano-grating, highlighting that more investigations are required.

SAMPLE SF57

$\mathbf{E_p}$ **(μJ)**	**SF5710**	**$\Delta\phi$ (rad)**	**SF5750**	**$\Delta\phi$ (rad)**
2.40 μJ	$SF5710_{10}$	3.6 ± 0.1		
2.00 μJ	$SF5710_9$	3.1 ± 0.1		
1.75 μJ	$SF5710_8$	2.8 ± 0.1		
1.50 μJ	$SF5710_7$	1.8 ± 0.1		
1.33 μJ			$SF5750_7$	1.6 ± 0.1
1.25 μJ	$SF5710_6$	1.3 ± 0.1	$SF5750_6$	1.6 ± 0.1
1.00 μJ	$SF5710_5$	0.4 ± 0.1	$SF5750_5$	1.5 ± 0.1
0.75 μJ	$SF5710_4$	0.2 ± 0.1	$SF5750_4$	1.2 ± 0.1
0.50 μJ	$SF5710_3$	0.5 ± 0.1	$SF5750_3$	0.8 ± 0.1
0.25 μJ	$SF5710_2$	0.0 ± 0.1	$SF5750_2$	0.6 ± 0.1
0.10 μJ	$SF5710_1$	0.0 ± 0.1	$SF5750_1$	0.0 ± 0.1

SAMPLE SFS

$\mathbf{E_p}$ **(μJ)**	**SFS10**	**$\Delta\phi$ (rad)**	**SFS50**	**$\Delta\phi$ (rad)**
2.45 μJ	$SFS10_{10}$	0.4 ± 0.1		
2.00 μJ	$SFS10_9$	0.4 ± 0.1		
1.75 μJ	$SFS10_8$	0.4 ± 0.1		
1.50 μJ	$SFS10_7$	0.4 ± 0.1		
1.25 μJ	$SFS10_6$	0.4 ± 0.1	$SFS50_1$	0.9 ± 0.1
1.00 μJ	$SFS10_5$	0.3 ± 0.1	$SFS50_2$	0.9 ± 0.1
0.75 μJ	$SFS10_4$	0.0 ± 0.1	$SFS50_3$	0.1 ± 0.1
0.50 μJ	$SFS10_3$	0.0 ± 0.1	$SFS50_4$	0.0 ± 0.1
0.25 μJ	$SFS10_2$	0.0 ± 0.1	$SFS50_5$	0.0 ± 0.1
0.10 μJ	$SFS10_1$	0.0 ± 0.1	$SFS50_6$	0.0 ± 0.1

SAMPLE BFS

$\mathbf{E_p}$ **(μJ)**	**BFS50**	**$\Delta\phi$ (rad)**
1.25 μJ	$BFS50_6$	$+1.0 \pm 0.1$
1.00 μJ	$BFS50_5$	$+0.7 \pm 0.1$
0.75 μJ	$BFS50_4$	$+0.1 \pm 0.1$
0.50 μJ	$BFS50_3$	-0.2 ± 0.1
0.25 μJ	$BFS50_2$	-0.3 ± 0.1
0.10 μJ	$BFS50_1$	-0.1 ± 0.1

TABLE 7.7: Fabrication details of the samples SF57, SFS, and BFS written in SF57 Schott lead-silicate glass, sodalime glass, and borosilicate glass, respectively. The samples were written with the setup described in Section 3.1, with $\lambda_w = 800\,nm$, $r = 100\,kHz$, $\tau \sim 200\,fs$, $s_s = 80\,\mu m/s$. The laser was focused via the 10x or 50x objective, and linearly polarized. The table also reports the measurement of the phase retardation induced in the written squares.

7.6 Conclusions

The results presented in this chapter confirmed the ability of femtosecond lasers to easily induce a modification of the refractive index in various transparent materials. Utilizing a phase stepped interferometric technique, we measured the phase retardation of the probing light travelling through the irradiated zones,and its dependence versus the laser energy density. Indeed, in all the transparent materials considered, it was possible to achieve a modification of the refractive index. In particular, in Ga:La:S and Bi_2O_3 glass an index change almost one order of magnitude higher than that achieved with a UV laser in the same glasses was demonstrated. In addition, it was shown that the ability to modify the refractive index of the material extends also to crystals.

However, our observations showed that the characteristics of the modified regions are highly dependent on the material. As was discussed in the previous chapters, in silica glass it was found that above a certain intensity threshold the formation of a subwavelength periodic structures in the irradiated regions gives rise to form birefringence, negative index change and anisotropic reflection. This characteristic has not been reproduced in any of the other tested material. Actually, even in the glass-ceramic described in Section 7.1, the ability to tune the sign of the index change according to the laser intensity was demonstrated. Nevertheless, in this case, the presence of SnO_2 nanoclusters grown in silica, dramatically affects the interaction between the femtosecond laser pulse and the material, consequently, the change of the sign of the laser modified refractive index was ascribed to a new mechanism involving the competitive effects of amorphization of the clusters and compression of the surrounding glass. Finally, the absence of an intensity birefringence threshold in all the investigated materials made it particularly difficult to identify the key parameter involved in the formation of the nano-grating, a mechanism still largely not understood and in need of more investigation.

Chapter 8

Conclusions and future work

8.1 Summary and discussion

In this thesis we have reported novel developments in the field of femtosecond micromachining within the bulk of transparent materials. We started researching this field as there were not studies conducted on the ability of femtosecond lasers to fabricate diffractive optical components in the bulk of a dielectric material. These are necessary components for the realization of monolithic optical devices. Moreover, the few reports on the measurement of the laser-induced index change were contradictory. Clearly, without the knowledge of this fundamental parameter, the design of embedded optical components could not be achieved, thus providing a strong motivation to examine the possible parameters in the femtosecond irradiation regime and for a range of interesting materials. Finally, as the interaction between ultrashort laser pulses and transparent dielectric materials was a new research topic, its fundamental mechanisms were largely unknown. A better understanding of the fundamentals is essential for an efficient use of this writing technique. The work carried out during my doctorate, and presented in this manuscript, has contributed to the development of each of these investigation topics. Precisely, our major breakthroughs consisted of:

- The first demonstration of femtosecond directly written diffractive optic devices (Fresnel zone plates) embedded in a silica substrate. Both the focusing properties and efficiencies of the devices compared well with the theoretical values (Chapter 4).
- The observation and characterization of a new class of structures created by femtosecond irradiation of silica glass (type II-fs), characterized by a spectrally selective reflection occurring only in the direction of the electric field of the writing laser, negative index change, birefringence, and extraordinary stability towards the temperature increase (Chapter 5).

- The discovery of the formation of self-assembled periodic sub-wavelength structures created during the irradiation process in silica glass, theoretically explained in Chapter 5 and experimentally observed in Chapter 6.
- The development of a practical tool to measure the laser-induced index change, which was utilized to investigate the behaviour of various transparent materials when irradiated by the femtosecond laser over a range of operating conditions (Chapter 7).

The progress made in these last few years have encouraged a few companies to introduced complete femtosecond laser processing systems, but these systems are still at a research and development stage, rather than realized product lines. The two principal impediments to the widespread use of femtosecond lasers in industrial processing environments are repetition rate and ruggedness. Typical amplified femtosecond lasers operate at $1\,kHz$, which makes high-speed processing impossible. However, CW-pumped amplified femtosecond lasers, operating in the $100\,kHz$ range, already produce $6\,mJ$ per pulse (and higher energy prototypes exist), which is adequate for the realization of a few parallel lines. In addition, as more applications are recognized for which femtosecond lasers offer unique advantages, they will become common place in industry as well as academia. To our knowledge, in fact, no other technique holds the potential to realize three-dimensional multi-component photonic devices, fabricated in one single step in a variety of transparent materials. While laser manufacturers work to make femtosecond systems cheaper, robust and turnkey, academia will continue investigate the femtosecond writing technique and the underlying physical processes.

8.2 Future work

We believe that the results presented in this thesis represent a major step forward in the study of femtosecond laser induced modification of the irradiated materials, however, the vastness of this subject leaves several areas for future researches to investigate. Some of the most immediate topic areas to be tackled are discussed here.

8.2.1 Development and optimization of Fresnel zone device-based components

The natural evolution of the work presented in Chapter 4, where efficient Fresnel zone plates were demonstrated, is the generalization of the fabrication method to other Fresnel zone devices characterized by a higher focusing efficiency. Indeed, our results have already inspired the realization of MFZPs by femtosecond direct writing [112]. Using the characterization data that we have provided on laser-induced phase retardation, efficient single MFZPs and arrays can now be realized in all the transparent materials investigated in Chapter 7.

Furthermore, we are designing a device, which will allow the mode conversion of the incident beam from Hermite-Gaussian (HG) to Laguerre-Gaussian (LG). LG modes are laser beams carrying orbital momentum, which are extremely interesting as they could be used as optical tweezers or spanners [113]. Although LG modes have been produced directly in laser systems [114], they are more easily produced by the conversion of HG beams (the most common intensity distribution of laser resonators). The mode converter that we are investigating, has been already demonstrated utilizing bulk optics [115], and comprises three focusing devices. Exploiting the ability of the femtosecond technique to write lenses in the bulk of the material, we are planning to integrate the device into a single and compact block.

8.2.2 Development of photonic devices based on the femtosecond written structures of type II-fs

In Chapter 5, it was demonstrated that, in silica glass, it is possible to create a class of written structure (type II-fs) characterized by negative index change, anisotropic reflection, birefringence, and thermal stability. As we have shown, these properties are a consequence of the formation of a self-assembled periodic structure within the irradiated volume. Owing to their unique characteristics, the femtosecond structures of type II-fs can find useful applications in the realization of numerous devices.

In Section 5.5, femtosecond directly written retardation plates have already been demonstrated in principle, however an optimization of their parameters is still required. The magnitude of the birefringence can be controlled by the intensity of the writing beam and the exposure time, while the thickness of the modified structures can be increased by writing more layers in the bulk of the material. In Section 5.2, we have also seen that the anisotropic properties of the structures of type II-fs can be utilized for the realization of micro-reflectors. These devices may well have a principal role in routing of lasers beams in optical integrated circuits. Furthermore, given their directional reflection characteristic, i.e. only along the direction of polarization of the writing beam, they could find useful applications in dense optical memories. However, the optimization of the micro-reflectors requires more investigation of the characteristics of the self-assembled nano-grating, and their dependence on the laser parameters (Sec. 8.2.3).

Retardation plates and reflectors are only two of the possible applications of this novel type of directly written structure. For instance, exploiting their spatial coherence (Sec. 6.3), the self-assembled periodic structures could be directly utilized for the creation of band-gap guiding devices in two or three dimensions.

Amongst the materials investigated in Chapter 7, only silica glass was observed to display the structures of type II-fs , hence at the time it was the only host for the development of the aforementioned devices. In fact, very recently, self-assembled sub-wavelength periodic structures produced by a femtosecond laser have also been observed in a TeO_2 crystal [116]. Further investigation of the common properties between these media is required to determine which other materials have suitable characteristics for type II-fs photonic structures.

8.2.3 Experimental characterization of the nano-gratings

The experimental observations, presented in Chapter 6, left a number of open questions which were beyond the scope of this work, yet should be addressed to enable a better understanding of the mechanisms responsible for the formation of the sub-wavelength periodic structures, and consequently how to efficiently exploit them (Sec. 8.2.2). In particular, it was shown that the sub-wavelength periodic assembly, created in the irradiated volume, displayed an asymmetric periodicity ($f_f \neq 0.5$). The nature of this characteristic is still unexplained. While our observation reveals a filling factor, f_f, of 0.3, the data reported in [91] demonstrated $f_f = 0.1$. The identification of the parameter affecting f_f may help the understanding of why the grating is not balanced and how to control the filling factor value.

Another unsolved issue is the presence of a tilt of the periodic arrangement, appearing in the tail of the written structures, with respect to the direction of the propagation of the writing laser (Fig. 6.4). We have already conducted some preliminary investigations, which seem to suggest that the tilt appears only when the writing light is tightly focused. However, this results is in disagreement with the recent observations presented in [98] and needs to be further investigated.

Finally, the dependence of the of the nano-grating period as a function of the laser parameters should be explored.

8.2.4 Modelling of the femtosecond writing technique

As mentioned in Chapter 2, a complete model of the interaction of femtosecond laser pulses that are focused in the bulk of transparent materials has not yet been solved. The groups working in this field are currently faced with the computational difficulties presented when attempting to solve the propagation equation for ultra-short pulses in a highly non-linear regime, where the paraxial approximation is no more valid.

To complicate the mathematical problem even further, the novel results presented in this thesis (Chap. 6) suggest that there is another physical mechanism that needs to be considered. Our experimental observations suggest that, in fact, in silica glass the interaction between the writing electromagnetic wave and the generated longitudinal plasma waves initiate a modulation of the plasma distribution. Ultimately, this is thought to cause the observed periodic structure of the refractive index with dimensions smaller than the irradiating laser wavelength. Indeed, it would be extremely interesting to include this interaction in the current theoretical modelling of the femtosecond writing technique, and will on its own be the basis for a doctoral thesis. Therefore, it is expected that results from modelling this effect, combined with additional characterization data (Sec. 8.2.3), will give a better insight into the physical mechanisms involved under femtosecond pulse irradiation, and it will also assist in enabling efficient design strategies to be developed for future devices based on *the most fascinating self-assembled periodic structures ever created by light*.

Appendix A

Waves in plasma

In this appendix, the necessary definitions related to a plasma are given and the type of waves supported by a plasma with no static magnetic field are discussed. An exhaustive discussion on plasma physics can be found in [96, 117].

A plasma is a fully or partially ionized gas in which electromagnetic interaction between the charged particles plays an essential role. In a plasma the **E** and **H** fields are not prescribed but are determined by the positions and motions of the charges themselves. Fortunately, in most of the cases the plasma can be modelled as composed of fluids, neglecting the identity of individual particles and considering only the fluid movements. An important parameter to describe a plasma is the Debye length, λ_D, representing the distance beyond which the potential of an individual charge is shielded by surrounding mobile charges

$$\lambda_D = \sqrt{\frac{\varepsilon_0 k_B T_e}{e^2 \rho}}, \tag{A.1}$$

where k_B is Boltzman constant and T_e is the electron temperature. On a spatial scale shorter than λ_D, the presence and effects of individual charges are evident. On a scale larger than λ_D, charged particle interactions tend to occur through collective motion. The Debye length of typical plasmas can be found in Figure A.1, where it can be noticed that the Debye length of plasmas generated by lasers ranges from several nanometers to several micrometers.

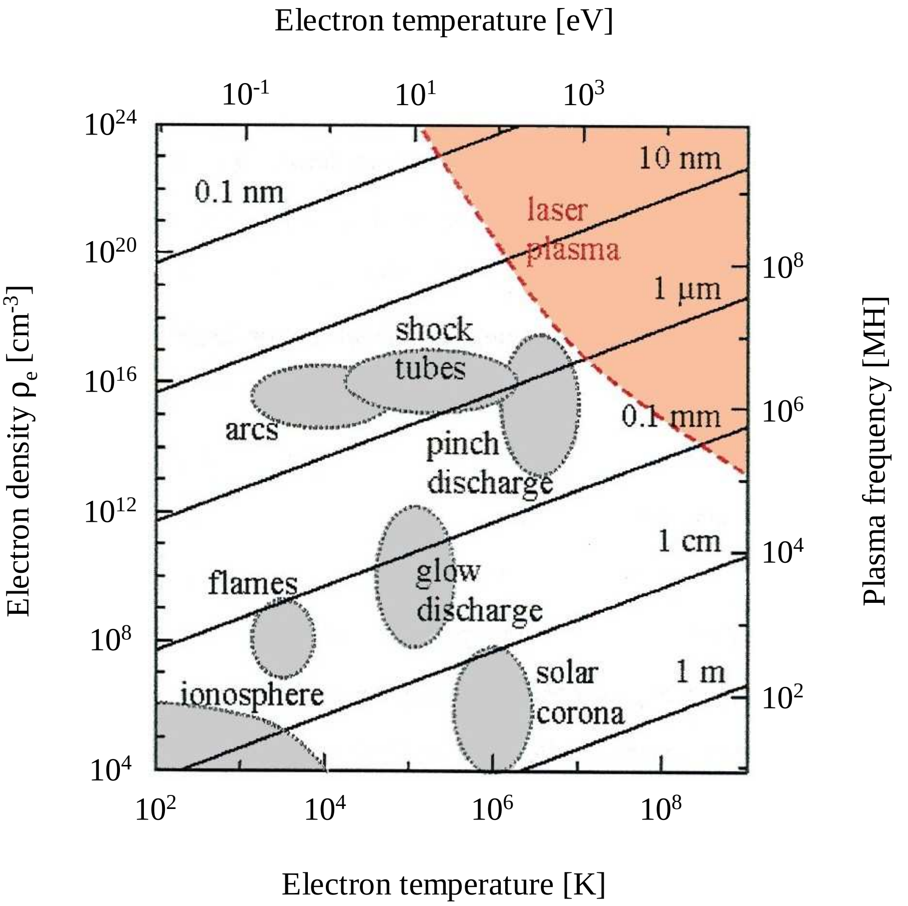

FIGURE A.1: Various types of plasma in nature. The tilted lines in the contour plot denote the Debye length λ_D [118].

A.1 The complete set of fluid equations

The set of equations whose solution gives a set of self-consistent fields and fluids motion in plasma, under the fluid approximation, is given by: Maxwell's equations (2.1), the equations of motion (A.2), the continuity equations (A.3), and the state equations (A.4) or (A.5) [117]. Maxwell's equations tells us what **E** and **H** are for a given state of the plasma. To solve the self-consistent problem, we must also have an equation giving the plasma's response to given **E** and **H**. In the fluid approximation, we consider the plasma to be composed of two interpenetrating fluids. We shall need two equations of motion, one for the positively charged ions and one for the electrons

$$m_i\rho_i\left[\frac{\partial \mathbf{v_i}}{\partial t}+(\mathbf{v_i}\cdot\nabla)\mathbf{v_i}\right]=+e\rho_i(\mathbf{E}+\mathbf{v_i}\times\mathbf{B})-\nabla p_i, \tag{A.2a}$$

$$m_e\rho_e\left[\frac{\partial \mathbf{v_e}}{\partial t}+(\mathbf{v_e}\cdot\nabla)\mathbf{v_e}\right]=-e\rho_e(\mathbf{E}+\mathbf{v_e}\times\mathbf{B})-\nabla p_e, \tag{A.2b}$$

where ρ_i (ρ_e) is the density of ions (electrons), p_i (p_e) is the ion (electron) pressure, and $\mathbf{v_i}$, ($\mathbf{v_e}$) the average fluid velocity of the ions (electrons). The conservation of matter requires that the total number of particles in a volume can change only if there is a net flux of particles across the surface bounding the volume

$$\frac{\partial \rho_i}{\partial t} + \nabla \cdot \rho_i \mathbf{v_i} = 0, \tag{A.3a}$$

$$\frac{\partial \rho_e}{\partial t} + \nabla \cdot \rho_e \mathbf{v_e} = 0. \tag{A.3b}$$

Two more relations are needed to close the system. Assuming that the electron plasma obeys to the ideal gas law, and that the compression is adiabatic (i.e. a compression without extraction of heat, resulting in increased temperature)

$$\nabla p_i = 3k_B T_i \nabla \rho, \tag{A.4a}$$

$$\nabla p_e = 3k_B T_e \nabla \rho. \tag{A.4b}$$

On the contrary, for isothermal compressions (i.e. a compression where the temperature of the ions and electron remains constant)

$$\nabla p_i = k_B T_i \nabla \rho, \tag{A.5a}$$

$$\nabla p_e = k_B T_e \nabla \rho. \tag{A.5b}$$

Assuming that the amplitude of oscillations is small, equations (2.1), (A.2), (A.3), (A.4) and (A.5) can be solved by the procedure of linearization, where the terms containing higher powers of amplitude can be neglected [117]. Solving the equations, the dependent variables will be separated into two parts: an “equilibrium” part indicated by a subscript 0, and a “perturbation” part indicated by a subscript 1. Finally, it is assumed that there is no static magnetic field.

A.2 Plasma oscillations

If electrons in a plasma are displaced from a uniform background of ions, electric fields will build up to restore the neutrality of the plasma by pulling the electrons back to their original positions. The electrons will oscillate around their equilibrium positions with a characteristic frequency (*plasma frequency*). The expression for this frequency can be derived in a simplified case [117], assuming

1. There are no thermal motions ($\nabla p = 0$).
2. The ions are fixed in space in a uniform distribution ($\mathbf{v_i} = 0$).
3. The electron motion occurs in one direction only (x).

In this case, Maxwell's equation (2.1c), the electron equations of motion (A.2b) and continuity are (A.3b)

$$\nabla \cdot \mathbf{E} = \frac{e(\rho_i - \rho_e)}{\varepsilon_0}, \tag{A.6}$$

$$m_e \rho_e \left[\frac{\partial \mathbf{v_e}}{\partial t} + (\mathbf{v_e} \cdot \nabla)\mathbf{v_e} \right] = -e\rho_e \mathbf{E}, \tag{A.7}$$

$$\frac{\partial \rho_e}{\partial t} + \nabla \cdot \rho_e \mathbf{v_e} = 0. \tag{A.8}$$

At equilibrium there are no oscillations, hence

$$\nabla \rho_0 = \mathbf{v_0} = \mathbf{E_0} = 0, \tag{A.9}$$

$$\frac{\partial \rho_0}{\partial t} = \frac{\partial \mathbf{v_0}}{\partial t} = \frac{\partial \mathbf{E_0}}{\partial t} = 0. \tag{A.10}$$

Applying the linearization, Equations (2.1c), (A.2b), and (A.3b) now become

$$\nabla \cdot \mathbf{E_1} = -\frac{e\rho_1}{\varepsilon_0}, \tag{A.11}$$

$$m_e \left[\frac{\partial \mathbf{v_1}}{\partial t} \right] = -e\mathbf{E_1}, \tag{A.12}$$

$$\frac{\partial \rho_1}{\partial t} + \rho_0 \nabla \cdot \mathbf{v_1} = 0. \tag{A.13}$$

The oscillating quantities are assumed to behave sinusoidally

$$\mathbf{E_1} = E_1 e^{i(kx - \omega t)} \hat{\mathbf{x}}, \tag{A.14a}$$

$$\rho_1 = \rho_1 e^{i(kx - \omega t)}, \tag{A.14b}$$

$$\mathbf{v_1} = v_1 e^{i(kx - \omega t)} \hat{\mathbf{x}}. \tag{A.14c}$$

Therefore time derivative can be replaced by $-i\omega$ and the spatial derivative by ik

$$0 + ikE_1 + \frac{e}{\varepsilon_0}\rho_1 = 0, \tag{A.15}$$

$$-im_e \omega v_1 + eE_1 + 0 = 0, \tag{A.16}$$

$$+ik\rho_0 v_1 + 0 - i\omega \rho_1 = 0. \tag{A.17}$$

The non-trivial solutions of this system are found imposing the determinant to be zero

$$-m_e \omega^2 k + k\rho_0 \frac{e^2}{\varepsilon_0} = 0, \tag{A.18}$$

hence we must have

$$\omega = \sqrt{\frac{\rho e^2}{\varepsilon_0 m_e}} = \omega_p. \tag{A.19}$$

The plasma frequency, ω_p, is the frequency for collective oscillations of the electrons about their equilibrium position. This oscillation is so fast that the massive ions do not have time to respond to the oscillating field and may be considered as fixed. Equation A.19 tells us that the frequency of plasma oscillations depends only on the electron density. In particular, ω does not depend on k, hence the disturbance does not propagate.

A.2.1 Electron plasma waves or Langmuir waves

In the previous section we have seen that plasma oscillations do not propagate. The equation describing the motions of the electrons was solved in absence of thermal motions. When this effect is taken into account, the pressure force to the right hand side of (A.2b) cannot be neglected. This force arises from the random motion of particles in and out a small volume of plasma. Applying the linearization [117], Equations (2.1c), (A.2b), and (A.3b) now become

$$\nabla \cdot \mathbf{E_1} = -\frac{e\rho_1}{\varepsilon_0}, \tag{A.20}$$

$$m_e\rho_0 \left[\frac{\partial \mathbf{v_1}}{\partial t}\right] = -e\rho_0\mathbf{E_1} - 3k_BT_e\frac{\partial \rho_1}{\partial x}, \tag{A.21}$$

$$\frac{\partial \rho_1}{\partial t} + \rho_0\nabla \cdot \mathbf{v_1} = 0. \tag{A.22}$$

Using Equation A.14, we obtain

$$0 + ikE_1 + \frac{e}{\varepsilon_0}\rho_1 = 0, \tag{A.23}$$

$$-im_e\omega\rho_0v_1 + e\rho_0E_1 + i3kk_BT_e\rho_1 = 0, \tag{A.24}$$

$$+ik\rho_0v_1 + 0 - i\omega\rho_1 = 0. \tag{A.25}$$

This linear homogenous system has non-trivial solutions if its determinant is equal to zero

$$-3k^2k_BT_e + \omega^2me_e - \rho_0\frac{e^2}{\epsilon_0}. \tag{A.26}$$

Hence, the dispersion relationship for the electron plasma wave is as follows

$$\omega^2 = \omega_p^2 + \frac{3}{2}v_e^2k^2, \tag{A.27}$$

where $v_e^2 = (2k_BT_e/m_e)$ is the thermal speed of electrons. In (A.27) the frequency depends on k, hence electron plasma waves propagate in the direction of the electric field.

A.2.2 Ion acoustic waves

Ion acoustic waves in plasma are similar to ordinary acoustic sound waves in neutral gas: they are longitudinal waves consisting of compression and rarefaction progressing in the medium. Unlike sound waves, ion acoustic waves can also propagate through collisionless medium, because the charged ions interact at long distances via their electromagnetic field. A second difference is that plasma contains electrons which affect the wave dispersion equation. Due to their small mass the electrons are very mobile and they quickly follow the ion motion trying to preserve charge neutrality. The electron motion is caused by a small electric field internally generated by the plasma as a result of variations in the local density ($\mathbf{B} = \mathbf{0}$). The equation of motion of the ions (A.2a) becomes

$$m_i \rho_i \left[\frac{\partial \mathbf{v_i}}{\partial t} + (\mathbf{v_i} \cdot \nabla)\mathbf{v_i} \right] = e\rho_i \mathbf{E} - \nabla p_i. \tag{A.28}$$

Charge neutrality is preserved if $\rho_i = \rho_e = \rho$, which can only be accomplished when $\mathbf{v_i} = \mathbf{v_e} = \mathbf{v}$. Then the momentum equations (A.2) give

$$\frac{e\rho \mathbf{E} - \nabla p_i}{m_i} = -\frac{e\rho \mathbf{E} + \nabla p_e}{m_e}, \tag{A.29}$$

which can be solved to obtain the electric field

$$\mathbf{E} = \frac{m_e \nabla p_i - m_i \nabla p_e}{e\rho(m_i + m_e)} \sim -\frac{\nabla p_e}{e\rho}. \tag{A.30}$$

This approximation is valid because the electron mass is much smaller than the ion mass. Equation A.28 can now be written as:

$$m_i \rho \left[\frac{\partial \mathbf{v}}{\partial t} + (\mathbf{v} \cdot \nabla)\mathbf{v} \right] = -\nabla p_i - \nabla p_e. \tag{A.31}$$

In the previous section, the electron compression has been assumed adiabatic. However, on a time scale where the massive ion movement becomes important, the electrons are expected to move fast enough to equalize the electron temperature. In this case, their compression becomes (A.5b) isothermal and the equation of movements of the ions becomes

$$m_i \rho \left[\frac{\partial \mathbf{v}}{\partial t} + (\mathbf{v} \cdot \nabla)\mathbf{v} \right] = -k_B(3T_i + T_e)\nabla \rho. \tag{A.32}$$

Using (A.14), and linearizing, (A.32), and (A.3a) become

$$m_i \omega \rho_0 v_1 + k k_B (3T_i + T_e)\rho_1 = 0, \tag{A.33}$$

$$k\rho_0 v_1 - \omega \rho_1 = 0. \tag{A.34}$$

Again, this system has non-trivial solutions only if its determinant is zero which leads to the dispersion relationship for ion acoustic waves

$$\omega = \sqrt{\frac{k_B(3T_i + T_e)}{m_i}} k. \tag{A.35}$$

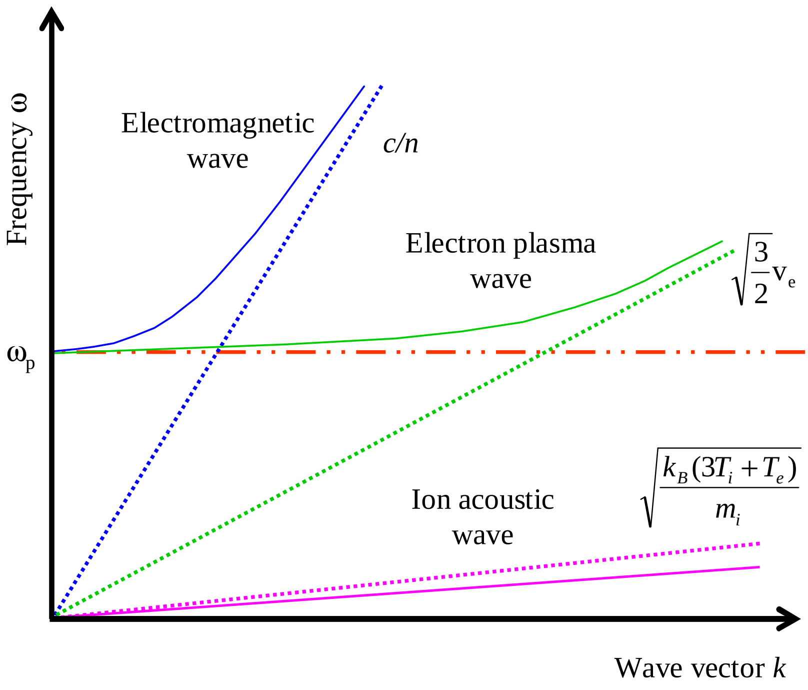

Figure A.2: Dispersion diagram for naturally occurring waves in an plasma [119].

This equation also shows that the phase velocity of the ions $v_+ = \sqrt{\frac{k_B(3T_i+T_e)}{m_i}}$ is much smaller than the phase velocity of electrons $v_e = \sqrt{2k_BT_e/m_e}$, thus confirming the assumption that the electrons are fast enough to equalize their temperature.

A.2.3 Electromagnetic waves in plasma

The dispersion equation of electromagnetic waves in vacuum ($\omega = ck$) is obtained combining (2.1a), and (2.1b), with $\mathbf{j} = 0$, and assuming $\exp\left[i(\mathbf{k}\cdot\mathbf{r} - \omega t)\right]$ dependence. In a plasma, the term accounting for the currents due to charged particle motions in (2.1b) modifies the dispersion equation. Indeed, combining (2.1a), and (2.1b) we obtain

$$(\omega^2 - c^2k^2)\mathbf{E} = -i\frac{\omega}{\varepsilon_0}\mathbf{j}. \tag{A.36}$$

At optical frequencies the the ions can be considered fixed and the current $\mathbf{j}$ comes entirely from electron motion

$$\mathbf{j} = -e\rho_0\mathbf{v_e}. \tag{A.37}$$

Using the linearized equation of motion (A.16) we have

$$(\omega^2 - c^2k^2)\mathbf{E} = \frac{e^2\rho_0}{\varepsilon_0 m_e}\mathbf{E}, \tag{A.38}$$

hence

$$\omega^2 = \omega_p^2 + c^2k^2. \tag{A.39}$$

This is the dispersion relationship for electromagnetic waves propagating in a plasma with no static magnetic field. We see that the vacuum relations is modified by a term ω_p^2 reminiscent of plasma oscillations. A dispersion relation like (A.39) exhibits a phenomenon called *cutoff* (Fig. A.2). If one sends an electromagnetic wave with a given frequency ω, the wavelength $2\pi/k$ in the plasma will take on the value prescribed by the dispersion relationship. As the plasma density, and hence ω_p^2, is raised, k^2 will necessarily decrease. Finally, an electron density will be reached such that k^2 is zero. For densities larger than this the wave cannot propagate. This cutoff condition occurs at a critical density ρ_c such as $\omega = \omega_p$; namely

$$\rho_c = \frac{m_e \omega^2 \varepsilon_0}{e^2}, \tag{A.40}$$

which, at $800\,nm$ the critical density of plasma is $\rho_c = 1.74 \times 10^{21}\,cm^{-3}$.

Appendix B

Propagation of light in an optically anisotropic material

This appendix has been included to clarify the notation utilized throughout the thesis when referring to laser-induced form birefringence. Section B.1 reviews the geometrical construction utilized to determine the velocities of propagation and the polarization for electromagnetic waves in anisotropic materials. Section B.2 details an expression, which describes the polarization state of a monochromatic wave after traversing a birefringent plate. Finally, Section B.3 describes the concept of *form birefringence* which is a type of anisotropy the reader may not be familiar with and which we believe plays a key role in ultrashort micro-machining. An exhaustive discussion on birefringence can be found in [93].

B.1 The ellipsoid of the wave normal

Optically anisotropic materials are defined as substances whose electrical excitations depend upon the direction of the electric field. In general, the displacement vector **D** will no longer be aligned to the direction of the vector **E**. Assuming that the **E** and **D** are linearly related,

$$\mathbf{D} = \overline{\varepsilon}\,\mathbf{E}, \tag{B.1}$$

with

$$\overline{\varepsilon} = \begin{bmatrix} \varepsilon_{xx} & \varepsilon_{xy} & \varepsilon_{xz} \\ \varepsilon_{xy} & \varepsilon_{yy} & \varepsilon_{yz} \\ \varepsilon_{xz} & \varepsilon_{yz} & \varepsilon_{zz} \end{bmatrix}. \tag{B.2}$$

In the system of coordinate of the principal dielectric axes $\overline{\varepsilon}$ becomes a diagonal matrix, whose elements ε_x, ε_y, ε_z are defined as the principle dielectric constants. It may be seen immediately from these formulae that **D** and **E** will have different directions, unless **E** coincides in direction with one of the principal axes, or the principal dielectric constants are all equal.

It can be demonstrated that an anisotropic medium permits two monochromatic plane waves with two different linear polarization (and two different phase velocities) to propagate in any given direction [93]. From the Fresnel equation of the wave normal

$$\frac{s_x^2}{v_p^2 - v_x^2} + \frac{s_y^2}{v_p^2 - v_y^2} + \frac{s_z^2}{v_p^2 - v_z^2} = 0, \tag{B.3}$$

one can see that for every direction $\hat{\mathbf{s}}$ of propagation ($|\hat{\mathbf{s}}| = 1$) there correspond two phase velocities v_p' and v_p''. The phase velocities of waves which are propagated in the direction of the principal axes are equal to

$$v_x = \frac{c}{n_x}, \quad v_y = \frac{c}{n_y}, \quad v_z = \frac{c}{n_z}, \tag{B.4}$$

where c is the speed of light $n_x = \sqrt{\varepsilon_x}$, $n_y = \sqrt{\varepsilon_y}$, and $n_z = \sqrt{\varepsilon_z}$. In all the other cases, the two phase velocities and the perpendicular directions of the two vector $\mathbf{D}$ corresponding to a given propagation direction $\hat{\mathbf{s}}$ can be graphically found from what is know as *ellipsoid of wave normal*, or the *index ellipsoid.* The index ellipsoid is the surface described by the components of the vector $\mathbf{D}$ which indeed satisfy the relation

$$\frac{D_x^2}{\varepsilon_x} + \frac{D_y^2}{\varepsilon_y} + \frac{D_z^2}{\varepsilon_z} = \text{Constant}, \tag{B.5}$$

Equation B.5 represents an ellipsoid, the semi-axes of which are equal to the square roots of the principal dielectric constants and coincide in direction with the principal dielectric axes.

The intersection of a plane through the origin of the ellipsoid and perpendicular to $\hat{\mathbf{s}}$ is an ellipse (Fig. B.1 (a)); the principal semi-axes of this curve are proportional to $1/v_p$ and their directions coincide with the corresponding directions of the vector $\mathbf{D}$. For any ellipsoid, the intersected curve is a circle only for two directions of propagation. These directions are defined as *optic axes*, and they are characterized by the fact that there is only one velocity of propagation along them and $\mathbf{D}$ can take any direction perpendicular to $\hat{\mathbf{s}}$.

When the axes of the ellipsoid all have unequal length, the material has two optical axes and is therefore defined as *biaxial.* When all the axes have the same length, the ellipsoid degenerates to a sphere with infinite possible optic axes. In this case $\varepsilon_x = \varepsilon_y = \varepsilon_z = \varepsilon$ and the material is defined *optically isotropic.* Finally, when two axes are equal and one is unequal, Equation B.5 becomes a spheroid and the material is such to have only one optical axis (*uniaxial*).

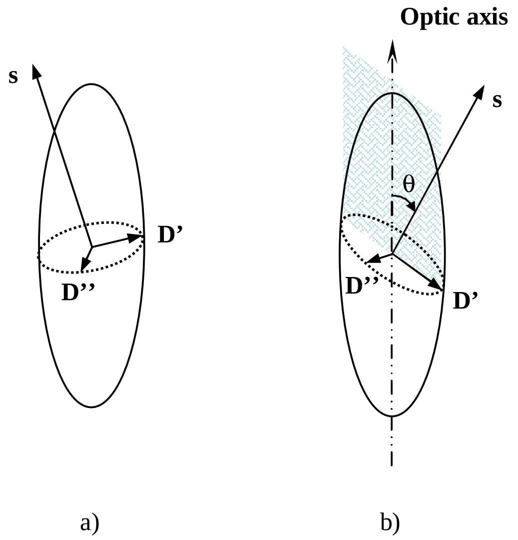

FIGURE B.1: (a) The ellipsoid of the wave normals. Construction of directions of **D** for a propagation direction $\hat{\mathbf{s}}$. (b) The directions of **D** in a uniaxial crystal.

B.2 Light propagating in a uniaxial material

Let us consider a uniaxial material with optic axis x, then $v_y = v_z = v_o$ and $v_x = v_e$. Equation B.3 reduces to

$$(v_p^2 - v_o^2)[(s_y^2 + s_z^2)(v_p^2 - v_e^2) + s_x^2(v_p^2 - v_o^2)] = 0. \tag{B.6}$$

Let θ be the angle that $\hat{\mathbf{s}}$ makes with the x axis; then

$$s_x^2 = \cos^2\theta \tag{B.7a}$$

$$s_y^2 + s_z^2 = \sin^2\theta. \tag{B.7b}$$

The two roots of Equation B.6 are given by

$$v_p'^2 = v_o^2 \tag{B.8a}$$

$$v_p''^2 = v_o^2\cos^2\theta + v_e^2\sin^2\theta. \tag{B.8b}$$

Equations B.8 show that one of the two waves that corresponds to any particular propagation direction is an *ordinary wave*, with a velocity independent of the direction of propagation, while the other, an *extraordinary wave*, has a velocity depending on the angle between the direction of the wave normal and the optic axis. The two velocities are only equal when $\theta = 0$, i.e. when the wave is propagating in the direction of the optical axis. When $v_o > v_e$ ($v_e > v_o$), the ordinary (extraordinary) wave travels faster than the extraordinary (ordinary) wave (except for $\theta = 0$ when they are equal), and the material is defined *positive* (*negative*).

The directions of **D** may be conveniently found with the help of the ellipsoid of wave normals, which has now two of its axes equal (Fig. B.1 (b)). The plane containing $\hat{\mathbf{s}}$ and the optic axis z is called the principal plane. The elliptical section through the origin by the plane perpendicular to $\hat{\mathbf{s}}$ has its semi-axes parallel and perpendicular to the principal plane. In particular the semi-axis perpendicular to the principal plane is equal to the radius of the equatorial circle of the spheroid and therefore it is proportional to n_o. In conclusion, the vector $\mathbf{D}$ of the ordinary wave vibrates in the direction perpendicular to the principal plane, while the vector of the extraordinary wave is in this plane.

B.2.1 The polarization state of light after travelling through a birefringent plate

We are now interested in detailing an expression which describes the polarization state of a monochromatic wave propagating through an isotropic material, after having traversed a birefringent plate of thickness t_p. We choose the z-axis as propagation direction, x and as the optical axis of the birefringent material. Consequently $\theta = 90°$ in Figure B.1 (b), and the directions of the vector $\mathbf{D}$ inside the birefringent material will be along the principal dielectric axes x and y ($n_x = n_e$, $n_y = n_o$).

Consider now the nature of the curve that the end of the electric vector describes at a typical point in space; this curve is the locus of points whose coordinates are (E_x, E_y);

$$E_x = a_x \cos(kz - \omega t + \phi_e), \tag{B.9a}$$

$$E_y = a_y \cos(kz - \omega t + \phi_o), \tag{B.9b}$$

with a phase delay corresponding to each of the vibration directions

$$\phi_e = \frac{2\pi}{\lambda} t_p n_e, \tag{B.10a}$$

$$\phi_o = \frac{2\pi}{\lambda} t_p n_o, \tag{B.10b}$$

and where $k = 2\pi/\lambda$ is the wavenumber, with λ the wavelength of the propagating field, and t is the time coordinate. Combining Equations B.9

$$\frac{E_x}{a_x} \sin\phi_o - \frac{E_y}{a_y} \sin\phi_e = \cos t' \sin(\phi_e - \phi_o), \tag{B.11a}$$

$$\frac{E_x}{a_x} \cos\phi_o - \frac{E_x}{a_y} \cos\phi_e = \sin t' \sin(\phi_e - \phi_o), \tag{B.11b}$$

Squaring and adding gives

$$\left(\frac{E_x}{a_x}\right)^2 + \left(\frac{E_y}{a_y}\right)^2 - 2\frac{E_x E_y}{a_x a_y} \cos(\phi_e - \phi_o) = \sin^2(\phi_e - \phi_o), \tag{B.12}$$

which is the equation of an ellipse.

This demonstrates that in general, the polarization of a monochromatic wave is elliptical after having travelled through a birefringent plate of thickness t_p. Nonetheless there are two cases in which the difference in phase shift

$$\phi_e - \phi_o = \frac{2\pi}{\lambda}(n_e - n_o)t_p, \tag{B.13}$$

is such that the ellipse degenerates to a straight line, or into a circle. When

$$\phi_e - \phi_o = m\pi \qquad (m = 0, \pm1, \pm2\ldots), \tag{B.14}$$

then

$$\frac{E_y}{E_x} = (-1)^m \frac{a_y}{a_x}, \tag{B.15}$$

and we say that the field $\mathbf{E}$ is *linearly polarized.* It is interesting to note that $m = 0$ means either that the material is isotropic, or that the direction of propagation is parallel to the optical axis. When instead

$$a_x = a_y, \tag{B.16a}$$

$$\phi_e - \phi_o = m\frac{\pi}{2} \qquad (m = 0, \pm1, \pm2\ldots), \tag{B.16b}$$

then $\mathbf{E}$ is *circularly polarized.*

B.3 Form birefringence

The birefringent properties of materials are usually explained in terms of the anisotropic electrical properties of molecules of which they are composed. However, birefringence may arise from anisotropy on a scale much larger than molecular, namely when there is an arrangement of similar particles of optically isotropic material whose size is large compared with the dimensions of molecules, but small compared with the wavelength of light. In this case we then speak of *form birefringence* [93].

We shall explain the principle by considering the case of an array that has the form of thin parallel plates (Fig. B.2). Let t_1 be the thickness of each plate and t_2 their separation. Further, let ε_1 be the dielectric constant of each plate and ε_2 the dielectric constant of the medium in which they are immersed.

Consider a monochromatic wave incident on the assembly, whose propagation direction $\hat{\mathbf{s}}$ is parallel to the z-axis, and assume first that its electric vector is perpendicular to the plates (x). If the linear dimensions of the faces of the plates are assumed to be large but the thickness t_1 and t_2 is small compared to the wavelength, the field in the plates and in the spaces may be considered uniform. Furthermore, the normal component of the electric displacement must be continuous across the surface at which the property of the medium changes abruptly. Hence the electric displacement must have the same value $\mathbf{D}$

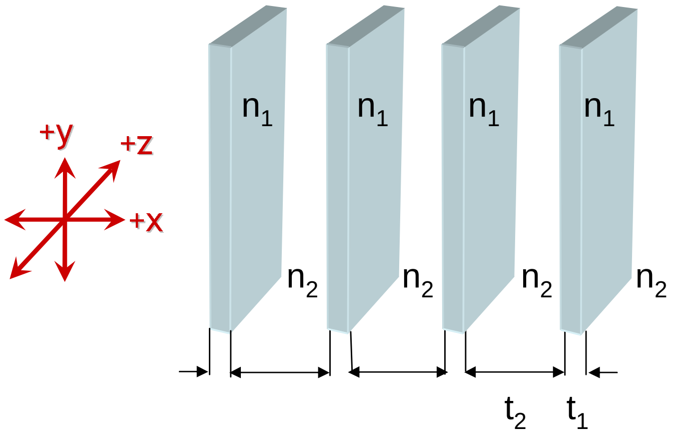

FIGURE B.2: A regular assembly of thin parallel plates.

inside the plates and in the spaces between them. If $\mathbf{E_1}$ and $\mathbf{E_2}$ are the corresponding electric fields, in the plates and in the surrounding medium,

$$\mathbf{E_1} = \frac{\mathbf{D}}{\varepsilon_1}, \quad \mathbf{E_2} = \frac{\mathbf{D}}{\varepsilon_2}, \tag{B.17}$$

thus, the mean field $\mathbf{E}$ averaged over the total volume is

$$\mathbf{E} = \frac{t_1\frac{\mathbf{D}}{\varepsilon_1} + t_2\frac{\mathbf{D}}{\varepsilon_2}}{t_1 + t_2}. \tag{B.18}$$

The effective dielectric constant ε_x is, therefore,

$$\varepsilon_x = \frac{\mathbf{D}}{\mathbf{E}} = \frac{\varepsilon_1\varepsilon_2}{f_f\varepsilon_2 + (1 - f_f)\varepsilon_1}, \tag{B.19}$$

where $f_f = t_1/(t_1 + t_2)$ is the fraction of the total volume occupied by the plates.

Suppose next that the incident field has its electric vector parallel to the plates (y). Since the tangential component of the electric field is continuous across a discontinuity surface, in this case the electric field will have the same value $\mathbf{E}$ inside the plates and in the space between. The electric displacements in two regions are then

$$\mathbf{D_1} = \varepsilon_1\mathbf{E}, \quad \mathbf{D_2} = \varepsilon_2\mathbf{E}, \tag{B.20}$$

so that the mean displacement $\mathbf{D}$ averaged over the total volume is

$$\mathbf{D} = \frac{t_1\varepsilon_1\mathbf{E} + t_2\varepsilon_2\mathbf{E}}{t_1 + t_2}. \tag{B.21}$$

Hence the effective dielectric constant is now given by

$$\varepsilon_y = \frac{\mathbf{D}}{\mathbf{E}} = f_f\varepsilon_1 + (1 - f_f)\varepsilon_2. \tag{B.22}$$

Since the effective dielectric constant is the same for all directions parallel to the plates, the assembly behaves as a uniaxial material with its optic axis perpendicular to the plane of the plates. Recalling that the extraordinary wave has its electric field in the principal plane defined by the propagation direction and the optic axis, the refractive indices may be expressed as

$$n_e^2 = \frac{n_1^2 n_2^2}{f_f n_2^2 + (1-f_f)n_1^2}, \tag{B.23a}$$

$$n_o^2 = f_f n_1^2 + (1-f_f)n_2^2. \tag{B.23b}$$

Finally, subtracting (B.23a) to (B.23b)

$$n_e^2 - n_o^2 = -\frac{f_f(1-f_f)(n_1^2-n_2^2)^2}{f_f n_2^2 + (1-f_f)n_1^2} \leqslant 0, \tag{B.24}$$

it is possible to conclude that the assembly of rectangular plates always behaves like a *negative* uniaxial material (Sec. B.1). For assemblies of particles of different forms Equation B.24 may have another expression; for instance in the case of an assembly of parallel and similar thin cylindric rods, if the rods occupy a small fraction of the total volume ($f_f \ll 1$) one has, in place of (B.24) [93],

$$n_e^2 - n_o^2 = \frac{f_f(1-f_f)(n_1^2-n_2^2)^2}{(1+f_f)n_2^2 + (1-f_f)n_1^2} \geqslant 0. \tag{B.25}$$

The sign of the measured difference between ordinary and extraordinary index indicates whether the shape of the particles is nearer to a rod or a plate, and if the fraction of volume occupied by the particles is known, it may be possible to estimate n_1 and n_2.

List of pulications

Journal papers

J. D. Mills, P. G. Kazansky, E. Bricchi, and J. J. Baumberg. Embedded anisotropic microreflectors by femtosecond-laser nanomachining. *Appl. Phys. Lett.*, 81(2):196–198, 2002.

E. Bricchi, J. D. Mills, P. G. Kazansky, B. G. Klappauf, and J. J. Baumberg. Birefringent Fresnel zone plates in silica by femtosecond laser machining. *Opt. Lett.*, 27(24):2200–2202, 2002.

E. Bricchi, B. G. Klappauf, and P. G. Kazansky. Form birefringence and negative index change created by femtosecond direct writing in transparent materials. *Opt. Lett.*, 29 (1):119–121, 2004.

A. Paleari, E. Franchina, E. Bricchi, N. Chiodini, A. Lauria, and P. G. Kazansky. SnO_2 nanocrystals in silica as nanosized tools for writing refractive index patterns through femtosecond-laser machining. Submitted to *Appl. Phys. Lett.*, 2005.

E. Bricchi and P. G. Kazansky. Extraordinary stability of direct written structures in silica glass. To be submitted to *Appl. Phys. Lett.*, 2005.

Conference papers

J. D. Mills, P. G. Kazansky, E. Bricchi, C. W. J. Hillman, and J. J. Baumberg. Direct microstructuring of fiber cores with femtosecond laser pulses. CLEO CMJ4, 2002.

J. D. Mills, P. G. Kazansky, E. Bricchi, and J. J. Baumberg. Anisotropic reflection from femtosecond laser directly-written structures. CLEO CMZ3, 2002.

E. Bricchi, J. D. Mills, P. G. Kazansky, and J. J. Baumberg. Maskless fresnel zone plates for dense embedded optical components. CLEO CMP7, 2002.

J. D. Mills, P. G. Kazansky, E. Bricchi, and J. J. Baumberg. Anisotropic micro-reflectors in glass by femtosecond laser machining. IQEC QW14, 2002.

P. G. Kazansky nad J. D. Mills, E. Bricchi, H. Inouye, J. Qiu, and K. Hirao. Photoinduced anisotropy and related phenomena in glass irradiated with ultrashort pulses. **(Invited)** International Symposium on Photonic Glasses, 2002.

J. J. Baumberg, J. D. Mills, P. G. Kazansky, and E. Bricchi. Anisotropic nanostructures directly written by fs pulses in wide-bandgap materials. NOEKS, 2003.

P. G. Kazansky, J. Mills, E. Bricchi, J. J. Baumberg, J. Qui, and K. Hirao. Self-organized form birefringence in glass irradiated by intense ultrashort light pulse. CLEO, 2003.

E. Bricchi, J. D. Mills, B. G. Klappauf, P. G. Kazansky, and J. J. Baumberg. Femtosecond direct writing of embedded photonic structures. **(Invited)** International Workshop on Recent Trends in Nonlinear Optics and Ultra-short Pulse Generation, 2003.

E. Bricchi, B. G. Klappauf, and P. G. Kazansky. Form birefringence anisotropic reflection and negative index change created by fs laser pulses in transparent materials. ICALEO M101, 2003.

P. G. Kazansky, Y. Shimotsuma, J. Qiu, E. Bricchi, and K. Hirao. Nanostructuring of transparent materials by light. BGPP WA5, 2003.

P. G. Kazansky, E. Bricchi, C. Corbari B. G. Klappauf, O. Deparis, J. Qiu, Y. Shimotsuma, and K. Hirao. Femtosecond laser nano-structuring of transparent materials. **(Invited)** ILATA-III and LAM-X, 2003.

E. Bricchi and P. G. Kazansky. Extraordinary stability of femtosecond direct written structures. POWAG, 2004.

P. G. Kazansky, E. Bricchi, Y. Shimotsuma, J. Qiu, and K. Hirao. Nanostructuring of transparent materials by ultrashort light pulses. TICON, 2004.

W. Yang, E. Bricchi, and P. G. Kazansky. Waveguide fabrication in bismuthate glasses using femtosecond laser pulses. POWAG, 2004.

P. G. Kazansky, E. Bricchi, Y. Shimotsuma J. Qiu and K. Hirao. Self-organized nanostructures in glass irradiated by femtosecond light pulses. **(Invited)** XX International Congress on Glass (ICG), 2004.

P. G. Kazansky, E. Bricchi, Y. Shimotsuma, J. Qui, and K. Hirao. 3D self-organized periodic nano-structures in glass irradiated by ultrashort light pulses. CLEO CFG5, 2005.

E. Bricchi, W. Yang, and P. G. Kazansky. Robustness of femtosecond direct written structures in silica glass. CLEO CThV4, 2005.

W. Yang, E. Bricchi, and P. G. Kazansky. Symmetric waveguides written in Er^{3+}-doped Bi_2O_3-based glass using femtosecond laser pulses. CLEO CThV6, 2005.

Bibliography

[1] B. C. Stuart, M. D. Feit, A. M. Rubenichik, B. W. Shore, and M. P. Perry. Laser-induced damage in dielectrics with nanosecond to subpicosecond pulses. *Phys. Rev. Lett.*, 74(12):2248–2251, 1995.

[2] L. Frey, J. M. Jonathan, A. Villing, and G. Roosen. Kinetics of photoinduced gratings by a moving grating technique. *Opt. Commun.*, 165:153–161, 1999.

[3] G. Zhang, Y. Tomita, X. Zhang, and J. Xu. Near-infrared holographic recording with quasi-nonvolatile readout in $LiNbO_3$:In, Fe. *Appl. Phys. Lett.*, 81(8):1393–1395, 2002.

[4] H. Hosono, Y. Abe, D. L. Kinser, R. A. Weeks, K. Muta, and H. Kawazoe. Nature and origin of the 5eV band in SiO_2:GeO_2 glasses. *Phys. Rev. Lett. B*, 46(18): 11445–11451, 1992.

[5] D. L. Williams, S. T. Davey, R. Kashyap, J. R. Armitage, and B. J. Ainslie. Ultraviolet absorption studies on photosensitive germanosilicate preforms and fibers. *Appl. Phys. Lett.*, 59:762–764, 1991.

[6] K. O. Hill, Y. Fuji, D. C. Johnson, and B. S. Kawasaki. Photosensitivity in optical fiber waveguides: Application to reflection filter fabrication. *Appl. Phys. Lett.*, 32: 647–649, 1978.

[7] M. Durkin, M. Ibsen, M. J. Cole, and R. I. Laming. 1m long continuously-written fibre Bragg gratings for combined second- and third-order dispersion compensation. *Electron. Lett.*, 33(22):1891–1893, 1997.

[8] I. J. G. Sparrow, G. D. Emmerson, C. B. E. Gawith, S. P. Watts, R. B. Williams, and P. G. R. Smith. Assessment of waveguide thermal response by interrogation of UV written planar gratings. *IEEE Photonic. Tech. L.*, 17(2):438–440, 2005.

[9] M. Ibsen, M. K. Durkin, M. N. Zervas, A. B. Grudinin, and R. I. Laming. Custom design of long chirped Bragg gratings: Application to gain-flattening filter with incorporated dispersion compensation. *IEEE Photonic. Tech. L.*, 12(5):498–500, 2000.

[10] G. Brambilla and H. Rutt. Fiber Bragg gratings with enhanced thermal stability. *Appl. Phys. Lett.*, 80(18):3259–3261, 2002.

[11] A. K. Mairaj, A. M. Chardon, D. P. Shepherd, and D. W. Hewak. Laser performance and spectroscopic analysis of optically written channel waveguides in neodymium-doped gallium lanthanum sulphide glass. *IEEE J. Sel. Top. Quant.*, 8:1381–1388, 2002.

[12] A. Favre, E. Lee, V. Apostolopoulos, C. B. E. Gawith, C. Y. Tai, E. M. Taylor, Y. Kondon, and F. Koizumi. UV-written channel waveguides in Er^{3+}-doped Bi_2O_3-based glass. *Phys. Stat. Sol. (c)*, 1(2):295–298, 2004.

[13] D. Du, X. Liu, G. Korn, J. Squier, and G. Mourou. Laser-induced breakdown by impact ionization in SiO_2 with pulse widths from 7 ns to 150 fs. *Appl. Phys. Lett.*, 64(23):3071–3073, 1994.

[14] D. Von der Linde and K. Sokolowski-Tinten. The physical mechanisms of short-pulse laser ablation. *Appl. Surf. Sci.*, 154-155:1–10, 2000.

[15] M. Lenzner, F. Krausz, J. Kruger, and W. Kautek. Photoablation with sub-10 fs laser pulses. *Appl. Surf. Sci.*, 154-155:11–16, 2000.

[16] H. Varel, M. Wahmer, A. Rosenfeld, D. Ashkenasi, and E. E. B. Campbell. Femtosecond laser ablation of sapphire: time-of-flight analysis of ablation plume. *Appl. Surf. Sci.*, 127-129:128–133, 1998.

[17] X. Li, T. Jia, D. Feng, and Z. Xu. Ablation induced by femtosecond laser in sapphire. *Appl. Surf. Sci.*, 225:339–346, 2004.

[18] W. G. Roeterdink, L. B. F. Juurlink, O. P. H. Vaughan, J. D. Diez, and M. Bonn nand A. W. Kleyna. Coulomb explosion in femtosecond laser ablation of Si(111). *Appl. Phys. Lett.*, 82(23):4190–4192, 2003.

[19] E. Glezer, M. Milosavljevic, L. Huang, R. J. Finlay, T. H. Her, J. P. Callan, and E. Mazur. Three-dimensional optical storage inside transparent materials. *Opt. Lett.*, 21(24):2023–2025, 1996.

[20] C. B. Schaffer, A. O. Jamison, and E. Mazur. Morphology of femtosecond laser-induced structural changes in bulk transparent materials. *Appl. Phys. Lett.*, 84 (2):1441–1443, 2004.

[21] H. Sun, Y. Xu, S. Juodkazis, K. Sun, M. Watanabe, S. Matsuo, H. Misawa, and J. Nishii. Arbitrary-lattice photonic crystals created by multiphoton microfabrication. *Opt. Lett.*, 26(6):325–327, 2001.

[22] K. M. Davis, K. Miura, N. Sugimoto, and K. Hirao. Writing waveguides in glass with a femtosecond laser. *Opt. Lett.*, 21(21):1729–1731, 1996.

[23] K. Miura, J. Qiu, H. Inouye, T. Mitsuyu, and K. Hirao. Photowritten optical waveguides in various glasses with ultrashort pulse laser. *Appl. Phys. Lett.*, 71 (23):3329–3331, 1997.

[24] D. Homoelle, S. Wielandy, A. L. Gaeta, N. F. Borrelli, and C. Smith. Infrared photosensitivity in silica glasses exposed to femtosecond laser pulses. *Opt. Lett.*, 24(18):1311–1313, 1999.

[25] Y. Sikorski, A. A. Said, P. Bado, R. Maynard, C. Florea, and K. A. Winick. Optical waveguide amplifier in Nd-doped glass written with near-IR femtosecond laser pulses. *Electron. Lett.*, 36(3):226–227, 2000.

[26] A. M. Streltsov and N. F. Borrelli. Fabrication and analysis of a directional coupler written in glass by nanojoule femtosecond laser pulses. *Opt. Lett.*, 26(1):42–43, 2001.

[27] G. Cerullo, R. Osellame, S. Taccheo, M. Marangoni, D. Polli, R. Ramponi, P. Laporta, and S. De Silvestri. Femtosecond micromachining of symmetric waveguides at 1.5μm by astigmatic beam focusing. *Opt. Lett.*, 27(21):1938–1940, 2002.

[28] S. J. Mihailov, C. W. Smelser, P. Lu, R. B. Walker, D. Grobnic, H. Ding, G. Henderson, and J. Unruh. Fiber Bragg gratings made with a phase mask and 800-nm femtosecond radiation. *Opt. Lett.*, 28(1):55–57, 2003.

[29] C. B. Schaffer, A. Brodeur, J. F. Garcia, and E. Mazur. Micromachining bulk glass by use of femtosecond laser pulses with nanojoule energy. *Opt. Lett.*, 26(2): 93–95, 2001.

[30] O. M. Efimov, L. B. Glebov, K. A. Richardson, E. Van Stryland, T. Cardinal, S. H. Park, M. Couzi, and J. L. Brunéel. Waveguide writing in chalcogenide glasses by a train of femtosecond laser pulses. *Opt. Mater.*, 17:379–386, 2001.

[31] J. B. Ashcom. *The role of focusing in the interaction of femtosecond laser pulses with transparent materials.* PhD thesis, The Department of Physics, Harvard University, Cambridge, Massachusetts, January 2003.

[32] M. M. Streltsov and N. F. Borrelli. Study of femtosecond-laser-written waveguides in glasses. *J. Opt. Soc. Am. B*, 19(10):2496–2504, 2002.

[33] K. Minoshima, A. M. Kowalevicz, I. Hartl, E. P. Ippen, and J. G. Fujimoto. Photonic device fabrication in glass by use of nonlinear materials processing with a femtosecond laser oscillator. *Opt. Lett.*, 26(19):1516–1518, 2001.

[34] S. M. Eaton, H. Zhang, P. R. Herman, F. Yoshino, L. Shah, J. Bovatsek, and A. Y. Arai. Heat accumulation effects in femtosecond laserwritten waveguides with variable repetition rate. *Opt. Express*, 13(12):4708–4716, 2005.

[35] Y. Kondo, K. Nouchi, T. Mitsuyu, M. Watanabe, P. G. Kazansky, and K. Hirao. Fabrication of long-period gratings by focused irradiation of infrared femtosecond laser pulses. *Opt. Lett.*, 24(10):646–648, 1999.

[36] S. J. Mihailov, C. W. Smelser, D. Grobnic, R. B. Walker, P. Lu, H. Ding, and J. Unruh. Bragg gratings written in all-SiO_2 and Ge-doped core fibers with 800-nm femtosecond radiation and a phase mask. *J. Lightwave Tech.*, 22(1):94–100, 2004.

[37] A. Marcinkevičius, S. Juodkazis, M. Watanabe, M. Miwa, S. Matsuo, H. Misawa, and J. Nishii. Femtosecond laser-assisted three-dimensional microfabrication in silica. *Opt. Lett.*, 26(5):277–279, 2001.

[38] S. Juodkazis, K. Yamasaki, V. Mizeikis, S. Matsuo, and H. Misawa. Formation of embedded patterns in glasses using femtosecond irradiation. *Appl. Phys. A*, 79: 1549–1553, 2004.

[39] Y. Bellouard, A. Said, M. Dugan, and P. Bado. Fabrication of high-aspect ratio, micro-fluidic channels and tunnels using femtosecond laser pulses and chemical etching. *Opt. Express*, 12(10):2120–2129, 2004.

[40] Y. Li, K. Itoh, W. Watanabe, K. Yamada, D. Kuroda, J. Nishii, and Y. Jiang. Three-dimensional hole drilling of silica glass from the rear surface with femtosecond laser pulses. *Opt. Lett.*, 26(23):1912–1914, 2001.

[41] H. Sun, S. Juodkazis, M. Watanabe, S. Matsuo, H. Misawa, and J. Nishii. Generation and recombination of defects in vitreous silica induced by irradiation with a near-infrared femtosecond laser. *J. Phys. Chem. B*, 104:3450–3455, 2000.

[42] S. Joudkazis, M. Watanabe, H. B. Sun, S. Matsuo, J. Nishii, and H. Misawa. Optically induced defects in vitreous silica. *Appl. Surf. Sci.*, 154(155):696–700, 2000.

[43] J. W. Chan, T. Huser, S. Risbud, and D. M. Krol. Structural changes in fused silica after exposure to focused femtosecond laser pulses. *Opt. Lett.*, 26(21):1726–1728, 2001.

[44] P. G. Kazansky, H. Inouye, T. Mitsuyu, K. Miura, J. Qiu, K. Hirao, and F. Starrost. Anomalous anisotropic light scattering in Ge-doped silica glass. *Phys. Rev. Lett.*, 82:2199–2202, 1999.

[45] J. Qui, P. G. Kazansky, J. Si, K. Miura, K. Hirao, and A. L. Gaeta. Memorized polarization-dependent light scattering in rare-earth-doped glass. *Appl. Phys. Lett.*, 77(13):1940–1942, 2000.

[46] L. Sudrie, M. Franco, B. Prade, and A. Mysyrowicz. Writing of permanent birefringent microlayers in bulk fused silica with femtosecond laser pulses. *Opt. Commun.*, 171:279–284, 1999.

[47] H. Guillet de Chatellus and E. Freysz. Characterization and dynamics of gratings induced in glasses by femtosecond pulses. *Opt. Lett.*, 27(13):1165–1176, 2002.

[48] J. D. Mills, P. G. Kazansky, E. Bricchi, C. W. J. Hillman, and J. J. Baumberg. Direct microstructuring of fiber cores with femtosecond laser pulses. CLEO CMJ4, 2002.

[49] X. Wang, H. Guo, H. Yang, H. Jiang, and Q. Gong. Characterization and dynamics of gratings induced in glasses by femtosecond pulses. *Appl. Opt.*, 43(23):4571–4574, 2004.

[50] P. Oberson, B. Gisin, B. Huttner, and N. Gisin. Refracted near-field measurements of refractive index and geometry of silica-on-silicon integrated optical waveguides. *Appl. Opt.*, 37(31):7268–7272, 1998.

[51] J. W. Chan, T. R. Huser, S. H. Risbud, and J. S. Hayden D. M. Krol. Waveguide fabrication in phosphate glasses using femtosecond laser pulses. *Appl. Phys. Lett.*, 82(15):2371–2373, 2003.

[52] V. Apostolopoulos, L. Laversenne, T. Colomb, C. Depeursinge, R. P. Salathé, M. Pollnau, R. Osellame, G. Cerullo, and P. Laporta. Femtosecond-irradiation-induced refractive-index changes and channel waveguiding in bulk Ti^{3+} :Sapphire. *Appl. Phys. Lett.*, 85(7):1122–1124, 2004.

[53] G. P. Agrawal. *Nonlinear fiber optics.* Academic Press, 1995.

[54] R. Boyd. *Nonlinear optics.* Academic Press, second edition, 2003.

[55] A. L. Gaeta. Catastrophic collapse of ultrashort pulses. *Phys. Rev. Lett.*, 84(16): 3582–3585, 2000.

[56] S. H Cho, H. Kumagai, K. Midorikawa, and M. Obara. Fabrication of double cladding structure in optical multimode fibers using plasma channeling excited by a high-intensity femtosecond laser. *Opt. Commun.*, 168:287–295, 1999.

[57] C. B. Schaffer, A. Brodeur, and E. Mazur. Laser-induced breakdown and damage in bulk transparent materials induced by tightly focused femtosecond laser pulses. *Mater. Sci. Tech.*, 12:1784–1794, 2001.

[58] S. C. Jones, P. Braunlich, R. T. Casper, X. A. Shen, and P. Kelley. Recent progress on laser-induced modifications and intrinsic bulk damage of wide-gap optical-materials. *Opt. Eng.*, 28(10):1039–1068, 1989.

[59] L. V. Keldysh. Ionization in the field of a strong electromagnetic wave. *Sov. Phys. JETP*, 20(5):1307– 1314, 1965.

[60] A. Kaiser, B. Rethfeld, M. Vicanek, and G. Simon. Microscopic processes in dielectrics under irradiation by subpicosecond laser pulses. *Phys. Rev. B*, 61(17): 11437–11450, 2000.

[61] J. I. Pankove. *Optical processes in semiconductors.* Englewood Cliffs: Prentice-Hall, 1971.

[62] H. B. Sun, Y. Xu, S. Juodkazis, K. Sun, J. Nishii, Y. Suzuki, S. Matsuo, and H. Misawa. Photonic lattices achieved with high-power femtosecond laser microexplosion in transparent solid materials. volume 388, pages 131–142. SPIE, 2000.

[63] S. H Cho, H. Kumagai, and K. Midorikawa. In situ observation of dynamics of plasma formation and refractive index modification in silica glasses excited by a femtosecond laser. *Opt. Commun.*, 207:243–253, 2002.

[64] E. N. Glezer, Y. Huang, and E. Mazur. The behavior of $\chi^{(2)}$ during laser-induced phase transition in GaAs. *Phys. Rev. Lett. B*, 51(15):9589–9596, 1995.

[65] D. Von der Linde and H. Schuler. Breakdown threshold and plasma formation in femtosecond laser solid interaction. *J. Opt. Soc. Am. B*, 13(1):216–222, 1996.

[66] B. C. Stuart, M. D. Feit, S. Herman, A. M. Rubenchik, B. W. Shore, and M. D. Perry. Nanosecond-to-femtosecond laser-induced breakdown in dielectrics. *Phys. Rev. B*, 53(4):1749–1761, 1996.

[67] A. C. Tien, S. Backus, H. Kapteyn, M. Murnane, and G. Mourou. Short-pulse laser damage in transparent materials as a function of pulse duration. *Phys. Rev. Lett.*, 82(19):3883–3886, 1999.

[68] M. Lenzner, J. Kruger, S. Sartania, Z. Cheng, Ch. Spielmann, G. Mourou, W. Kautek, and F. Krausz. Femtosecond optical breakdown in dielectrics. *Phys. Rev. Lett.*, 80(18):4076–4079, 1998.

[69] M. D. Berry, B. C. Stuart, P. S. Banks, M. D. Feit, V. Yanovsky, and A. M. Rubenchik. Ultrashort-pulse laser machining of dielectric materials. *J. Appl. Phys.*, 85(9):6803–6805, 1999.

[70] J. Jasapara, A. V. V. Nampoothiri, W. Rudolph, D. Ristau, and K. Starke. Femtosecond laser pulse induced breakdown in dielectric thin films. *Phys. Rev. B*, 63: 0451171–0451175, 2001.

[71] Z. Wu, H. Jiang, L. Luo, H. Guo, H. Yang, and Q. Gong. Multiple foci and long filament observed with focused femtosecond pulse propagation in fused silica. *Opt. Lett.*, 27(6):448–450, 2002.

[72] Z. Wu, H. Jiang, H. Yang, and Q. Gong. The refocusing behaviour of a focused femtosecond laser pulse in fused silica. *J. Opt. A: Pure Appl. Opt.*, 5:102–107, 2003.

[73] L. Sudrie, A. Couairon, M. Franco B. Lamouroux, B. Prade, S. Tzortzakis, and A. Mysyrowicz. Femtosecond laser-induced damage and filamentary propagation in fused silica. *Phys. Rev. Lett.*, 89(18):1866011–1866014, 2002.

[74] K. Yamada, W. Watanabe, T. Toma, K. Itoh, and J. Nishii. In *situ* observation of photoinduced refractive-index changes in filaments formed in glasses by femtosecond laser pulses. *Opt. Lett.*, 26(1):19–21, 2001.

[75] L. Luo, D. Wang, C. Li, H. Jiang, H. Yang, and Q. Gong. Formation of diversiform microstructures in wide-bandgap materilas by tight-focusing femtosecond laser pulses. *J. Opt. A: Pure Appl. Opt.*, 4:105–110, 2002.

[76] S. Tzortzakis, L. Sudrie, M. Franco, B. Prade, A. Mysyrowicz, A. Couairon, and L. Bergé. Self-guided propagation of ultrashort IR laser pulses in fused silica. *Phys. Rev. Lett.*, 87(19):2139021–2139024, 2001.

[77] C. Joenathan. Phase-measuring interferometry: new methods and error analysis. *Appl. Opt.*, 33(19):4147–4155, 1994.

[78] N. Kitaura, S. Ogata, and Y. Mori. Spectrometer employing a micro-Fresnel lens. *Opt. Eng.*, 34(2):584–588, 1995.

[79] M. Haruna, M. Takahashi, K. Wakahayashi, and H. Nishihara. Laser beam lithographed micro-Fresnel lenses. *Appl. Opt.*, 29(34):5120–5126, 1990.

[80] J. Canning, K. Sommer, S. Huntington, and A. Carter. Silica-based fibre Fresnel lens. *Opt. Commun.*, 199(5):375–381, 2001.

[81] D. A. Buralli, G. M. Morris, and J. R. Rogers. Optical performance of holographic kinoforms. *Appl. Opt.*, 28(5):975–983, 1989.

[82] H. Dammann. Blazed syntetic phase-only holograms. *Optik*, 31(1):95–98, 1970.

[83] R. W. Wood. Phase reversal zone-plates and diffraction-telescopes. *Phil. Mag.*, 45 (277):511–523, 1898.

[84] E. Hecht. *Optics*. Addison-Welsey, third edition, 1998.

[85] J. Kirz. Phase zone plates for X rays and extreme UV. *J. Opt. Soc. Am.*, 64(3): 301–309, 1974.

[86] H. Nishihara and T. Suhara. *Progress in Optics*, volume XXIV, pages 5–11. Elsevier Science Publishers B. V. Amsterdam, 1987.

[87] J. Higbie. Fresnel zone plate: Anomalous foci. *Am. J. Phys.*, 44(10):929–930, 1976.

[88] O. Svelto. *Principles of lasers*. Plenum Press, fourth edition, 1998.

[89] G. P. Agrawal. *Applications of nonlinear fiber optics.* Academic Press, 2001.

[90] S. R. Brueck and D. J. Ehrlich. Stimulated surface-plasma-wave scattering and growth a periodic structure in laser-photodeposited metal films. *Phys. Rev. Lett.*, 48(24):1678–1681, 1982.

[91] Y. Shimotsuma, P. G. Kazansky, J. Qiu, and K. Hirao. Self-organized nanogratings in glass irradiated by ultrashort light pulses. *Phys. Rev. Lett.*, 91(24):2474051–2474054, 2003.

[92] L. Sudrie, M. Franco, B. Prade, and A. Mysyrowicz. Study of damage in fused silica induced by ultra-short IR laser pulses. *Opt. Commun.*, 191:333–339, 2001.

[93] M. Born and E. Wolf. *Principles of optics.* Cambridge University Press, Cambridge, 1999.

[94] P. G. Kryukov, Yu. V. Larionov, A. A. Rybaltovskii, K. A. Zagorulko, A. Dragomir, D. N. Nikogosyan, and A. A. Ruth. Long-period fibre grating fabrication with femtosecond pulse radiation at different wavelengths. *Microelec. Eng.*, 69:248–255, 2003.

[95] D. Ashkenasi, H. Varel, A. Rosenfeld, S. Henz, J. Herrmann, and E. E. B. Cambell. Application of self-focusing of ps laser pulses for three-dimensional microstructuring of transparent materials. *Appl. Phys. Lett.*, 72(12):1442–1444, 1998.

[96] A. G. Sitenko. *Electromagnetic Fluctuations in Plasma.* Academic Press, 1967.

[97] Q. Zhong and D. Inniss. Characterization of the lightguiding structure of optical fibers by Atomic Force Microscopy. *J. Lightwave Tech.*, 12(9):1517–1523, 1994.

[98] C. Hnatovsky, R. S. Taylor, R. Bhardwaj, E. Simova, D. M. Rayner, and P. B. Corkum. Long-range periodic planar nanostructures produced in glass by femtosecond laser dielectric modification. CLEO CThV1, 2005.

[99] N. Chiodini, A. Paleari, D. DiMartino, and G. Spinolo. SnO_2 nanocrystals in SiO_2: A wide-band-gap quantum-dot system. *Appl. Phys. Lett.*, 81(9):1702–1704, 2002.

[100] N. Chiodini, F. Meinardi, F. Morazzoni, J. Padovani, A. Paleari, R. Scotti, and G. Spinolo. Thermally induced segregation of SnO_2 nanoclusters in Sn-doped silica glasses from oversaturated Sn-doped silica xerogels. *J. Mater. Chem.*, 11:926–929, 2001.

[101] N. Chiodini, A. Paleari, and G. Spinolo. Photorefractivity in nanostructured Tin-Silicate glass ceramics: A radiation-induced nanocluster size effect. *Phys. Rev. Lett.*, 90(5):0555071–0555074, 2003.

[102] N. Chiodini, A. Paleari, G. Spinolo, and P. Crespi. Photorefractivity in SiO_2:SnO_2 glass-ceramics by visible light. *J. Non-Cryst. Solids*, 322:266–271, 2003.

[103] A. Paleari, E. Franchina, E. Bricchi, N. Chiodini, A. Lauria, and P. G. Kazansky. SnO_2 nanocrystals in silica as nanosized tools for writing refractive index patterns through femtosecond-laser machining. Submitted to Adv. Mat., 2005.

[104] A. Diéguez, A. Romano-Rodríguez, A. Vilà, and J. R. Morante. The complete Raman spectrum of nanometric SnO_2 particles. *J. Appl. Phys.*, 90(3):1550–1557, 2001.

[105] F. L. Galeener. Band limits and the vibrational spectra of tetrahedral glasses. *Phys. Rev. B*, 19(8):4292–4297, 1978.

[106] N. Sugimoto. Ultrafast optical switches and wavelength division multiplexing (WDM) amplifiers based on bismuth oxide glasses. *J. Am. Ceram. Soc.*, 85(5): 1083–1088, 2002.

[107] S. Tanabe, N. Sugimoto, S. Ito, and T. Hanada. Broad-band $1.5\,\mu m$ emission of Er^{3+} ions in bismuth-based oxide glasses for potential WDM amplifier. *J. Lumin.*, 87:670–672, 2000.

[108] W. Yang, E. Bricchi, and P. G. Kazansky. Symmetric waveguides written in Er^{3+}-doped Bi_2O_3-based glass using femtosecond laser pulses. CLEO CThV6, 2005.

[109] L. B. Shaw, B. Cole, P. A. Thielen, J. S. Sanghera, and I. D. Aggarwal. Mid-wave IR and long-wave IR laser potential of rare-earth doped chalcogenide glass fiber. *IEEE J. Quantum Elect.*, 37:1127–1137, 2001.

[110] A. K. Mairaj. *Optical waveguides and lasers in improved gallium lanthanum sulphide glass.* PhD thesis, Faculty of Engineering and Applied Science Optoelectronics Research Centre, 2003.

[111] A. K. Mairaj, P. Hua, H. N. Rutt, and D. W. Hewak. Fabrication and characterization of continuous wave direct UV ($\lambda = 244$ nm) written channel waveguides in chalcogenide (Ga:La:S) glass. *J. Lightwave Tech.*, 20(8):1578–1584, 2002.

[112] K. Yamada, W. Watanabe, Y. Li, K. Itoh, and J. Nishii. Multilevel phase-type diffractive lenses in silica glass induced by filamentation of femtosecond laser pulses. *Opt. Lett.*, 29(16):1846–1848, 2004.

[113] R. Grunwald, U. Griebner, F. Tschirschwitz, E. T. J. Nibbering, T. Elsaesser, V. Kebbel, H.-J. Hartmann, and W. Jptner. Generation of femtosecond Bessel beams with microaxicon arrays. *Opt. Lett.*, 25(13):981–983, 2000.

[114] C. Tamm and C. O. Weiss. Bistability and optical switching of spatial patterns in a laser. *J. Opt. Soc. Am. B*, 7(6):1034–1038, 1990.

[115] M. Padgett, J. Arlt, N. Simpson, and L. Allen. An experiment to observe the intensity and phase structure of Laguerre-Gaussian laser modes. *Am. J. Phys.*, 64 (1):77–82, 1996.

[116] Y. Shimotsuma, K. Hirao, j. Qiu, and P. G. Kazansky. Nano-modification inside transparent materials by femtosecond laser single beam. *Mod. Phys. Lett. B*, 19 (5):225–238, 2005.

[117] F. F. Chen. *Introduction to plasma physics*. Plenum Press, 1974.

[118] A. G. Michette and C. J. Buckley. *X-Ray Science and Technology*. IOP Publishing Ltd., 1993.

[119] D. Attwood. *Soft X-Rays and extreme ultraviolet radiation*. Univ. Press, 1999.